An Implementation of Smoothed Particle Hydrodynamics For Large Deformation, History Dependent Geomaterials With Applications to Tectonic Deformation

Hans Frederick Schwaiger

A dissertation submitted in partial fulfillment
of the requirements for the degree of

Doctor of Philosophy

University of Washington

2007

Program Authorized to Offer Degree: Earth and Space Sciences

University of Washington
Graduate School

This is to certify that I have examined this copy of a doctoral dissertation by

Hans Frederick Schwaiger

and have found that it is complete and satisfactory in all respects,
and that any and all revisions required by the final
examining committee have been made.

Chair of the Supervisory Committee:

_____

Sean D. Willett

Reading Committee:

_____

Sean D. Willett

_____

Gerard Roe

_____

John Booker

Date: _____

In presenting this dissertation in partial fulfillment of the requirements for the doctoral degree at the University of Washington, I agree that the Library shall make its copies freely available for inspection. I further agree that extensive copying of this dissertation is allowable only for scholarly purposes, consistent with "fair use" as prescribed in the U.S. Copyright Law. Requests for copying or reproduction of this dissertation may be referred to Proquest Information and Learning, 300 North Zeeb Road, Ann Arbor, MI 48106-1346, 1-800-521-0600, to whom the author has granted "the right to reproduce and sell (a) copies of the manuscript in microform and/or (b) printed copies of the manuscript made from microform."

Signature_____

Date_____

University of Washington

Abstract

An Implementation of Smoothed Particle Hydrodynamics For Large Deformation, History Dependent Geomaterials With Applications to Tectonic Deformation

Hans Frederick Schwaiger

Chair of the Supervisory Committee:
Professor Sean D. Willett
Department of Earth and Space Sciences

The deformation of a wide range of materials in geology can be described by fluid behavior, whether of mass wasting, cooling lava or crustal flows. These "geophysical flows" can be problematic to model numerically as they can involve the significant deformation of heterogeneous, history-dependent material. The large deformation can become increasingly troubling when it is highly localized in shear bands or on discrete failure plains such as with the brittle deformation along faults in the upper crust. Traditional, grid-based numerical schemes have difficulty capturing this faulting behavior. An alternative approach is to use a numerical scheme that does not rely on a grid. In this dissertation, a mesh-free formulation, based on the Smoothed Particle Hydrodynamics (SPH) method, is developed for the significant deformation of creeping, visco-plastic material as applied to the brittle failure of the continental crust in tectonic deformation.

To apply the SPH scheme to creeping, viscous flows, several modifications are needed. The first modification is an improved treatment of the Laplacian operator, particularly near the surface of the flow where the standard SPH discretization fails. Secondly, a means of enforcing the incompressibility constraint is developed. In the course of these efforts, an improved treatment of boundary conditions is implemented. Finally, to simulate the deformation of crustal material, a Mohr-Coulomb rheology is added along with modifications to improve the localization of strain. The numerical model is then applied to two tectonic environments: a doubly-vergent wedge and a symmetric rift.

The SPH model with these modifications performs well for creeping, viscous, incompressible flow and thermal diffusion. The Mohr-Coulomb implementation performs satisfactorily (convergence is slow), however, due to the width of the SPH discretization, the shear bands do not result in strain more localized than with grid-based methods. As such, the SPH method as presented is well suited for modeling coupled thermo-mechanical flows of history-dependent material, such as the rolling

advance of cooling lava. Brittle deformation can be approximated, however it is not clear that the influence of the width of the SPH discretization can be overcome efficiently, particularly in comparison with other mesh-free methods.

TABLE OF CONTENTS

LIST OF FIGURES

LIST OF TABLES

ACKNOWLEDGMENTS

This dissertations is the result of several years of what, at times, seemed to be a solitary effort. A little reflection, though, and there are many, many people to acknowledge and thank. First, of course, thanks go to my advisor, Sean Willett, who introduced me to particle methods and has provided much-needed encouragement and advice at key points in this PhD effort. George Bergantz also provided notable encouragement in the early years. I owe nearly the entire base of my knowledge of numerical methods to Randy LeVeque. His willingness to help me sort out my ideas was beyond expectation and will not be forgotten. Thanks also go to John Booker for teaching me fluid mechanics and a significant tip-of-the-hat to Gerard Roe for graciously and generously agreeing to be a last-minute addition to my reading committee. Altruism *par excellence*. Joe Monaghan provided crucial encouragement, guidance and support at a time when it was not at all clear that this project would come to fruition. His influence played a pivotal role in my completion of this work.

Then there are the grad students. Drew Stolar, Chris Fuller, Jane Lock, Heather Sherrington, Joe Dufek, Noah Finnegan, Alison Anders, Philipp Ruprecht and Hig were great sounding boards for vetting ideas or just learning about how things work.

This project could never have happened if it were not for someone at NSF who decided to collect scraps of funds from each of the programs for continental dynamics, geophysics and infrastructure in order to allow this project to proceed. To that anonymous and creative funder, "Thank you." I've been the fortunate beneficiary of many other anonymous donors, in particular those at the ARCS Foundation and those donating to the UW ESS department. It's humbling to think of all those people who wrote checks on my behalf. Thank you.

And finally, thanks to my family and friends for all the support over the years. Especially to all those kind people who helped facilitate my transient lifestyle: my sister Ursula for the storage and temporary shelter, Richard for the short-term housing, and Jen and her housemates for taking care of Lena in my months abroad. Most of all, thanks to Denise who put up with countless evenings of me going back to work and who never once pointed out how comical the contrast is between a bad day of work for me (couldn't track down the bug that caused my mountains to collapse) and a bad day for her (couldn't track down the bug that caused her patient's lives to collapse).

DEDICATION

To my grandfather, Frederick Roemer, who saw a budding scientist in me and cultivated the desire to learn.

Chapter 1

INTRODUCTION

'Geophysical flow' is a term broadly used for describing the deformation and flow of geomaterials in many natural environments. These range from the faster flows such as landslides or atmospheric flows to the creeping flows of lava and crustal material [54]. In each of these cases, the essential mechanics of the problem can be cast in terms of a viscous fluid described by the incompressible Navier-Stokes equations. Viscous stresses might be negligible, as in the case of atmospheric flows, or significant as with a landslide. In other cases, such as with creeping flow, the viscous stresses may be dominant. This viscous model for geophysical flows allows for including plastic behavior through a non-linear viscosity. This is a useful framework for addressing deformation of crustal material in which the primary mode of deformation changes from brittle at shallow depths, to ductile at greater depths. The brittle deformation can be modeled using a frictional plastic rheology through a non-linear, stress-dependent viscosity whereas the ductile deformation can be modeled with a viscosity linear in stress (although dependent on temperature).

In many of these examples, the flows can be quite complicated and involve heterogeneous materials such as multiple fluids interacting, or materials with some sort of dependence on the fluid's history. For example, this dependence could be a rheologic dependence of the integrated strain history with the material either weakening or strengthening with increasing deformation. Alternatively, the rheology of a material parcel could be dependent on the thermal history of that parcel, in which case an accurate estimate of the parcel's path through an evolving temperature field would be needed to calculate the evolution of the rheology.

The primary geophysical flow with which this thesis is concerned is the visco-plastic flow of crustal material. For this flow, the accumulated damage on a parcel of material plays a significant role in the localization of strain. This is important since the brittle deformation of crustal material which occurs on distinct faults, can be modeled as highly localized shear bands.

This class of flows in which the deformation is large, yet requires an accurate accounting of the material history, such as the accumulated damage, has provided additional hurdles for traditional numerical methods. By 'traditional', I refer to the many numerical methods that rely on a grid or

mesh (Finite Difference, Finite Volume, Finite Element) to efficiently convert the governing partial differential equations to algebraic equations. Generally, the frame of reference of a numerical method is chosen to be either fixed in space (Eulerian reference frame) or fixed to the material (Lagrangian reference frame). An advantage of the Eulerian frame is that since the grid remains fixed, arbitrarily large deformations can easily be accommodated, however the history of an individual material parcel is difficult to track. The Lagrangian frame, in contrast, inherently tracks material history since the grid follows the deformation, however the accuracy of the calculations is often dependent of the geometry of the grid. As this geometry become more distorted, the accuracy of the numerical solution suffers and can fail if steps are not taken to prevent the mesh from becoming entangled. As such, the Lagrangian methods generally are used for small deformations such as elastic behavior or the onset of plastic failure of elasto-plastic material. As opposed to the failure analysis problems of mechanical engineering, for geomaterials undergoing plastic failure, it is often the behavior post-yield that is of interest, leading to the same mesh-entanglement issues.

Grid-based numerical methods can be cast in either of these frames of reference for the simulation of large deformation flows with the understanding that there will be errors that arise either from the numerical diffusion of material properties in Eulerian schemes, or interpolation errors from regridding a severely deformed Lagrangian mesh. To mitigate this problem, an Eulerian mesh can be used with some mechanism of tracking particle paths and material history. These include the Arbitrary Lagrangian-Eulerian (ALE) [36] method which advects a Lagrangian grid based on Eulerian velocities, and the Particle-in-cell (PIC) method [88, 87] which tracks material properties and histories of particles that communicate their values to an Eulerian grid. Other similar methods include the Marker-and-cell (MAC) [48] and the Material Point Method (MPM) [129]. All of these methods rely on an underlying Eulerian grid for solving the continuum equations and to some extent are susceptible to the associated numerical diffusion.

The geophysical flow of visco-plastic deformation in the upper crust highlights many of these potential sources of errors when using grid-based methods. Deformation can be large and can involve inhomogeneous material. The material's rheology may be dependent on its history. Zones of highly localized shear deformation (faults) are the primary mode of deformation. Because of these various features of this class of flow and the difficulty of the grid-based methods in simultaneously addressing all of them, a method that does not need a grid is an attractive option.

1.1 Mesh-free numerical modeling

An alternative to grid-based numerical methods such as finite difference and finite element methods are the mesh-free (particle) methods. As the name suggests, the equations of motion are solved on a set of particles with no underlying mesh. The particles, essentially, correspond to fluid parcels. The primary advantage of this approach is that a Lagrangian frame can be chosen (which is advantageous for tracking history dependent material) without the problems of mesh entanglement, loss of accuracy due to highly deformed grids, or the computational expense and loss of accuracy due to frequent regridding.

Mesh-free methods have a long history in the fluid dynamics community starting with Smoothed Particle Hydrodynamics (SPH) [71, 38] in the mid-1970's which was developed for inviscid gas dynamics. The past ten years have seen a dramatic evolution of the SPH method with applications to free-surface, shallow-water flows [82], solid mechanics [40], impact problems [56], and fluid–solid interactions [93]. In order to extend the applicability of SPH to these problems, several improvements needed to be included. For example, in problems where the object has a stress-free surface (as opposed to problems of gas dynamics) the spatial discretization in the SPH method fails to accurately represent even constant functions in the vicinity of that surface. Various corrections for this lack of consistency of the method have been introduced often with a rechristening of the method. For example, the Reproducing Kernel Particle Method (RKPM) [69] uses correction functions that require that the discretization reproduce polynomials of a given order. The Corrected Smoothed Particle Hydrodynamics (CSPH) [5] also uses a correction function, but one derived from a Taylor series expansion. The Corrective Smoothed Particle Method (CSPM) [18] and the related Modified SPH (MSPH) method [147]) also use a Taylor series expansion, but include higher order terms and are applicable to discretization of the second derivative. The development of these techniques was crucial in addressing other required improvements to SPH such as the ability to properly enforce essential and natural boundary conditions. All these methods mentioned above are collocation methods, but mesh-free Galerkin methods have also been developed such as the Element Free Galerkin (EFG) [3] and Meshless Local-Petrov-Galerkin [65] methods.

More recently, these improved mesh-free methods have been applied to the problem of the localization of plastic failure. The RKPM was applied to strain localization by Li and Liu [62]. A variant of SPH (MSPH) was used in adiabatic shear bands by Batra and Zhang [1]. Rabczuk and Areias [108] employed the EFG method and Li et al. [64] used a mesh-free Galerkin method. In each of these studies, an elasto-viscoplastic rheology was used with an emphasis on dynamic problems. As such, explicit integration was used in each of these examples.

The work presented in this thesis is the extension of the SPH method to creeping, incompressible visco-plastic flow with an emphasis on the localization of shear-bands. In addressing this problem, several modifications to the classic SPH algorithm needed to be developed.

1.1.1 Classic SPH discretization

The classic SPH discretization starts with a function representation as follows.

$$f(x) = \int_\Omega f(x')\delta(x - x')\,\mathrm{d}x'$$

Ω is the domain and δ is the Dirac delta function.

The SPH spatial discretization involves a two-step approximation. First δ is approximated by a kernel (W) of finite width, h.

$$\begin{aligned} f(x) &= \int_\Omega f(x')\delta(x - x')\,\mathrm{d}x' && (1.1)\\ &\simeq \int_\Omega f(x')W(x - x', h)\,\mathrm{d}x' && (1.2)\end{aligned}$$

Next, the integral is approximated by a summation over discrete set of points.

$$\begin{aligned} f(x) &\simeq \int_\Omega f(x')W(x - x', h)\,\mathrm{d}x' && (1.3)\\ &\simeq \sum_j f(x_j)W(x - x_j, h)\varphi_j \end{aligned}$$

j are the particles in the support domain (within the region of influence of the kernel, W) and φ_j is the discrete volume element equal to the ratio of the particle's mass to its density (m_j/ρ_j).

Problems can arise in both steps of this approximation. If the point of interest is near a boundary, then the kernel might be truncated by the boundary. If measures are not taken into account for this insufficiency of the support domain, the first approximation will lead to increased errors. Secondly, if there is an insufficient number of particles in the support domain, then the second step of the approximation will flounder.

The SPH approximation of first derivative arises from applying an integration by parts to the integral approximation. Assuming that the kernel is identically zero beyond some fixed radius, the boundary term of the integration by parts can be neglected.

$$f(x)_{,\alpha} \simeq \int_\Omega f(x')W_{,\alpha}\,\mathrm{d}x' \qquad (1.4)$$

The Greek indices refer to coordinates and comma denotes partial differentiation. Second derivatives can be similarly approximated by applying a second integration by parts.

$$f(x)_{,\alpha\beta} \simeq \int_{\Omega} f(x')W_{,\alpha\beta}\,\mathrm{d}x' \tag{1.5}$$

Each of these integral approximations can then be approximated by a summation over a set of neighboring particles as before, but each of these approximations can suffer from the same boundary and kernel deficiency issues as do the function approximations. Most of the correction methods have been developed to improve function and gradient approximations. To calculate solutions for creeping flow, an accurate evaluation of the Laplacian is needed which currently requires expensive corrections.

Additionally, incompressibility is approximated in the classic SPH algorithm by allowing a slight compressibility through an equation of state with a high speed of sound, then explicitly integrating density via the continuity equation. For creeping flow problems, this approach is not practical since the high viscosity makes an explicit integration scheme very inefficient.

These problems must be addressed in order to apply SPH to creeping flow problems.

1.2 Outline of thesis

This thesis is organized as follows. In chapter 2, to highlight a class of geophysical flows ripe for a mesh-free solution, the classic SPH implementation of free-surface, viscous flow is applied to the high velocity impact of two fluids of differing density and viscosity. In this case, the viscous fluid is a landslide and the less viscous fluid is water. Calculations of the resulting wave height and run-up are constrained by laboratory data and published field observations.

Chapter 3 presents a formulation of SPH for diffusive initial, boundary value problems with free-surfaces. Issues that need to be addressed are:

- Implementing general linear boundary conditions (Dirichlet, Neumann, Mixed) at both walls and surfaces
- The deficiency of the Laplacian calculation near surface boundaries
- Casting the initial-boundary value problem implicitly and using iterative solvers

Chapter 4 presents a formulation of SPH to creeping, viscous, incompressible flows. This formulation relies heavily on the developments of chapter 3, but also focuses on efficient methods for imposing the incompressibility constraint.

Chapter 5 applies the developments of chapters 3 and 4 to two idealized tectonic settings: symmetric divergence (rift) and asymmetric convergence (doubly-vergent wedge). Linear viscous and visco-plastic cases are shown. The primary issues addressed in this chapter are:

- Implementing a Mohr-Coulomb rheology for creeping flow
- Development of shear-bands via strain softening
- Improving the localization of the shear-bands through modifying the kernel width and adaptively refining the particle distribution

Finally, some concluding remarks are given in chapter 6.

Chapter 2

APPLICATION OF SPH TO TSUNAMIGENIC LANDSLIDES

A version of this chapter entitled "Lagrangian hydrocode simulations of the 1958 Lituya Bay tsunamigenic rockslide" was submitted to *Geochemistry, Geophysics, Geosystems*. Bretwood Higman was the co-author.

The interaction of debris flows, whether subaqueous or subaerial, with bodies of water can produce tsunamis with a locally devastating impact. When debris flows begin above the water surface, the impact can produce a large air cavity, significantly increasing the effective volume of water displaced and complicating efforts to model the resulting tsunami. Because grid-based, Eulerian numerical methods have an inherent difficulty tracking material boundaries, we have implemented a particle-based, Lagrangian model (Smoothed Particle Hydrodynamics). We treat the debris flow as an incompressible, viscous fluid and the body of water as inviscid. We use this model to simulate the 1958 Lituya Bay rockslide and resulting tsunami. Our simulation results compare favorably with field observations as well as a scaled laboratory experiment and numerical studies.

2.1 Introduction

In contrast to submarine landslides, subaerial landslides, can attain high velocities before impacting the water and generating waves. These subaerial landslide events can lead to significant damage as, for example, with the 1963 breech of the Vaiont Reservoir in Italy resulting in the destruction of the town of Longarone and the deaths of 2000 people [125] They can also produce a wave height and run-up significantly greater than other tsunamigenic mechanisms as, for example, the 1958 Lituya Bay rockslide [81] which produced the highest measured run-up (524 m) for any historic tsunami. The high-velocity impact can generate a large air cavity [98]. As a result, to numerically investigate the near-field wave characteristics of these subaerial landslides, the full Navier-Stokes equations should be used [74, 73]. Since the impact process involves the interaction of three phases (slide material, air, and water), the numerical method must be capable of tracking the large deformation of these material interfaces. For Eulerian, grid-based methods (as are typically used for fluid modeling), these material interfaces can be subjected to a numerical diffusion. Techniques such as adaptive mesh refining (AMR) [74] and the level-set method [105, 128], have successfully been used to mitigate the

effects of numerical diffusion and improve the tracking of material interfaces.

In this study, we test the feasibility of using Smoothed Particle Hydrodynamics (SPH), a mesh-free Lagrangian hydrocode, in studying this landslide-impact process. In contrast to grid-based Eulerian methods, in the SPH method, material is represented as a system of particles that follow deformation. As a result, the tracking of material interfaces (as well as material history) is an inherent feature of the numerical method. The particular event we model is the 1958 Lituya Bay rockslide.

2.2 Lituya Bay Rockslide

Lituya Bay (Figure 2.1) is a T-shaped bay in southeast Alaska with Gilbert Inlet to the north and Crillon Inlet to the south forming the branches of the 'T'. On the evening of 9 July, 1958, a magnitude 7.7 earthquake occurred along the Fairweather Fault. Within a few minutes, a rockslide was triggered on the northeast side of Gilbert Inlet. Although the slide itself was not witnessed, observers anchored at the western end of the bay reported waves emanating from Gilbert Inlet as well as "a big wall of water going over the point" (the spur southwest of Gilbert Inlet) [81].

The slide area is sketched in Figure 2.1 and was described by Miller [81] as a "prism of rock that is roughly triangular in cross section." The slide had a maximum thickness of approximately 92 m, a total volume of $30.6 \times 10^6 \mathrm{m}^3$ and a center of mass at an elevation of 610 m.

2.2.1 Previous Models

Some of the early laboratory work on tsunamigenic landslides [see Slingerland and Voight [125] and references therein] found slide thickness to be an important parameter in characterizing far-field waves. This has provided some guidance in specifying source terms for modeling the subsequent tsunami, however large discrepancies in the near-field run-up may remain. For example, in the case of Lituya Bay, a tsunami model using a depth-integrated, shallow water tsunami-propagation code (SWAN) and using an instantaneous water displacement of the landslide volume, found that the run-up immediately opposite the slide was underestimated by an order of magnitude [72].

Fritz et al. [35] simulated the impact event and subsequent run-up using a Froude-similar scaled laboratory model (Figure 2.3b). The rockslide was simulated by a granular material driven by a pneumatic acceleration mechanism so that the impact characteristics could be controlled. Using a two-dimensional simplified cross-section, Fritz et al. measured run-up values (526 m) in agreement with observations. In their experiments, a large air cavity was generated by the impact (Figure 2.3b).

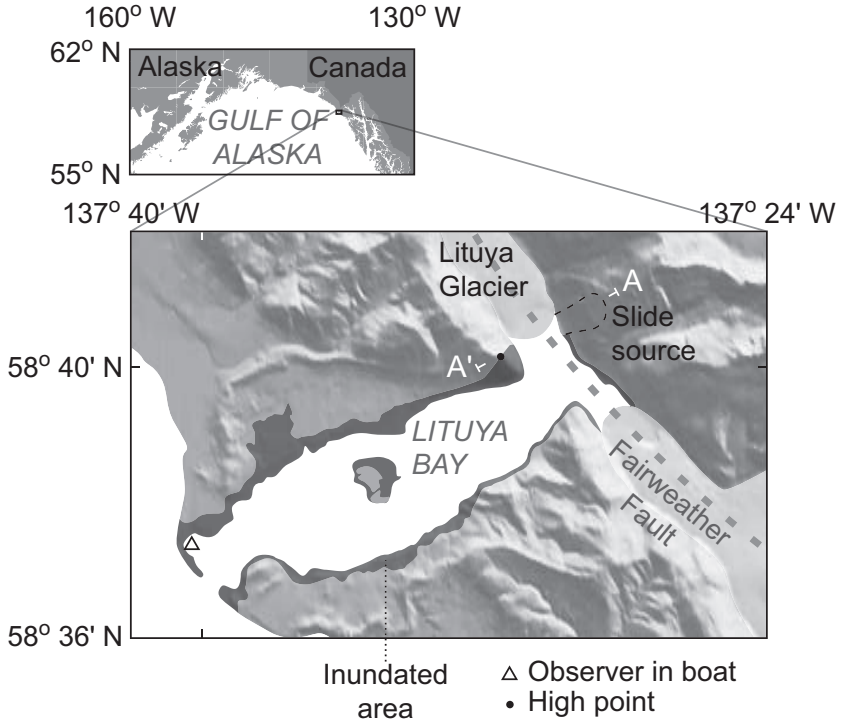

Figure 2.1: Lituya Bay, Alaska.

Mader and Gittings [74] subsequently numerically modeled the impact process using the same initial geometry as described by Fritz et al. [35] using a full Navier-Stokes AMR Eulerian compressible hydrodynamics code (SAGE). The numerical results also showed an air cavity formation and produced a run-up consistent with observation (580 m). Quecedo et al. [105] also modeled the Lituya rockslide with the same initial geometry using an Eulerian mesh and a characteristic based Galerkin (CBG) solver. They tracked material interfaces by advecting an indicator function. Their results are similar to that of Mader and Gittings [74].

Eulerian grid-based numerical methods are fast, but they have an inherent difficulty tracking material interfaces. Lagrangian grid-based methods can track these material interfaces, however, large deformation flows require frequent remeshing which also leads to a diffusion of the material interface. Mesh-free (particle) methods can be computationally more expensive since they often require a greater number of neighboring points (larger support region) to accurately calculate gradients, however they inherently track material histories and interfaces in large deformation flows. Recently, the near-field effects of impact-generated waves has been addressed using mesh-free, Lagrangian

methods [85, 39, 97].

2.3 Numerical Methodology

The mesh-free method we employ is Smoothed Particle Hydrodynamics (SPH) which, for free-surface flows, is described by Monaghan [82]. Colagrossi and Landrini [21] outline several modifications for multi-phase flows that become important when density contrasts become large. However, we found that for flows with a density contrast of 2.7 (as encountered in the present simulations), these modifications did not significantly alter wave height and run-up. All results presented here are generated by the formulations of Monaghan [82].

The SPH implementation of free-surface flows employs an artificial viscosity term which is activated by and is proportional to velocity convergence. This term behaves as a bulk viscosity and dampens spurious pressure oscillations. We use an artificial viscosity parameter of $\alpha = 0.1$ (for details, see [82]); lower values resulted in a more turbulent flow. Viscous shear stresses are calculated using a term developed by Morris et al. [89]. The results presented in this paper are from simulations with a Newtonian viscosity, however other rheologies have been successfully included in SPH simulations through a nonlinear viscosity (e.g. Mohr-Coulomb [94], Bingham [113], Bi-linear [120], Voellmy [77]).

It is unlikely that rockslides such as at Lituya Bay behave as a fluid with a Newtonian viscosity. However, this assumption allows maximal wave height and run-up values to be constrained while providing a mechanism to limit the transfer of gravitational potential energy to wave energy.

2.4 Comparison With Previous Models

2.4.1 Run-up on a steep slope

As an initial test of the reliability of this numerical method in predicting run-up on steep slopes, simulation results of the run-up of a solitary wave on a slope of 45° were compared with laboratory data (Figure 2.2). In these simulations, a surface profile and velocity field of the solitary wave were initialized as described in Monaghan and Kos [83]. Five cases were run with wave heights (H) in increments of 10 m from $H = 30$ m to 60 m. In each case, $D = 100$ m. Normalized run-up values are plotted in Figure 2.2b and compare favorably with experimental data.

2.4.2 Lituya Bay landslide impact models

Using the boundary and water geometry as described by Fritz et al. [35] and a triangular rockslide geometry with the thickness, elevation and mass described by Miller [81] (See Figure 2.3a), we

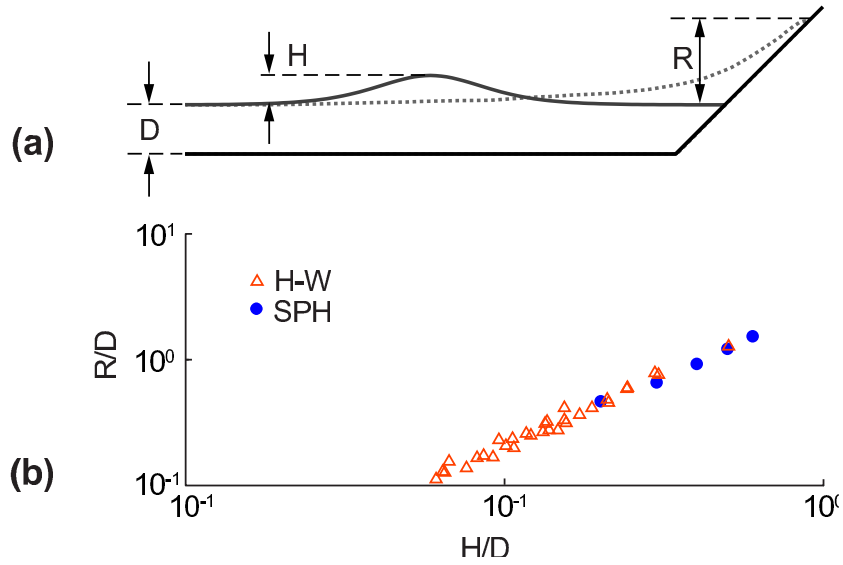

Figure 2.2: Simulation of the run-up of a solitary wave on a slope of 45°. Data in (b) are from Hall and Watts [47]

modeled the rockslide as a viscous fluid and obtained results with rockslide and water profiles which compare favorably with the laboratory results of Fritz et al. [35] (Figure 2.3b,c,d) for times greater than approximately 13 s after impact. Simulation results for earlier times differ due to differences in initial conditions. In the laboratory simulation, the mass and length of the slide were taken from observations of Miller [81], however the thickness of the slide was increased since the granular material used had a lower bulk density. This granular material was assigned an impact velocity assuming the material fell freely from the initial center of mass of the slide. In the SPH simulation, the mass, initial thickness, and density of the slide were all taken from Miller [81]. Additionally, since the material was allowed to slide from its initial position, the velocity of each fluid particle was different as it arrived at the impact point.

Increased viscous dissipation within the rockslide reduced the energy available to be transferred to the water (Figure 2.3e), resulting in a lower wave height. Differences can also be seen in the structure of the air cavity region for different viscosities. This is due primarily to changes in the shape of the front of the rockslide at impact. Increased shear stress at the base of the slide causes the front to develop a blunter profile. This effect can be seen in Figure 2.3f, where the time-dependent thickness of the slide near the point of impact is compared for different viscosities with data from the laboratory model of Fritz et al. [35]. The profiles of the SPH solutions of the viscous slides differ significantly from the measured profile of the granular material due to the different initial geometry

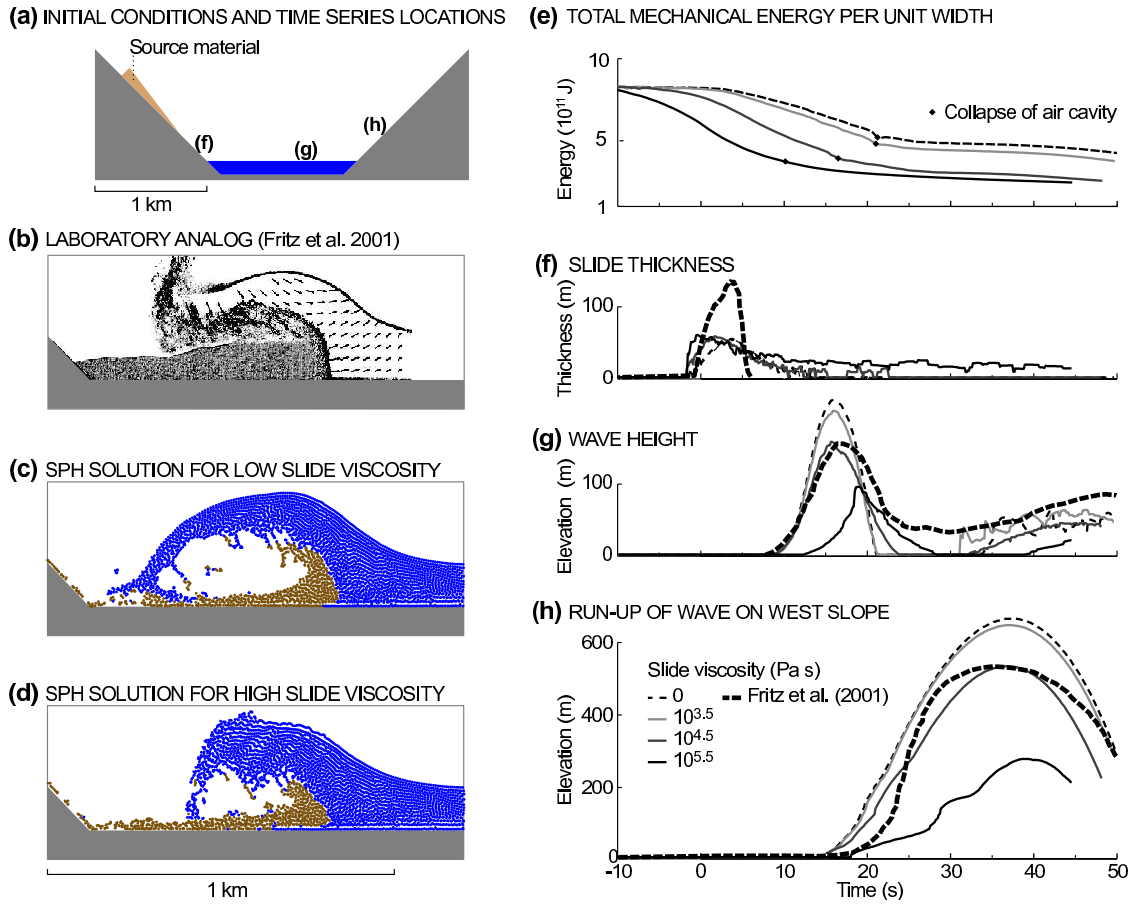

Figure 2.3: Comparison of SPH solution with laboratory model of Fritz et al. [35]. The initial configuration is shown in (a). The photograph in (b) shows the laboratory results of Fritz et al. [35] at 12.9 s after impact. The SPH solutions presented are for (c) a rockslide viscosity of $\mu = 10^{3.5}\ Pa\,s$ and (d) a rockslide viscosity of $\mu = 10^{4.5}\ Pa\,s$ both at 12.9 s after impact. Water is treated as inviscid in each case and time is given as seconds after impact. In each of the graphs on the right, curves are plotted for SPH simulations with different rockslide viscosities (darker lines corresponding to higher viscosities). In (e), the total mechanical energy (kinetic and gravitational potential with respect to -122 m) per unit width is plotted. Plots (f)-(h) are comparisons of the SPH simulations with three time-series data sets of the laboratory model [35]: the profile of the impacting slide (measured as thickness of the slide at 67 m elevation), wave height at 885 m, and wave run-up.

Table 2.1: Comparison of run-up (R) and wave height (H_{wave}) for Lituya models.

	Wave Height (H_{wave})	Run-up (R)
Field [81]	?	524 m
Lab. [35]	154 m	526 m
AMR [74]	250 m	580 m
CBG [105]	227 m	600 m
SPH (invisc.)	213 m	671 m
SPH ($\mu = 10^4$Pa s)	156 m	531 m

and velocity structure at impact.

Despite these markedly different impacting profiles, the wave height at 885 m from the shore (Figure 2.3g) and the run-up (Figure 2.3h) are similar to that measured in the laboratory by Fritz et al. [35] and observed in the field [81]. The case of an inviscid rockslide produced a maximum wave height of 214 m at the wave gauge and a run-up of 662 m. This is to be compared with numerical results of [74] (250 m and 580 m) and of Quecedo et al. [105] (227 m and 600 m). In each of the numerical cases (SPH, AMR, CBG), both wave height and run-up values are greater than that measured by Fritz et al. [35] (154 m and 526 m for the wave height and run-up, respectively). Using a rockslide with a viscosity of $\mu = 10^{4.5}$ Pa s produces results much closer to the laboratory model with a wave height of 156 m and a run-up of 530 m. These values are summarized in Table 2.1 This value of viscosity effectively incorporates both the dissipation of energy through deformation as well as the energy lost through turbulence in the impact process. As can be seen in Figure 2.3e, there is a slight increase in the dissipation of mechanical energy prior to impact ($t = 0$) with increasing viscosity, however, the rate of energy dissipation is greatest after impact, but before the collapse of the air cavity. After the collapse of the air cavity, the bulk of the remaining total energy is in a large solitary wave with little dissipation of energy.

Hunt [52] noted that for waves generated by landslides in reservoirs, the primary factors which characterize far-field waves are the reservoir geometry and the volume of water displaced. Since it is possible that including a more detailed geometry of Gilbert Inlet than the simplified cross-section of Figure 2.3a might effect run-up values, models were also run using topography and bathymetry from Miller [81] along the transect A–A' (Figure 2.1). Including this geometry and using an initial slide geometry consistent with Miller's estimate of total mass, center of mass, maximal thickness and upper and lower scarp lines, did not significantly effect run-up values.

2.5 Discussion

As noted above, the viscosity used in this model should be interpreted as a proxy for the dissipation of mechanical energy within the slide. The mechanism of energy dissipation by internal deformation within the slide may be more accurately modeled by including plasticity using a non-linear viscosity, however the energy transfer from the impact is poorly constrained. Law and Brebner [61] estimate that 2–28% of the kinetic energy of the slide is transferred to wave energy, a fraction that is likely dependent on the structure of the splash zone. The structure of this region is, in part, dependent on the shape of the front of the impacting slide. This uncertainty is an issue with any numerical method, however with this caveat, SPH is a viable method for constraining maximal run-up values. As with the grid-based numerical methods, data from SPH simulations can be coupled to a shallow-water tsunami propagation code to more efficiently model far-field inundation from landslide generated waves.

Although it was not investigated in this study, the Lagrangian nature of the method eases the inclusion of additional energy dissipation mechanisms at material interfaces.

2.6 Appendix: Numerical Parameters

For completeness, the problem-dependent parameters necessary to reproduce these simulations are given here. For details of the algorithm, see Monaghan [82]. In all simulations presented, the smoothing kernel (W) used was the cubic-spline kernel with a characteristic width of $h = 1.2s$ where s is the initial particle spacing. For most of the simulations presented, $s = 7.5\,\mathrm{m}$. The simulations of low-amplitude solitary waves required a finer resolution ($s = 5\,\mathrm{m}$ and $3.5\,\mathrm{m}$ for $H = 20$ and $10\,\mathrm{m}$ respectively). Pressure is determined through an equation of state:

$$P = \frac{\rho_0}{\gamma} c_s^2 \left[\left(\frac{\rho}{\rho_0} \right)^{\gamma} - 1 \right]$$

where ρ_0 is the reference density of the material and c_s is the speed of sound, which, for shallow water flows, is given by $c_s = \sqrt{200gH}$ where H is the characteristic depth of the flow. In all the simulations presented, we used $\gamma = 7$ and $H = 50\,\mathrm{m}$.

Solid wall boundaries are imposed through the use of boundary particles that impart a central force to fluid particles according to the Lennard-Jones description:

$$\mathbf{a}_{lj} = D \left[\left(\frac{r_0}{r} \right)^{p_1} - \left(\frac{r_0}{r} \right)^{p_2} \right] \frac{\mathbf{r}}{r^2}$$

where $\mathbf{r}$ is the position of the fluid particle relative to the boundary particle. We take D to be gH,

$p_1 = 4$, $p_2 = 2$, and $r_0 = s$. The boundary particles were positioned with a spacing of approximately $0.5s$. These boundary particles are included in the SPH summation for the viscous term but not the pressure gradient term.

Acknowledgments

Figure 2.1 was generated using software GMT [139]

Chapter 3

AN IMPLICIT CORRECTED SPH FORMULATION FOR THERMAL DIFFUSION WITH LINEAR FREE-SURFACE BOUNDARY CONDITIONS

A version of this chapter with the same title was submitted to *International Journal for Numerical Methods in Engineering*.

The Smoothed Particle Hydrodynamics (SPH) method has proven useful for modeling large deformation of fluids including fluids with stress-free surfaces. Because of the Lagrangian nature of the method, it is well suited to address the thermal evolution of these free-surface flows. Boundary conditions at the interface of the fluid with a solid wall are usually enforced through the use of boundary particles. However, applying conditions at surfaces, in particular gradient boundary conditions, can be problematic with traditional SPH formulations due to the degradation of the gradient approximation in these regions. Compounding this difficulty is that traditional approximations of the Laplacian operator suffer a similar degradation near surfaces. A new SPH formulation of the Laplacian operator is presented which improves the accuracy near surface boundaries. This new form is based on a gradient approximation commonly used in thermal, viscous, and pressure projection problems, but includes higher order terms in the appropriate Taylor series. Comparisons with other approximations of second-order derivatives are given. The discretization is tested by solving steady-state and transient problems of thermal diffusion using the Backward Euler method with a GMRES solver. Boundary conditions are imposed through an augmented matrix.

3.1 Introduction

Smoothed Particle Hydrodynamics (SPH) [84] was developed approximately 30 years ago to model inviscid fluid dynamics in astrophysical problems. SPH is a mesh-free, Lagrangian method in which the "particles" correspond to small parcels of fluid. "Smoothed" refers to the procedure for calculating state variables, such as density, in which the function value at a point is determined as a weighted average of values in a local region. One advantage of this formulation is that numerical effort is concentrated in regions of higher fluid density. In regions where density approaches zero, the distribution of particles becomes sparse and the averaging kernel used in determining neighboring

particles' contributions loses part of its support region. This loss of support results in a numerical approximation that also approaches zero. For fluids with diffuse boundaries such as in gas dynamics, the particle deficiency near boundaries does not pose serious problems and in fact is presented as an automatic incorporation of the correct temperature and density boundary condition [71]. The success of SPH in modeling gas dynamics has led to its application in many branches of fluid and solid mechanics, most notably free-surface flows [82], elastoplasticity [17] and impact dynamics [56]. For these problems, however, care must be taken to ensure that variables whose values do not approach zero at boundaries are accurately represented.

For the purposes of this chapter, the governing equation is that of thermal diffusion given by

$$\frac{\partial T}{\partial t} = \frac{1}{\rho c_p} \boldsymbol{\nabla} \cdot \left(k \boldsymbol{\nabla} T \right) \tag{3.1}$$

where T is the temperature, t is time, c_p is the specific heat, k is the thermal conductivity. This chapter only focuses on the problem of solving thermal diffusion in a static pool of fluid. The work of this chapter is intended to supplement a more complicated thermo-mechanical problem involving deformation. In the mechanical problem, the boundaries of the fluid are those formed at the walls of the container as well as possibly a free-surface. 'Free-surface' refers to the stress-free condition at the surface where $\boldsymbol{\sigma} \cdot \boldsymbol{n} = \mathbf{0}$ where $\boldsymbol{n}$ is the unit normal to the surface. This is a mechanical boundary condition and has no effect on the thermal problem. However, boundary conditions for any variable such as temperature, velocity, or pressure, are generally treated differently at boundaries defined by the walls of a container and those defined by the stress-free mechanical condition. This is because it is straight-forward to fill walls with ghost particles that can be used to enforce whatever boundary condition is needed at the walls. The free-surface mechanical boundary condition results in a configuration of particles that locally appears like a half-space. There are no supplemental particles to enforce boundary conditions for any of temperature, velocity, or pressure in these locations. In fact, traditionally in SPH, no boundary conditions are even enforced at these surfaces. This chapter aims to remedy this deficiency by a more careful treatment of boundary conditions in the vicinity of these surfaces. Note, 'surface' or 'free-surface' is suggestive of a mechanical boundary condition and is not meant to have any implications for the type (Dirichlet, Neumann, or mixed) of boundary condition in the thermal problem. Throughout this chapter, any use of the term 'surface' or 'free-surface' should be interpreted only to have implications on the local geometry of the particles, namely, the particle configuration that locally (on the scale of the kernel width) appear like a half-space. This chapter describes a method of improving the accuracy in the vicinity of these surfaces and imposing boundary conditions on these surfaces.

The standard SPH spatial discretization of a function f arises from the following sequence of approximations:

$$\begin{aligned} f(x) = \int_\Omega f(x')\delta(x-x')\,\mathrm{d}x' &\simeq \int_\Omega f(x')W(x-x',h)\,\mathrm{d}x' \\ &\simeq \sum_j f(x_j)W(x-x_j,h)\varphi_j \end{aligned} \tag{3.2}$$

where δ is the Dirac delta function, W is the kernel which approximates δ but with finite characteristic width (h), φ_j is the discrete volume element equal to the ratio of the particle's mass to its density (m_j/ρ_j), and Ω is the domain. The subscript j in the equation above, as well as all Latin indices throughout this paper, correspond to particle numbers; Greek indices correspond to coordinate numbers. The standard form of spatial derivative of a function f can be determined from integrating Eq. 3.2 by parts. If the kernel has compact support (i.e., is identically zero beyond a fixed radius) the boundary term from the integration by parts can be neglected, resulting in the following approximations:

$$f(x)_{,\alpha} \simeq \int_\Omega f(x')W_{,\alpha}\,\mathrm{d}x' \qquad f(x)_{,\alpha\beta} \simeq \int_\Omega f(x')W_{,\alpha\beta}\,\mathrm{d}x' \tag{3.3}$$

where the comma denotes partial differentiation with respect to the given coordinate. The second-order derivative results from a second integration by parts. Usually, to ensure that constant functions have an identically zero discrete gradient and curvature [15], the identities $(A)_{,\alpha} = (1\cdot A)_{,\alpha} - (1_{,\alpha})\cdot A$ and $(A)_{,\alpha\beta} = (1\cdot A)_{,\alpha\beta} - (1_{,\alpha\beta})\cdot A$ are invoked resulting in

$$f(x)_{,\alpha} \simeq \int_\Omega \big(f(x') - f(x)\big)W_{,\alpha}\,\mathrm{d}x' \qquad f(x)_{,\alpha\beta} \simeq \int_\Omega \big(f(x') - f(x)\big)W_{,\alpha\beta}\,\mathrm{d}x' \tag{3.4}$$

The assumption that the boundary terms from the integration by parts is zero in Eq.s 3.4 is only valid in regions where the kernel has full support. For particles near surfaces, the neglect of these terms leads to significant errors. Several authors have addressed these errors through various correction methods, some by calculating the boundary integrals [14], others by applying correction transformations in the derivative approximations [58, 2]. Approximations can also be corrected by basing SPH discretization on higher order Taylor series approximations [18, 16, 17, 67, 147] or by generating correction terms which require that the discrete equations reproduce linear fields [112, 7, 5, 6] or polynomials up to a given order [69, 68]. These methods are particularly successful in correcting the approximations of function gradients near boundaries, however, corrections to the second-order derivatives require significantly more work, particularly the Taylor series approximations, which

involve calculating all second-order derivatives.

Correction terms have also been generated for the Laplacian discretization based on Eq. 3.3 by requiring that the discrete Laplacian be zero for constant and linear functions, and constant for quadratic functions [5]. Approximations using second-order derivatives of the kernel, however, as in Eq.'s 3.3 or 3.4, are often noisy and sensitive to particle disorder, particularly for spline kernels of lower-order [9]. To avoid the use of these second-order kernel derivatives, Brookshaw [9] introduced an approximation of the Laplacian that only requires first-order derivatives, given by:

$$\boldsymbol{\nabla}\cdot\left(\tau\boldsymbol{\nabla}f_i\right) = \sum_j \varphi_j(\tau_j+\tau_i)(f_j-f_i)\frac{\left(x_j-x_i\right)_{,\alpha}\cdot\boldsymbol{\nabla}\, W_{,\alpha}}{|x_j-x_i|^2} \tag{3.5}$$

where the repeated index α denotes summation over that coordinate. Brookshaw introduced this form of the Laplacian operator in the context of thermal conduction (in which τ is the thermal conductivity and f is the temperature) where it continues to be successfully used, though in a slightly modified form [20, 57]. Morris et al. [89] successfully employed the Brookshaw form of the Laplacian in modeling viscous diffusion, although Watkins et al. [137] noted that this form is sensitive to perturbations in velocity. This form continues to be commonly used in viscous flow simulations [55] and is often coupled [99, 120, 115] with an analogous form of a pressure Poisson equation [23]. Second-order derivatives can often be avoided entirely if the PDE is cast in weak form [58] or in a variational formulation [5, 6] in which case only the gradient correction is needed. Nevertheless, the Brookshaw formulation of the Laplacian is widely used. In this work, a correction term to the Brookshaw formulation is introduced (based on a Taylor series expansion) which significantly improves the accuracy of this Laplacian operator near boundaries.

This paper is organized as follows. In section 3.2, the correction term to Eq. 3.5 is derived and its performance reproducing a variety of test functions demonstrated. Section 3.3 describes the implementation of boundary conditions at both solid-wall boundaries and surfaces. In section 3.4, the corrected form is applied to both steady-state and transient thermal conduction problems.

3.2 Corrected SPH Discretization of the Laplacian

3.2.1 Taylor Series Approximation

The corrected forms of f and ∇f used in this paper are those outlined by Chen et al. [18] and are derived from the Taylor series expansion about the point x_i.

$$f(x) = f(x_i) + f_{,\alpha}(x_i)[x-x_i]_\alpha + \frac{1}{2}f_{,\alpha\beta}(x_i)[x-x_i]_\alpha[x-x_i]_\beta + \cdots \tag{3.6}$$

Again, the Greek indices correspond to coordinate direction, the Latin index corresponds to the particle index, and the comma denotes partial differentiation.

The corrected form of $f(x_i)$ is found by multiplying the Taylor series by $W(x - x_i, h)$ and integrating over the region Ω:

$$f(x_i) \int_\Omega W \, \mathrm{d}x = \int_\Omega W f(x) - \int_\Omega W f_{,\alpha}(x_i)[x - x_i]_\alpha \, \mathrm{d}x + \cdots \tag{3.7}$$

$$f(x_i) \simeq \frac{1}{\mathcal{V}} \int_\Omega W f(x) \, \mathrm{d}x \tag{3.8}$$

where $\mathcal{V} = \int_\Omega W \, \mathrm{d}x$ is the kernel volume.

For the corrected form of $\boldsymbol{\nabla} f(x_i)$, Eq. 3.6 is multiplied by $\boldsymbol{\nabla} W$ and integrated:

$$f_{,\alpha}(x_i) \int_\Omega \left[(\Delta x)_\alpha \, W_{,\beta} \right] \, \mathrm{d}x = \int_\Omega \left[(f(x) - f(x_i)) \, W_{,\beta} \right] \, \mathrm{d}x + \cdots \tag{3.9}$$

where $\Delta x = x - x_i$. By defining

$$\mathbf{C}_{\alpha\beta} = \left[\int_\Omega \left[(\Delta x)_\alpha \, W_{,\beta} \right] \, \mathrm{d}x \right]^{-1} \tag{3.10}$$

Eq. 3.9 can be rewritten as:

$$f_{,\alpha}(x_i) \simeq \int_\Omega \left[(f(x) - f(x_i)) \, \mathbf{C}_{\alpha\beta} \boldsymbol{\nabla} W_\beta \right] \, \mathrm{d}x \tag{3.11}$$

To calculate the second derivatives of f, Chen et al. [18] multiplied Eq. 3.6 by $W_{,\gamma\delta}$ and solved for $f_{,\alpha\beta}$. The Taylor series approximation can be written as

$$\frac{1}{2} f_{,\alpha\beta} \int_\Omega (\Delta x)_\alpha (\Delta x)_\beta W_{,\gamma\delta} \, \mathrm{d}x \simeq \int_\Omega (f(x) - f(x_i)) W_{,\gamma\delta} \, \mathrm{d}x - f_{,\alpha} \int_\Omega (\Delta x)_\alpha W_{,\gamma\delta} \, \mathrm{d}x \tag{3.12}$$

where $f_{,\alpha}$ in the second term on the right-hand-side of Eq. 3.12 is calculated from Eq. 3.11. Although the integrand on the left-hand-side of Eq. 3.12 is a fourth-order tensor, it is symmetric in the pairs i, j and α, β. Eq. 3.12 can therefore be written in discrete form as

$$B_{\eta\xi} F_\xi = \Phi_\eta \tag{3.13}$$

where

$$\begin{aligned} B_{\eta\xi} &= (1-\delta_{\alpha\beta})\sum_{j=1}^{N}\varphi_j(x_j-x_i)_\alpha(x_j-x_i)_\beta W_{,\gamma\delta} \\ \Phi_\eta &= \sum_{j=1}^{N}\varphi_j(f(x_j)-f(x_i))W_{,\gamma\delta} - f_{,\alpha}(x_i)\sum_{j=1}^{N}\varphi_j(f(x_j)(x_j-x_i)_\alpha W_{,\gamma\delta} \end{aligned}$$

and $\delta_{\alpha\beta}$ is the Kronecker delta. Since the Hessian ($f_{,\alpha\beta}$) is symmetric, the number of independent variables in $F_\xi = f_{,\alpha\beta}$ is 3 and 6 for 2- and 3-dimensional problems respectively with ξ and η each mapping to $\alpha\beta$ pairs according to : $1 \leftrightarrow 11$, $2 \leftrightarrow 22$, $3 \leftrightarrow 33$, $4 \leftrightarrow 12$, $5 \leftrightarrow 23$, $6 \leftrightarrow 13$ [18]. In 2-dimensional problems, a 3-by-3 matrix ($B_{\eta\xi}$) must be inverted at each particle, while a 3-dimensional problem requires inverting a 6-by-6 matrix to solve for all independent $f_{,\alpha\beta}$. In recent papers [147, 67], it has been noted that the approximation of the Hessian can be further improved if the values of the function and its gradient (f and $f_{,\alpha}$) are simultaneously solved.

In many problems, second derivatives appear only in the form of the Laplacian operator. In these cases, the full Hessian is not required, only its trace. The Brookshaw form of the Laplacian only requires first derivatives [9] and is derived by multiplying Eq. 3.6 by $\frac{(\Delta x)_\alpha W_{,\alpha}}{|\Delta x|^2}$ and integrating [57].

$$\begin{aligned} f_{,\beta\gamma}(x_i)\int_\Omega \frac{(\Delta x)_\alpha W_{,\alpha}}{|\Delta x|^2}(\Delta x)_\beta(\Delta x)_\gamma \,\mathrm{d}x &= 2\int_\Omega (f(x)-f(x_i))\frac{(\Delta x)_\alpha W_{,\alpha}}{|\Delta x|^2}\,\mathrm{d}x \\ &\quad -2\int_\Omega \frac{(\Delta x)_\alpha W_{,\alpha}}{|\Delta x|^2} f_{,\beta}(x_i)(\Delta x)_\beta \,\mathrm{d}x + \cdots \end{aligned} \tag{3.14}$$

For a one-dimensional problem, the integral on the left-hand-side of Eq. 3.14 is a scalar and can simply be moved to the right-hand-side. For multi-dimensional problems, the integral is a matrix coupled to $f_{,\beta\gamma}$ through an inner product. However, setting

$$\begin{aligned} \mathbf{\Gamma}_{\beta\gamma} &= \int_\Omega \frac{(\Delta x)_\alpha W_{,\alpha}}{|\Delta x|^2}(\Delta x)_\beta(\Delta x)_\gamma \,\mathrm{d}x \\ &\simeq \delta_{\beta\gamma} \quad \text{(If the support domain is entire and the kernel symmetric.)} \end{aligned}$$

then

$$\begin{aligned} \boldsymbol{\nabla}^2 f(x_i) &= \mathrm{tr}\left[f_{,\alpha\beta}(x_i)\right] \\ &\simeq \mathbf{\Gamma}_{\alpha\beta} f_{,\alpha\beta}(x_i) \qquad (3.15) \\ &\simeq 2\int_\Omega (f(x)-f(x_i))\frac{(\Delta x)_\alpha W_{,\alpha}}{|\Delta x|^2}\,\mathrm{d}x - 2\int_\Omega W_{,\alpha} f_{,\alpha}(x_i)\,\mathrm{d}x \qquad (3.16) \end{aligned}$$

The inhomogeneous form of the Laplacian can be derived by repeated use of Eq. 3.16 in the following identity.

$$\boldsymbol{\nabla}\cdot\left(\tau\boldsymbol{\nabla}f\right) = \frac{1}{2}\left[\boldsymbol{\nabla}^2(\tau f) - f\boldsymbol{\nabla}^2\tau + \tau\boldsymbol{\nabla}^2 f\right] \tag{3.17}$$

Neglecting the second term on the right-hand-side (RHS) of Eq. 3.16 results in the Laplacian operator given by Brookshaw in Eq. 3.5. The second term on the RHS is the correction which gives a modest improvement over just the first term (Figures 3.1-3.4). If the gradient of f in the correction term is calculated using Eq. 3.11, the error is further reduced at the boundary.

An underlying assumption in this approximation is that $\boldsymbol{\Gamma}_{\beta\gamma} \simeq \delta_{\beta\gamma}$ throughout the domain, including regions near the boundaries. In fact, $\boldsymbol{\Gamma}_{\beta\gamma}$ deviates from $\delta_{\beta\gamma}$ in these regions. Unfortunately, since $\boldsymbol{\Gamma}_{\alpha\beta}$ and $f_{,\alpha\beta}$ are coupled through a tensor inner product, it is difficult to isolate $f_{,\alpha\beta}$. However, denoting the RHS of Eq. 3.16 as $\mathcal{L}$, and using the identity $\mathbf{A} : \mathbf{B} = \mathrm{tr}\left[\mathbf{A}\mathbf{B}^T\right]$, along with the fact that both $\boldsymbol{\Gamma}_{\alpha\beta}$ and $f_{,\alpha\beta}$ are symmetric, Eq. 3.16 can be expressed as:

$$\boldsymbol{\Gamma}_{\alpha\beta} f_{,\alpha\beta} = \mathcal{L} \tag{3.18}$$

$$f_{,\beta\gamma} = \frac{\mathcal{L}}{n}\boldsymbol{\Gamma}^{-1}_{\beta\gamma} + \boldsymbol{\Gamma}^{-1}_{\beta\alpha}\mathbf{W}_{\alpha\gamma} \tag{3.19}$$

$$\boldsymbol{\nabla}^2 f = \mathrm{tr}\left[f_{,\beta\gamma}\right] = \mathcal{L}\frac{\boldsymbol{\Gamma}^{-1}_{\alpha\alpha}}{n} + \left(\boldsymbol{\Gamma}^{-1}_{\alpha\beta} : \mathbf{W}_{\alpha\beta}\right) \tag{3.20}$$

where n is the number of dimensions and $\mathbf{W}$ is a tensor with zero trace. Converting the tensor-inner product of Eq. 3.18 to the tensor product so that $\Gamma_{\alpha\beta}$ can be inverted in Eq. 3.19 is essentially converting a scalar equation to a consistent matrix equation and therefore involves accounting for the additional unknowns through the matrix $\mathbf{W}$. Isolating $f_{,\beta\gamma}$ and extracting the trace modifies the original estimate of the Laplacian by a multiplicative factor $\boldsymbol{\Gamma}^{-1}_{\alpha\alpha}/n$, however an additive factor remains associated with the unknowns in $\mathbf{W}$.

Note that the crux of the difficulty here is that Eq. 3.20 is an attempt to circumvent the calculation of cross-derivative terms when in fact these terms do affect the estimate of the Laplacian when $\boldsymbol{\Gamma}_{\alpha\beta}$ has non-zero off-diagonal elements. The structure of $\mathbf{W}$ can be seen from Eq. 3.19 and is given by $\mathbf{W}_{\alpha\beta} = \boldsymbol{\Gamma}_{\alpha\gamma} f_{,\gamma\beta} - \delta_{\alpha\beta}\mathcal{L}/n$. If $\boldsymbol{\Gamma}_{\alpha\gamma} = \delta_{\alpha\gamma}$, these unknown cross-derivative terms are the off-diagonal terms of $\mathbf{W}$, but they do not effect the Laplacian since $\mathbf{W}$ has a trace of zero. When $\boldsymbol{\Gamma}_{\alpha\gamma}$ significantly differs from $\delta_{\alpha\gamma}$, then the cross-derivative terms are expected to play a more significant role and possibly degrade the approximation. A safer approach is to use the CSPM method [18], or variant thereof such as the MSPH approach [147], and calculate the full Hessian. However, this is computationally expensive as it requires inverting larger matrices, particularly in three-dimensional problems. In section 3.2.3 the performance of several of these approximations in the vicinity of

boundaries is shown.

3.2.2 Discrete Equations

The discrete form of the operators outlined in the previous section is tabulated below.

$$\langle f(x_i)\rangle \simeq \frac{1}{\mathcal{V}}\sum_j \varphi_j f_j W \tag{3.21}$$

$$\langle \boldsymbol{\nabla} f(x_i)\rangle \simeq \sum_j \varphi_j \left(f(x_j)-f(x_i)\right)\mathbf{C}_{\alpha\beta}W_{,\beta} \tag{3.22}$$

$$\begin{aligned}\left\langle \boldsymbol{\nabla}^2 f(x_i)\right\rangle \simeq \frac{\boldsymbol{\Gamma}^{-1}_{\beta\beta}}{n}\Bigg\{ & 2\sum_j \varphi_j\left(f(x_j)-f(x_i)\right)\frac{(x_{ij})_\alpha W_{,\alpha}}{|x_{ij}|^2} \\ & -2f_{,\alpha}(x_i)\cdot\Big[\sum_j \varphi_j W_{,\alpha}\Big]\Bigg\}\end{aligned} \tag{3.23}$$

$$\begin{aligned}\Big\langle \boldsymbol{\nabla}\cdot\left(\tau\boldsymbol{\nabla} f(x_i)\right)\Big\rangle \simeq \frac{\boldsymbol{\Gamma}^{-1}_{\beta\beta}}{n}\Bigg\{ & \sum_j \varphi_j\left(\tau_j+\tau_i\right)\left(f(x_j)-f(x_i)\right)\frac{(x_{ij})_\alpha W_{,\alpha}}{|x_{ij}|^2} \\ & -\Big[\big(\tau_i f(x_i)\big)_{,\alpha}-f(x_i)\tau_{i,\alpha}+\tau_i f_{,\alpha}(x_i)\Big]\cdot\Big[\sum_j \varphi_j W_{,\alpha}\Big]\Bigg\}\end{aligned} \tag{3.24}$$

In these equations, $x_{ij}=x_j-x_i$ and $\varphi_j=m_j/\rho_j$. The gradients in the second terms of the Laplacian discretization are previously determined from Eq. 3.22. Without the correction term and assuming $\boldsymbol{\Gamma}_{\alpha\beta}=\delta_{\alpha\beta}$, the Laplacian term reduces to the form commonly used in the literature for thermal [20, 57], viscous [89, 99, 120], and pressure projection [23, 115, 120] problems:

$$\frac{1}{\rho}\Big[\boldsymbol{\nabla}\cdot\left(k\boldsymbol{\nabla}T\right)\Big] = \frac{1}{\rho_i}\sum_j 2\langle k\rangle\left(T_j-T_i\right)\frac{(x_{ij})_\alpha W_{,\alpha}}{|x_{ij}|^2}\varphi_j \tag{3.25}$$

$$\frac{1}{\rho}\Big[\boldsymbol{\nabla}\cdot\left(\mu\boldsymbol{\nabla}\boldsymbol{v}\right)\Big] = \frac{1}{\rho_i}\sum_j 2\langle\mu\rangle\left(\boldsymbol{v}_j-\boldsymbol{v}_i\right)_\alpha\frac{(x_{ij})_\beta W_{,\beta}}{|x_{ij}|^2}\varphi_j \tag{3.26}$$

$$\Big[\boldsymbol{\nabla}\cdot\Big(\frac{1}{\rho}\boldsymbol{\nabla}P\Big)\Big] = \sum_j 2\Big\langle\frac{1}{\rho}\Big\rangle(P_j-P_i)\frac{(x_{ij})_\alpha W_{,\alpha}}{|x_{ij}|^2}\varphi_j \tag{3.27}$$

where $\langle\rangle$ term is an average "conductivity". The Taylor series suggests the average should be the arithmetic average, which is the form used by Morris et al. [89] for viscous diffusion. Cleary and Monaghan [20] use a different form in thermal conduction which guarantees continuity of heat flux. Cummins and Rudman [23] and Shao and Lo [120] each choose yet different forms for pressure Poisson equations.

3.2.3 Patch Tests

To quantify the accuracy of the proposed correction, the ability of the discretization to reproduce the Laplacian was tested for several functions. In all of the following tests, a two-dimensional domain was used with results displayed along the cross-section $y = 2.5$. In each test, the following discretizations are compared: Standard SPH (SSPH) given by Eq. 3.4 [15], Corrective Smoothed Particle Method (CSPM) given by Eq. 3.13 [18], gradient (Brookshaw) form of Laplacian (SPH1) given by Eq. 3.5, two-term gradient form of the Laplacian using Eq. 3.23 but with an uncorrected second term (SPH2); two-term gradient form of the Laplacian with a corrected second term (CSPH2), and finally the full form given by Eq. 3.23 including the correction from $\mathbf{\Gamma}^{-1}_{\alpha\beta}$. The motivation for displaying such a variety of methods is to demonstrate the incremental improvement for each additional correction. For example, including an uncorrected second term in Eq. 3.23 and assuming $\mathbf{\Gamma}_{\alpha\beta} = \delta_{\alpha\beta}$ leads to a modest improvement while remaining a relatively simple addition to one's program. Modifying one's program to calculate corrected gradients is not trivial and requires significant additional numerical effort (inverting an n-by-n matrix at each particle, where n is the number of dimensions) and storage costs, but the improvement is dramatic. Including the correction from $\mathbf{\Gamma}^{-1}_{\alpha\beta}$ requires yet another n-by-n matrix inversion.

The first class of test functions used is of the form $(x^m + y^m)$. Plots of the Laplacian approximations and the relative errors for the case $m = 3$ are shown in Figure 3.1. The domain for these cases is a unit square $(2 < x < 3, 2 < y < 3)$ with an array of 50-by-50 particles (average spacing $= s = 0.02$, $h = 1.2\ s$). A quintic spline kernel was used [89].

The CSPM formulation has the greatest accuracy at the boundary and is accurate to machine ϵ in the interior. The forms of Eq. 3.23 with a corrected gradient also performed nearly as well as CSPM, with CSPH2Γ also accurate to machine ϵ in the interior. A close-up of the right edge of the error plot is shown in Figure 3.2 along with test functions with exponents from $m = 2 \ldots 6$. For these functions, the CSPM and CSPH2Γ are uniformly more accurate although the difference decreases with increasing exponent.

For the functions in Figures 3.1 and 3.2, $f_{,\alpha\beta}$ has non-zero terms only along the diagonal, so it might be expected that the CSPH2 forms would not deteriorate much from the neglect of the cross-derivatives. To examine the effect of the cross-derivative terms, the same suite of tests was run with the function $(xy)^m$. The results are shown in Figure 3.3. The behavior of each discretization is similar to that shown in Figure 3.2. Both CSPH2 forms perform nearly as well as the CSPM form at the boundary. The CSPH2Γ and CSPM forms also perform with greater accuracy than all other forms in the interior except in the case with the highest exponent.

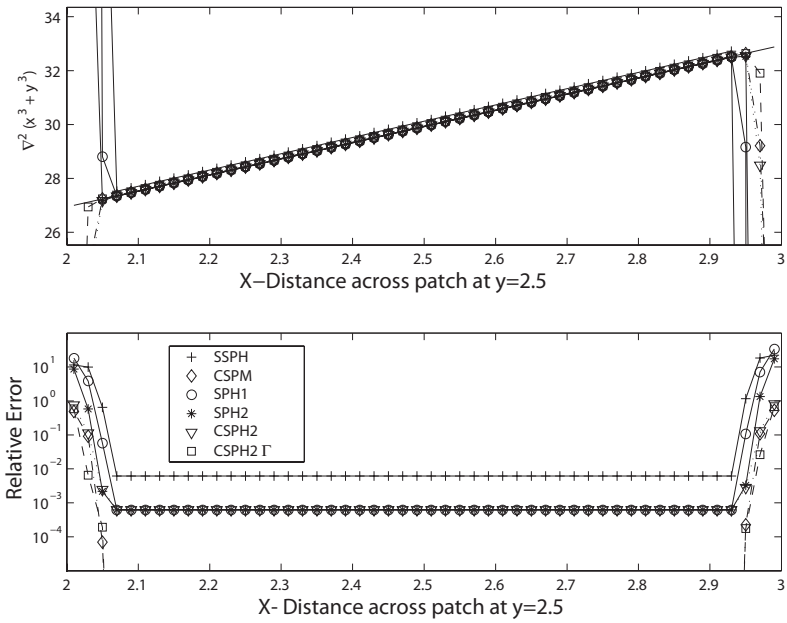

Figure 3.1: Cross section of test patch at $y = 2.5$. Several SPH approximations of $\nabla^2(x^3 + y^3)$ are shown. The Standard (SSPH) form is given by Eq. 3.4, while the CSPM [18] form is given by Eq. 3.13 and the commonly-used Brookshaw form (SPH1) is given by the first term of Eq. 3.23. New approximations to consider are the SPH2 form (Eq. 3.23 with both terms), the CSPH2 form (SPH2 with the gradient in the second term corrected using Eq. 3.22), and the CSPH2Γ form (Eq. 3.23). In this case the CSPH2, CSPH2Γ and CSPM forms have comparable accuracy at the boundaries, but the CSPH2Γ and CSPM are accurate in the interior to machine ϵ.

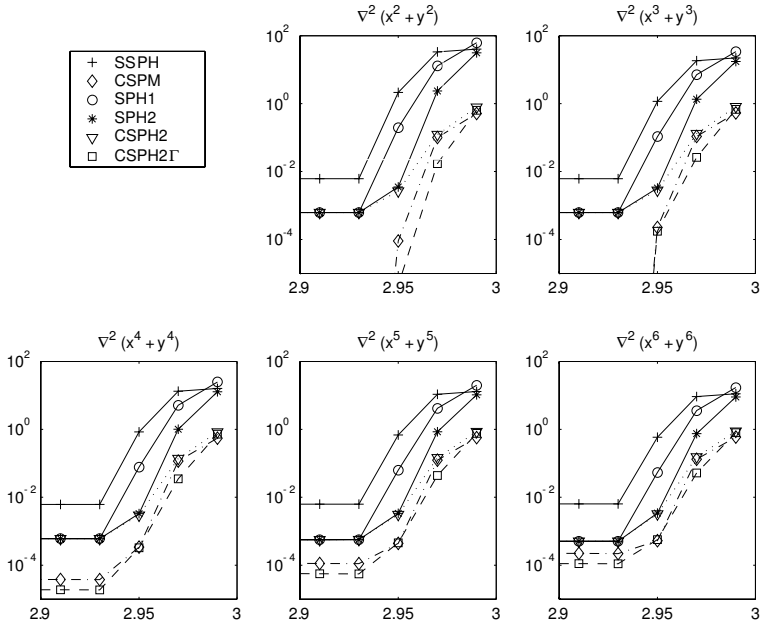

Figure 3.2: The relative errors along $y = 2.5$ for each of the discretizations used in Fig. 3.1 is shown here only at the right boundary for the suite of functions $\nabla^2(x^m + y^m)$ where $m = 2 \ldots 6$.

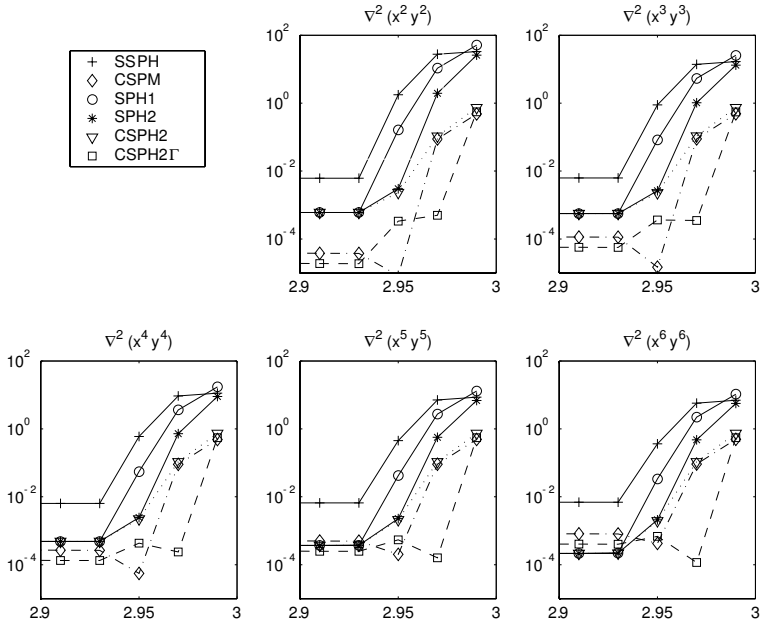

Figure 3.3: Relative errors for $(xy)^m$ on a same array as in Fig. 3.2 along $y = 2.5$.

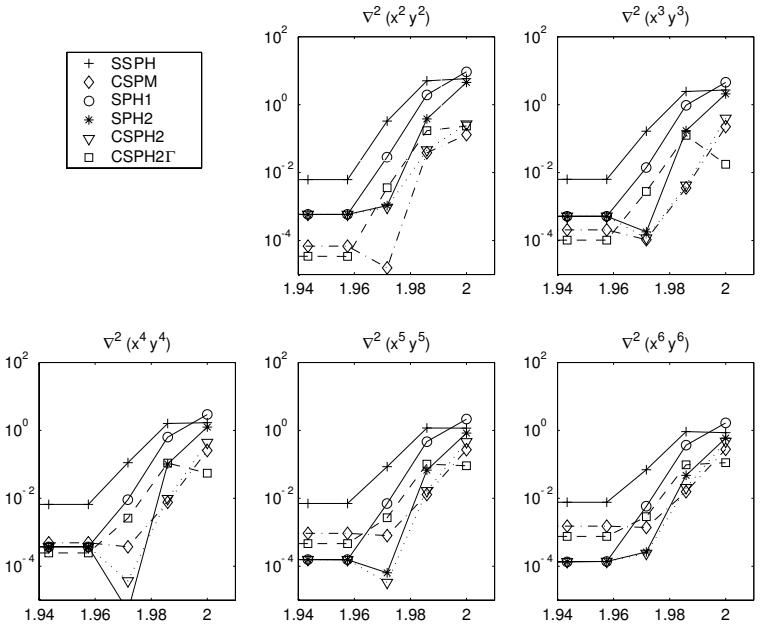

Figure 3.4: Relative errors for $(xy)^m$ on a array rotated 45° along $x = y$.

An additional concern is that, although $\Gamma_{\alpha\beta}$ deviates from $\delta_{\alpha\beta}$ near boundaries, it acquires no off-diagonal terms due to the alignment of the array of particles and the boundaries with the coordinate axes. To test the accuracy of the new approximations when $\Gamma_{\alpha\beta}$ has off-diagonal terms, a array with particles rotated 45° was used with the test function $(xy)^m$. The results along the cross-section $x = y$ are shown in Figure 3.4. The CSPM formulation performs consistently well for lower exponents. For higher exponents, the CSPH2 form has the lowest error near the boundaries. The CSPH2Γ form is clearly degraded in the vicinity of the boundary, though for lower-order functions it is still a reliable improvement over the one-term gradient approximation.

3.2.4 Convergence Tests

In section 3.2.3, the behavior of several Laplacian discretizations in the vicinity of boundaries was reported, however the performance of these discretizations in regions of full kernel support remains to be quantified. The tests of the previous section employed a regularly spaced array of particles with $s = 0.02$. To test the convergence properties of these discretizations, several other regularly spaced rectangular arrays were used with particle spacings of $s = 0.1$, 0.075, 0.05, 0.025, 0.01, and 0.0075. For the tests in this section, the same domain was employed as in section 3.2.3 with the same suite of Laplacian discretization applied to four test functions, $f = x^m + y^m$, $m = 2, 6$ and

$f = x^m y^m$, $m = 2, 6$. The quintic spline kernel was used in all cases with $h = 1.2s$. The accuracy of the approximations were quantified by calculating the integral of the relative error given by:

$$\text{Relative Error} = \left[\sum_i \left(\frac{\nabla^2 f_0 - \nabla^2 f_i}{\nabla^2 f_0} \right)^2 \varphi_i \right]^{0.5} \tag{3.28}$$

where $\nabla^2 f_0$ is the true Laplacian of f and $\nabla^2 f_i$ is the approximation of the Laplacian at particle i. The domain of integration is the region $2.25 < x < 2.75$, $2.25 < y < 2.75$. This subdomain was chosen so as to remove the effects of the boundary on the error calculation. Additionally, to check the convergence properties of these discretization when the particle spacing is not uniform, the same tests were run using the same particle arrays, but with particle positions given random perturbations of $-0.4s < \delta < 0.4s$ in both x and y. The results are shown in Figure 3.5.

The CSPM and CSPH2Γ forms show second-order convergence for regularly spaced arrays. Uncorrected forms of the Laplacian do not reliably improve with increasing resolution on these ordered arrays. This lack of convergence for uncorrected approximations was also observed by Belytschko et al. [2] in problems of linear elastostatics. Moreover, the addition of the perturbations to particle positions dramatically affects the convergence properties. The corrected forms (CSPM, CSPH2, and CSPH2Γ) no longer converge, but remain at a fairly constant relative error despite increasing resolution. Uncorrected forms can actually diverge with increasing resolution. Similar divergence behavior was observed by Quinlan et al. [106, 107] in one-dimensional tests of uncorrected approximations of functions and gradients with irregularly spaced particles. Although this divergence behavior is troubling, there is ample evidence of successful applications of SPH using the Brookshaw approximation on disordered particles. For the purposes of this study, it suffices to note that each correction term incrementally reduces the relative error of the Brookshaw approximation. As expected, the relative error of the CSPM approximation is less than all Brookshaw formulations as well as the SSPH approximation, but requires inverting larger matrices.

3.3 Boundary Conditions

When the fluid interacts with solid walls, boundary conditions are usually imposed through additional particles along the walls [66]. These are typically either a single layer of particles that defines that wall [82, 20], or a cloud of ghost particles that extend into the boundary [130, 112, 23], thereby ensuring that the interior fluid particles will have full kernel support. For the surface of a fluid, the stress-free boundary condition is usually not explicitly enforced (a notable exception is [120]) and a general method of imposing conditions on these surface boundaries is not well developed.

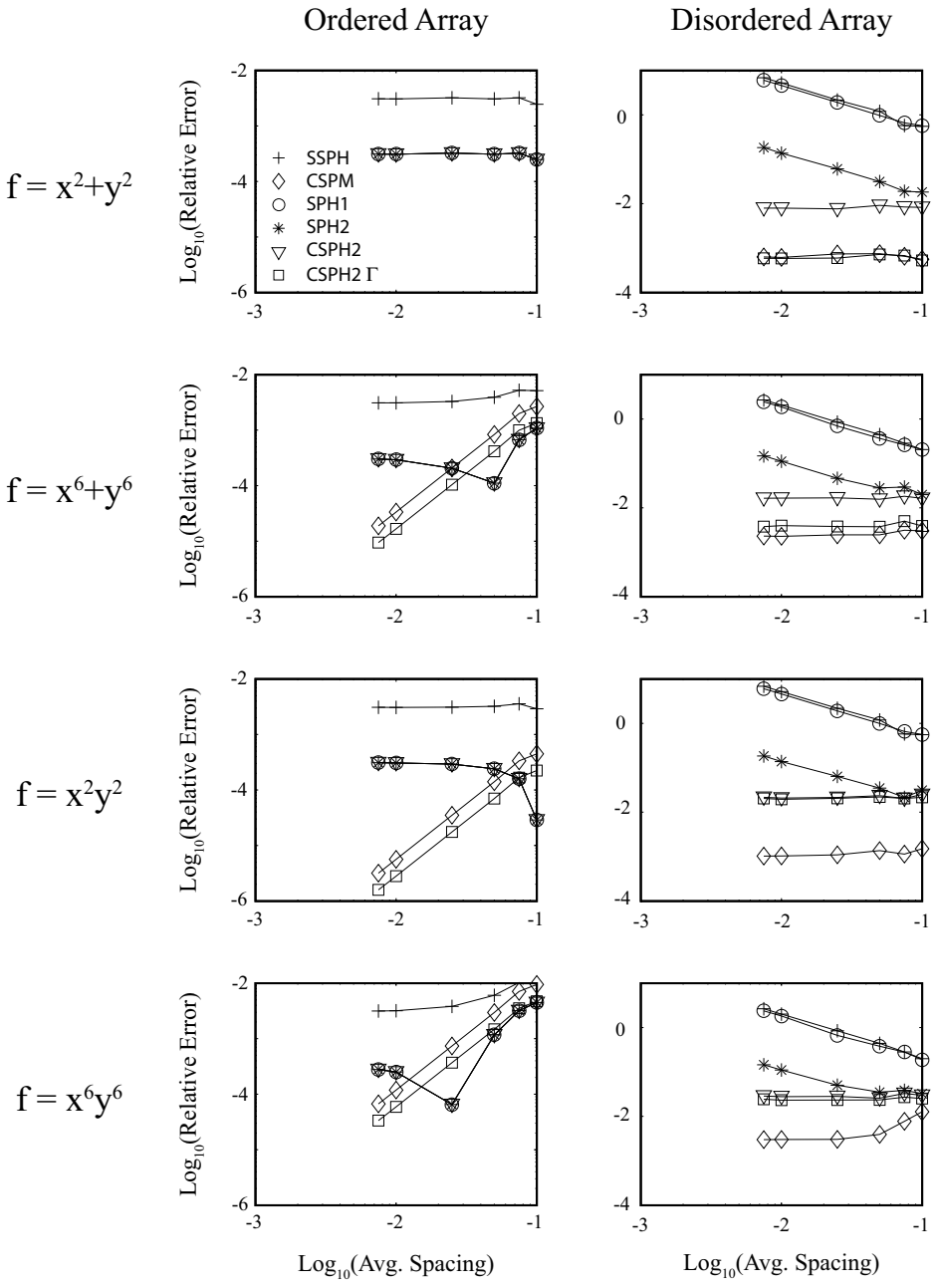

Figure 3.5: Relative errors of the various Laplacian discretization applied to four test functions for both regularly spaced and disordered arrays. All plots in the left column share the same scale, as do all plots in the right column. For $f = x^2 + y^2$ on a ordered array, the CSPM and CSPH2Γ forms are accurate to machine-ϵ and do not appear in the upper-left plot.

The method used in the steady-state and transient tests of section 3.4 for implementing boundary conditions on these two types of boundaries is described below.

3.3.1 Solid Wall Boundaries

Boundary conditions are enforced at solid-wall boundaries through ghost particles as shown in Figure 3.6. These ghost particles are positioned as described by Cummins and Rudman [23]. The ghost particles are generated by projecting the position of each of the interior particles across the boundary. Only interior particles within a kernel half-width of a boundary need to be considered. In this way, each ghost particle is linked with a source particle in the interior. This produces a layer of ghost particles with a thickness equal to the half-width of the kernel. Homogeneous Neumann conditions are enforced by assigning each ghost particle the value of its source particle which effectively creates a line of symmetry at the boundary. For homogeneous Dirichlet conditions, each ghost particle is assigned the negated value of its source particle in the interior. This forces an interpolated value of zero on the boundary. For inhomogeneous boundary conditions, each ghost particle is treated as an unknown, subject to the restriction that the ghost particle satisfies the boundary condition. For inhomogeneous Dirichlet conditions, the restriction is that the average value of the ghost particle and its source equals the required condition at the wall. This forces the linear interpolation of interior values to the correct boundary value. For inhomogeneous Neumann conditions, the restriction is that $\boldsymbol{\nabla} f_g \cdot \boldsymbol{n}$ equals the imposed value, where $\boldsymbol{n}$ is the unit normal to the boundary and $\boldsymbol{\nabla} f_g$ is calculated using Eq. 3.22. Since each of the ghost particles will have less than full kernel support (large circle in Figure 3.6a), the use of the corrected gradient is critical and improves convergence of the iterative solver.

Ghost particles in the wedge-shaped region shown in Figure 3.6b are positioned by projecting the interior particles through the point joining the two boundary walls. The boundary conditions that are enforced for these particles depends on the position within the wedge. If the boundary conditions on the walls B_1 and B_2 are of the same type (i.e. both Dirichlet), then the condition enforced at the ghost particle is interpolated and given by

$$B_g = \frac{\beta}{\gamma} B_1 + \frac{\alpha}{\gamma} B_2 \tag{3.29}$$

If walls B_1 and B_2 are of different types, the ghost particle is assigned the conditions of the closer wall.

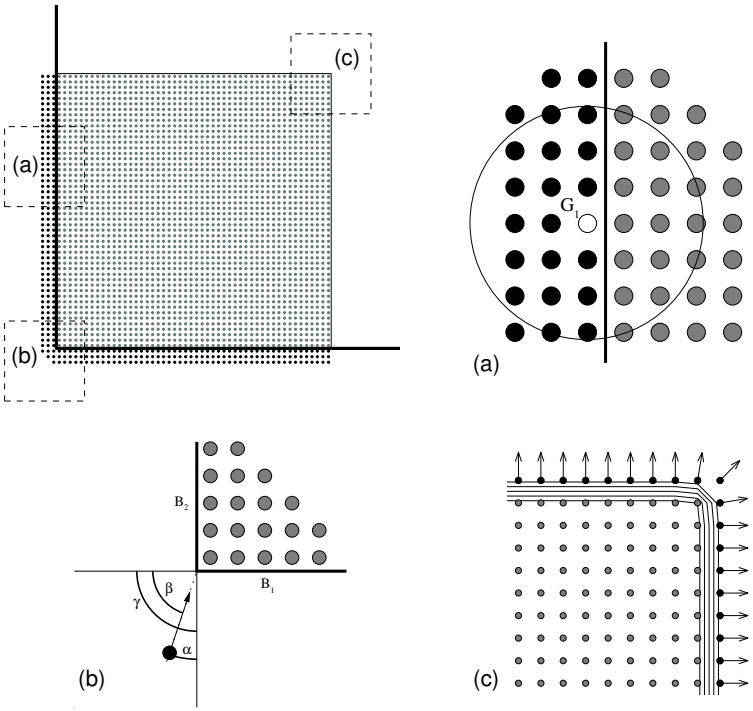

Figure 3.6: Treatment of boundaries: Ghost particles (black) are positioned by projecting interior particles across the boundary. Gradient boundary conditions determine the value at the ghost particles by requiring that the gradient at each ghost particle satisfy the boundary condition (inset (a)). Conditions at ghost particles near corners (inset (b)) are interpolated between adjacent walls. Inset (c) shows contours of kernel volume near surfaces and the surface normal.

3.3.2 Surface Boundaries

Particles with a kernel volume ($\mathcal{V} = \sum_j \varphi_j W$) less than a given threshold are identified as surface boundary particles. The value of the threshold that ensures a boundary one-particle thick depends on the kernel used and the initial geometry. For a quintic spline kernel and a rectangular initial geometry, a threshold value of 0.79 will result in a thin surface boundary layer. This method of identifying surfaces is the same as used by Shao and Lo [120], but with a lower threshold.

To apply gradient boundary conditions on the surface, a surface normal needs to be defined. The normalized gradient of the kernel support volume ($\boldsymbol{\nabla}\mathcal{V}$) is a suitable vector for this purpose, although there is some deviation from the true normal in the vicinity of corners as can be seen in Figure 3.6c.

With this formulation, surface particles are treated as ghost particles in that they are only required to satisfy the boundary conditions, not the differential equation. In order to ensure that the boundary condition is imposed at the correct location, it is advantageous to use a low kernel volume threshold in order to identify a thin surface boundary. Note that with this formulation, the calculation of the Laplacian at the edge of the domain is avoided in exchange for calculating a gradient value. An alternative method, in an approach parallel to that suggested by Chen et al. [18], would be to calculate the Laplacian at the surface particle via Eq. 3.23 and directly insert gradient boundary conditions into the correction term rather than calculate $f_{,\alpha}$ via Eq. 3.22.

A point to note with this formulation of gradient boundary conditions, is that since only the component of the gradient normal to the boundary is constrained, this formulation allows arbitrary gradients to develop tangent to the boundary. These spurious modes did not arise, however, in the test cases of steady-state and transient conduction using Eq. 5.2.

3.4 Numerical Tests

To test the proposed Laplacian discretization (Eq. 5.2) with the implementation of boundary conditions as described in section 3.3, numerical results of steady-state and transient thermal diffusion in a square plate is compared with analytical solutions. The governing equation is

$$\frac{\partial T}{\partial t} = \frac{1}{\rho c_p}\,\boldsymbol{\nabla}\cdot\Big(k\boldsymbol{\nabla}T\Big) + r \tag{3.30}$$

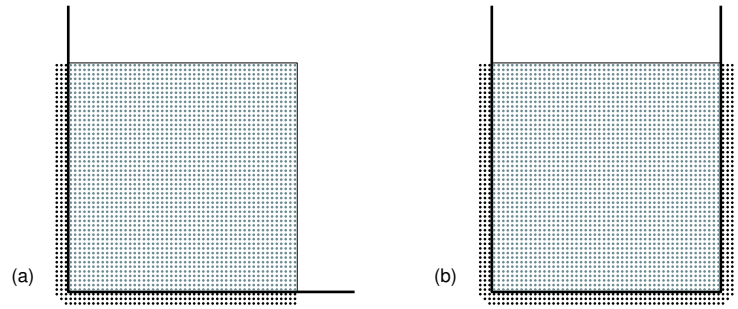

Figure 3.7: For the steady-state thermal problems of section 3.4.1, particles are positioned as shown in (a). For the transient problem of section 3.4.2, particles are positioned as shown in (b).

where T is the temperature, t is time, c_p is the specific heat, k is the thermal conductivity, and r is a heat source or sink. The general form of mixed boundary conditions is given by

$$\alpha T + (1-\alpha)\frac{\partial T}{\partial n} = \mathcal{B} \tag{3.31}$$

$\alpha = 1$ corresponds to Dirichlet conditions, $\alpha = 0$ corresponds to Neumann conditions and $\mathcal{B}$ is the inhomogeneous term.

All simulations are solved on a unit square with the same geometry as for the patch tests (non-rotated), but with solid-wall and surface boundaries as shown in Figure 3.7.

3.4.1 Steady-state thermal diffusion

Two steady-state cases were run (Figures 3.8 and 3.11). The first case tests the implementation of Dirichlet conditions at walls and surfaces. The second case tests Neumann conditions. In each case, a Poisson equation was solved, written in matrix form as

$$\begin{bmatrix} \mathbf{A} \\ \mathbf{B} \end{bmatrix} \begin{bmatrix} T_i \\ T_g \end{bmatrix} = \begin{bmatrix} r \\ \mathcal{B} \end{bmatrix} \tag{3.32}$$

where T_i and T_g are the unknown temperature values at the interior and ghost particles, and

$$\mathbf{A} = \Big[\frac{1}{\rho c_p}\,\boldsymbol{\nabla}\cdot\Big(k\boldsymbol{\nabla}\Big)\Big]$$

$$\mathbf{B} = \alpha + (1-\alpha)\hat{\boldsymbol{n}}\cdot\boldsymbol{\nabla}$$

r is included for generality, although the following test cases contained no heat sources or sinks. Also for generality, the inhomogeneous form of the Laplacian (Eq. 5.2) was used though the material properties were homogeneous. Eq. 3.32 is a large, sparse linear system which can be solved using standard matrix solving routines. Since the matrix in Eq. 3.32 is not symmetric, the GMRES solver from SPARSKIT [114] was used.

Inhomogeneous Dirichlet test case

For the general case of inhomogeneous Dirichlet conditions on a rectangle of width a and height b, the steady-state solution can be expressed using Fourier series:

$$\begin{aligned} T(x,y) &= \sum_{n=\text{odd}} \left[\frac{4f_1}{n\pi \sinh\left(\frac{n\pi b}{a}\right)} \right] \sin\left(\frac{n\pi}{a}x\right) \sinh\left(\frac{n\pi}{a}(b-y)\right) \\ &+ \sum_{n=\text{odd}} \left[\frac{4f_2}{n\pi \sinh\left(\frac{n\pi a}{b}\right)} \right] \sin\left(\frac{n\pi}{b}y\right) \sinh\left(\frac{n\pi}{b}x\right) \\ &+ \sum_{n=\text{odd}} \left[\frac{4f_3}{n\pi \sinh\left(\frac{n\pi b}{a}\right)} \right] \sin\left(\frac{n\pi}{a}x\right) \sinh\left(\frac{n\pi}{a}y\right) \\ &+ \sum_{n=\text{odd}} \left[\frac{4f_4}{n\pi \sinh\left(\frac{n\pi a}{b}\right)} \right] \sin\left(\frac{n\pi}{b}y\right) \sinh\left(\frac{n\pi}{b}(a-x)\right) \end{aligned} \tag{3.33}$$

where f_1 is the boundary condition at $y = 0$, f_2 at $x = a$, f_3 at $y = b$, and f_4 at $x = 0$. In the present case, $a = b = 1 - s/2$ where $s =$ the initial particle spacing and $f_{1...4}$ is given in the upper-left plot of Figure 3.8. Since the material properties are assumed to be homogeneous, they do not affect the steady-state solution and do not appear in Eq. 3.33. Contours of the series solution and numerical solution (using Eq. 5.2) are shown in Figure 3.8 along with several representative transects.

Figure 3.9 compares the convergence rates of the various discretizations and Figure 3.10 shows the relative error of the converged solutions. The convergence criterion used was ||residual|| <= $10^{-5} * ||\text{RHS}|| + 10^{-8}$, where RHS is the right-hand-side of Eq. 3.32. The four forms based on the Brookshaw approximation of the Laplacian all converged at a similar rate and also produced converged solutions with similar errors. The two forms based on second-order derivatives of the kernel (CSPM and SSPH forms) also shared convergence properties as well as similar errors in the vicinity of the surface.

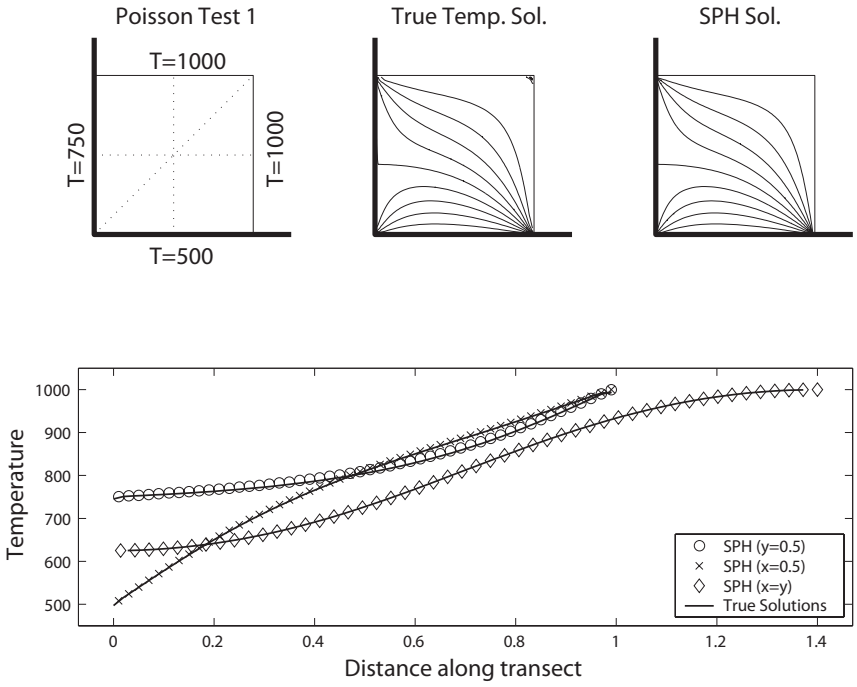

Figure 3.8: Test of inhomogeneous Dirichlet boundary conditions on solid wall boundaries and surfaces using the CSPH2Γ approximation. The transects shown in the lower plot are illustrated in the upper-left plot.

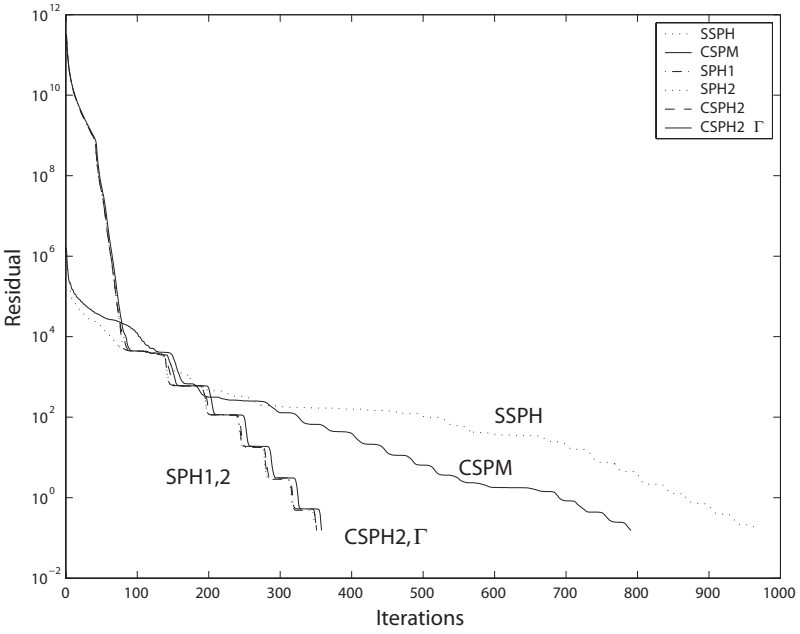

Figure 3.9: A comparison of the convergence rates of the different discretizations for the Dirichlet case described in Figure 3.8.

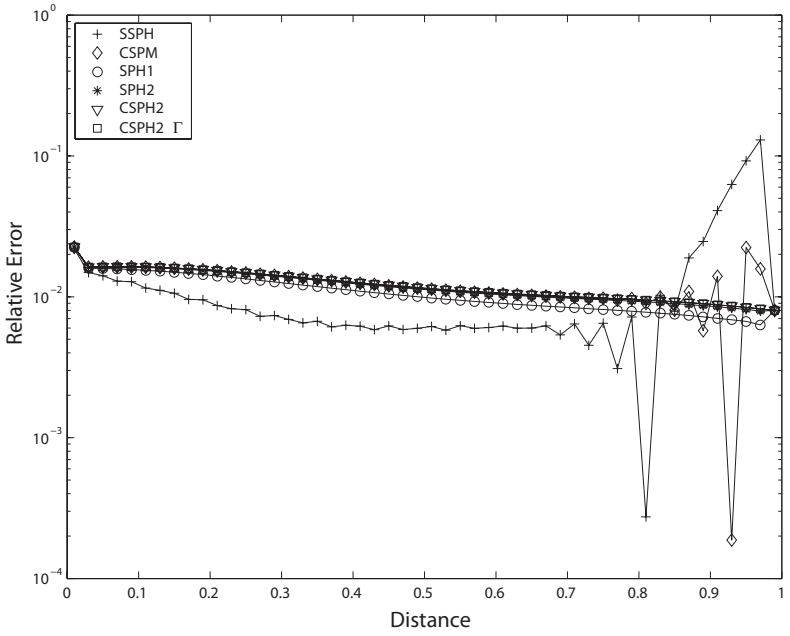

Figure 3.10: A comparison of the relative error of the converged solution along the line $x = 0.5$ for the different discretizations for the Dirichlet case.

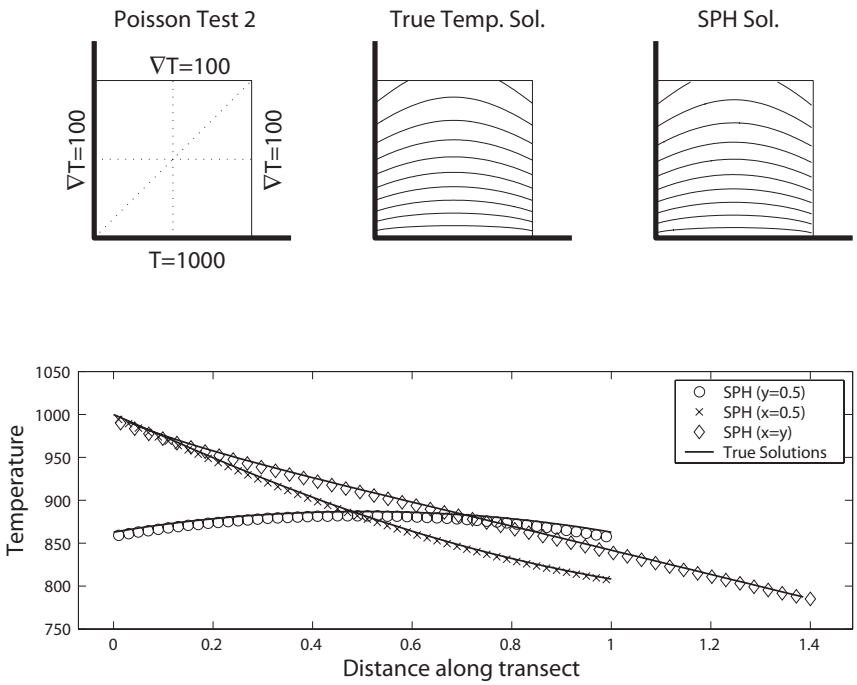

Figure 3.11: Test of inhomogeneous Neumann boundary conditions on solid wall boundaries and surfaces using the CSPH2Γ approximation. The transects shown in the lower plot are illustrated in the upper-left plot.

Inhomogeneous Neumann

The general steady-state solution for a Dirichlet condition along the base of the plate and Neumann conditions elsewhere is given by

$$T(x,y) = f_1 + f_3 y + \sum_{n=1}^{\infty} \frac{2f_2 \cosh\left(\sqrt{\lambda_n}x\right) - 2f_4 \cosh\left(\sqrt{\lambda_n}(a-x)\right)}{b\lambda_n \sinh\left(\sqrt{\lambda_n}a\right)} \sin\left(\sqrt{\lambda_n}y\right), \quad \lambda_n = \frac{(2n-1)\pi}{2b}$$

In the present case, $a = b = 1 - s/2$ and $f_{1\ldots4}$ is given in the upper-left plot of Figure 3.11. Results of the numerical solution are compared with the series solution in Figure 3.11.

Figure 3.12 compares the convergence rates of the various discretizations and Figure 3.13 shows the relative error of the converged solutions. The convergence criterion used was ||residual|| <= $10^{-5} * ||\text{RHS}|| + 10^{-8}$, where RHS is the right-hand-side of Eq. 3.32. For each discretization, enforcing a Neumann boundary condition reduces the convergence rate significantly compared to the Dirichlet case. As in the Dirichlet case, the four formulations based on the Brookshaw approximation of the Laplacian converge initially at a similar rate, although the lack of the corrected form of the gradient

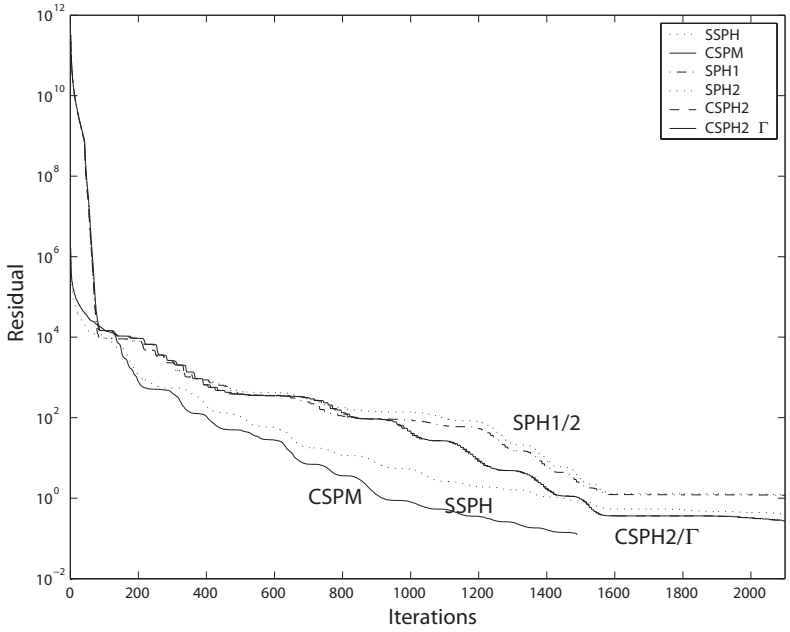

Figure 3.12: A comparison of the convergence rates for the different discretizations for the Neumann case.

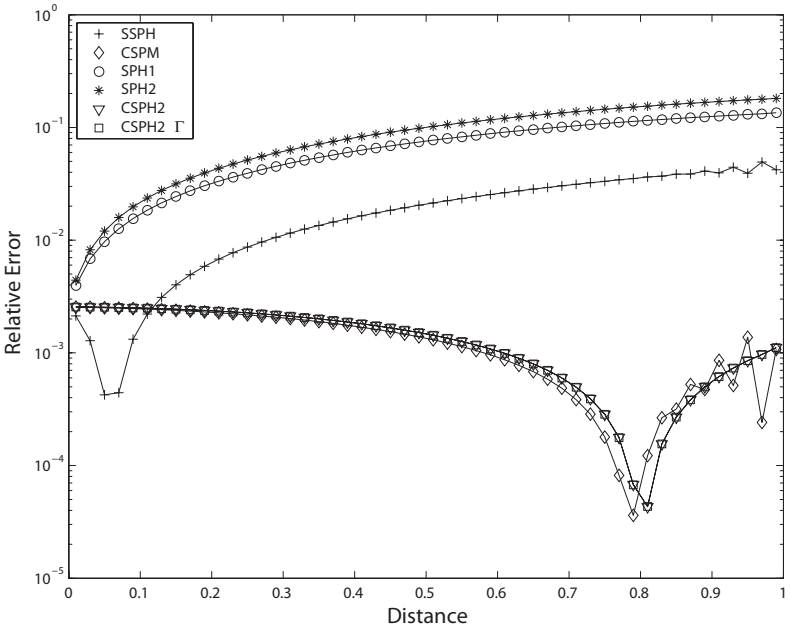

Figure 3.13: A comparison of the relative error of the converged solution along the line $x = 0.5$ for the different discretizations for the Neumann case.

in the SPH1 and SPH2 forms slows convergence and ultimately leads to the failure of the SPH1 form in returning an accurate solution (Figure 3.13). The CSPH2 and CSPH2Γ both continue to converge at a slow rate, yet returned a smooth solution. The SSPH and CSPM methods converge slightly faster than the Brookshaw forms, however the SSPH solution produces inaccurate results. The CSPM solution does not contain oscillatory behavior as strong as in the Dirichlet case.

Particle Disorder

Throughout this study, the quintic spline kernel was used. This kernel has a slightly wider support region than the commonly-used cubic spline kernel and therefore involves a greater number of interacting pairs, increasing both the computational and storage burden. The primary motivation for using this higher-order kernel is that smoother kernels mitigate the sensitivity of Laplacian calculations on particle disorder [9]. To determine the sensitivity of this formulation to particle disorder, the Neumann test case described above was run on two arrays, the regular array shown in Figure 3.7 and one with particle positions given random perturbations of $-0.4s < \delta < 0.4s$ in both x and y. Tests were conducted for both Eq. 5.2 and the CSPM method (Eq. 3.13 [18]) using both the quintic spline kernel (Figure 3.14) and the cubic spline kernel (Figure 3.15).

In all cases, the addition of particle disorder slows the convergence of the iterative solver. In fact, with the convergence criterion used above, the iterative solver used as many iterations as was allowed for all disorder cases. The maximum number of iterations was restricted to 75% of the number of unknowns. The relative error from the CSPM method is greater using the disordered array. Surprisingly, this increase is more pronounced when using the quintic spline kernel.

The convergence rate for the CSPH2Γ form (Eq 5.2) is initially unaffected by the particle disorder, although, the rate decreases after several hundred iterations. The relative error is slightly affected by both the particle disorder or the use of a lower-order kernel.

3.4.2 Transient Diffusion (Cooling of an infinite slab)

To test the ability of the proposed discretization and implementation of boundary conditions in representing transient behavior, the cooling of an infinite slab of thickness b from an initial temperature of $T = 750°$ to steady-state was modeled. The domain used consists of the same domain as in previous test, but with boundaries as shown in Figure 3.7(b) with a fixed temperature at the base and adiabatic ($\partial T/\partial n = 0$) side-walls. The equations are integrated in time using the Backward

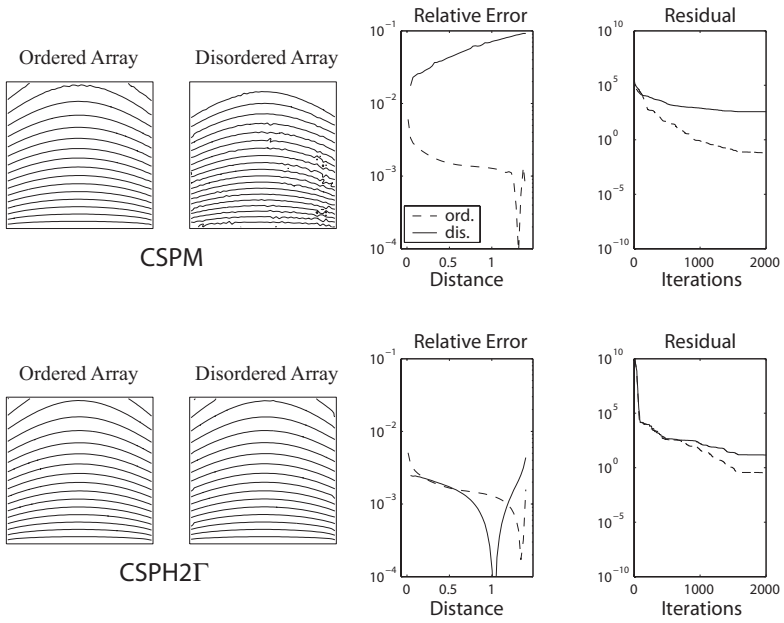

Figure 3.14: Effects of particle disorder on the steady-state Neumann test case with a quintic spline kernel. Results from the CSPM method are shown in the top row, CSPH2Γ on the bottom. Contour plots (contour interval = 12.5°) are for a ordered array on the left and disordered array on the right. Boundary conditions are shown in Figure 3.11.

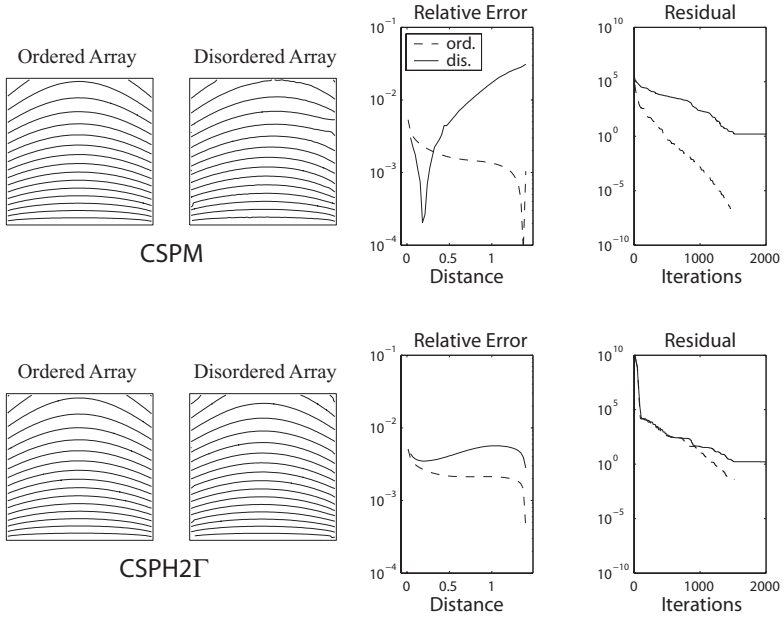

Figure 3.15: Effects of particle disorder on the steady-state Neumann test case with a cubic spline kernel. Boundary conditions are shown in Figure 3.11.

Euler method resulting in the following linear system:

$$\begin{bmatrix} \mathbf{A} \\ \mathbf{B} \end{bmatrix} \begin{bmatrix} T_i \\ T_g \end{bmatrix}^{(n+1)} = \begin{bmatrix} T_i + (\Delta t) r \\ \mathcal{B} \end{bmatrix}^{(n)} \tag{3.34}$$

where

$$\mathbf{A} = \mathbf{1} - \Delta t \Big[\frac{1}{\rho c_p} \boldsymbol{\nabla} \cdot \Big(k \boldsymbol{\nabla} \Big) \Big]$$

$$\mathbf{B} = \alpha + (1 - \alpha) \hat{\boldsymbol{n}} \cdot \boldsymbol{\nabla}$$

Tests were run for the three types of linear boundary conditions at the surface: Dirichlet, Neumann, and mixed. In each of these cases, homogeneous material properties ($\rho = 10^3$ kg/m^3, $c_p = 10^3$ J/(kg K), and $k = 10^5$ J/(s m K)) were used with no heat sources or sinks. The general solution for all three cases is given by

$$u_t = \kappa u_{yy} \quad u(0,t) = u_1 \quad u(y,0) = u_0$$

$$u(y,t) = u_{ss}(y) + \sum_{n=1}^{\infty} B_n e^{-t \lambda_n \sqrt{\kappa}} \sin\left(\sqrt{\lambda_n} y \right) \tag{3.35}$$

where $\kappa = \frac{k}{\rho c_p} = 10^{-1}$ m^2/s, $u_1 = 1000°$, $u_0 = 750°$, and u_{ss} is the steady-state solution. The particular values for the surface boundary condition were chosen so that the u_{ss} was the same (a linear temperature profile from 1000° to 500°), although the rate of cooling depends on λ_n which differs among the cases.

Dirichlet For the case of a fixed surface temperature, the boundary condition, eigenvalues and coefficients are given by

$$u(b,t) = u_2 = 500° \qquad u_{ss}(y) = u_1 - \frac{u_1 - u_2}{b} y$$

$$\lambda_n = \Big(\frac{n\pi}{b} \Big)^2 \qquad B_n = \frac{2}{b\sqrt{\lambda_n}} \Big(\big(u_2 - u_0 \big) \big(-1 \big)^n + u_0 - u_1 \Big)$$

Neumann For the case of a fixed surface heat flux, the boundary condition, eigenvalues and coefficients are given by

$$u_y(b,t) = f_2 = -500°/m \qquad u_{ss}(y) = u_1 + f_2 y$$

$$\lambda_n = \left(\frac{(2n-1)\pi}{2b} \right)^2 \qquad B_n = \frac{2}{b\sqrt{\lambda_n}} \Big(u_0 - u_1 - \frac{f_2}{\sqrt{\lambda_n}} \big(-1 \big)^{n-1} \Big)$$

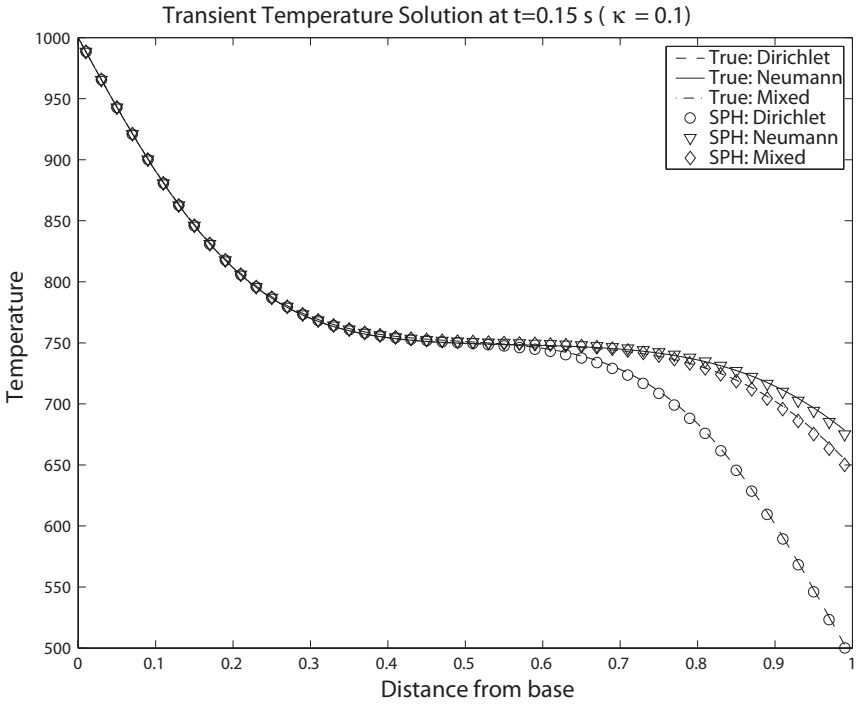

Figure 3.16: Test of the three types of linear boundary conditions the surface at $t = 0.15$ s. The base ($x = 0$) is held at $T = 1000°$ and the initial temperature is 750°.

Mixed For the case of heat flux governed by Newton's Law of cooling, the boundary condition is mixed with $\alpha = 1/2$. The boundary condition, eigenvalues and coefficients are given by

$$u(b,t) + u_y(b,t) = 0 \qquad u_{ss}(y) = u_1 - \frac{u_1}{b+1}y$$

$$\lambda_n = -\tan(\lambda_n b) \simeq \frac{(2n-1)\pi}{2b} \qquad k_n = \sqrt{\frac{2}{b + \cos^2(b\sqrt{\lambda_n})}}$$

$$B_n = k_n^2 \left[\Big(\frac{u_1 - u_0}{\sqrt{\lambda_n}} \Big) \Big(\cos(b\sqrt{\lambda_n}) - 1 \Big) + \Big(\frac{2u_1}{b+1} \Big) \frac{\sin(b\sqrt{\lambda_n})}{\sqrt{\lambda_n}} \right]$$

where k_n is a normalizing factor for the eigenfunction $\sin(\sqrt{\lambda_n}y)$. In all cases, a time-step of $\Delta t = 10^{-3}$ s was used and a stopping criterion for the iterative solver of $||\text{residual}|| <= 10^{-8}||\text{RHS}|| + 10^{-11}$ where RHS refers to the right-hand-side of Eq. 3.34. The numerical results are compared with the above series solutions for each of the three boundary conditions at a $t = 0.15$ s in Figure 3.16.

3.5 Concluding Remarks

Several methods have been proposed to address the difficulties involved in calculating second-order derivatives with SPH [5, 9, 15, 18, 20, 147, 67]. In contrast with the present formulation, many of these methods achieve a high accuracy through fully calculating the Hessian [18, 147, 67] or requiring that the discrete equations exactly reproduce quadratic functions [5]. The primary attraction of the present method is that it provides a simple correction term to a Laplacian discretization commonly used for thermal, viscous, and pressure projection problems which can be incrementally improved. If the computational and programming overhead of calculating corrected gradients is avoided, this correction term is a trivial addition and improves the accuracy near boundaries in each of the test cases. Including gradient corrections further improves the Laplacian approximation near boundaries, although this requires an n-by-n matrix inversion for each particle and significant additional storage. Finally, a scaling term can be used which reduced the relative errors in approximating the Laplacian for most of the test functions on a square patch although it did not lead to significant reduction in relative error for the steady-state thermal test cases. Additionally, this scaling term appears to be sensitive to the particle distribution and requires an additional n-by-n matrix inversion. The discretization was tested for transient heat conduction using a variety of surface boundary conditions. Convergence rates are slower with particle disorder, however the CSPH2Γ solution remains robust. It is possible that these rates may be improved with preconditioning or alternate implementations of boundary conditions [18] [136]. Although the converged solution of Eq. 5.2 with gradient boundary conditions does not appear to be influenced by spurious boundary modes, further work is needed to ensure that this boundary implementation can be used with other Laplacian discretizations.

The primary application for this improved thermal problem as presented will be in modeling the deformation of strongly coupled thermo-mechanical fluids such as the advancing lobe of cooling lava.

Within the context of visco-plastic modeling of geomaterials, the developments of this chapter will be applied to more accurate calculations of $\nabla^2 p$. Much more discussion can be found in chapter 5, however, the central idea is that for frictional (pressure dependent) material, an accurate and smooth pressure solution is crucial for the non-linear solution to converge. An uncorrected Laplacian can result in too much noise in the pressure solution, particularly for disordered particles, which can corrupt the convergence of the non-linear solver. Essentially, a smooth velocity field with an oscillatory pressure field will result in a distribution of plastic failure that mimics the oscillatory pressure field. The corrected Laplacian term greatly mitigates this effect.

Chapter 4

A GENERALIZED QUASI-COMPRESSIBILITY SPH MODEL FOR INCOMPRESSIBLE VISCOUS FREE-SURFACE FLOW

We present a Smoothed Particle Hydrodynamics (SPH) formulation of incompressible viscous free-surface flow. This formulation is a generalization of the quasi-compressibility methods (artificial compressibility, penalty, pressure stabilization, pressure correction) in which pressure is evolved through a perturbed continuity equation. The performance of both explicit and implicit formulations is compared with the standard explicit formulation based on an equation of state. SPH numerical results of several test cases are compared with analytical solutions and results from other numerical methods.

4.1 Introduction

The Smoothed Particle Hydrodynamics (SPH) method (see [84] for a review.) was developed to model compressible fluid dynamics in self-gravitating, astrophysical flows. The method uses a mesh-free spatial discretization and solves the fluid equations on interpolation points that are advected with the fluid. SPH was first applied to incompressible fluid flow by explicitly evolving the momentum and continuity equations using a stiff equation of state [82]. This method allows a slight compressibility governed by the sound speed and is commonly used in free-surface flow modeling. Morris et al. [89] extended SPH to low Reynold's number flow by including a term in the momentum equation for the physical viscosity. As an alternate method of enforcing the incompressibility condition, Cummins and Rudman [23] presented a projection method for SPH. This method involves first integrating the velocity field, then projecting this field onto the space of divergence-free vectors to enforce the incompressibility constraint. Larger time steps can be used since there are no restrictions from a sound speed, but this method requires solving a Poisson equation for pressure. Variations of this method have appeared recently ([99, 120, 115]) each using a slightly different Poisson equation. A similar approach was used by Colin et al. [22] who also used a fractional step approach, but solved for the null divergence velocity field via a Helmholtz–Hodge decomposition. A novel approach to enforcing incompressibility was presented by Ellero et al. [30] in which they require that the volume of particles remain constant.

As an alternative to the pressure projection method and formulations based on coupling pressure to an evolving density through an equation of state, we investigate an SPH discretization of a mixed formulation where both velocity and pressure are determined such that the velocity field remains approximately solenoidal ($\nabla \cdot \boldsymbol{v} = 0$).

In general, the incompressibility condition imposes a global constraint on the divergence of the velocity that results in an elliptic system of equations which is numerically expensive to solve. Several numerical methods are widely used that address this constraint by coupling the pressure and velocity fields through a perturbed continuity equation. The penalty method [51], for example, relaxes the strict enforcement of the divergence-free condition by directly coupling pressure to velocity divergence. Similarly, the artificial compressibility method [19] relaxes the incompressibility constraint by linking a divergence of the velocity to a pressure evolution equation. Other perturbations based on higher-order derivatives of the pressure have also been used such as the pressure stabilization [60] and pressure correction [123] methods. Hybrid forms of these perturbations have been employed with modest success with both explicit [109] and implicit [78] solvers although Dukowicz [28] noted that projection methods can be more efficient if the pressure Poisson equation is solved with a symmetric solver.

These standard perturbation methods of enforcing a solenoidal vector field have also been employed in enforcing the $\nabla \cdot \boldsymbol{B} = 0$ constraint in magnetohydrodynamics (MHD) [90, 132]. Recently, an analogous hybrid form has been used to impose this constraint in both grid-based [26] and SPH implementations [102] through the use of 'generalized Lagrange multiplier' coupling the equations. In the MHD literature, these methods are referred to as 'divergence cleaning' since a non-zero $\nabla \cdot \boldsymbol{B}$ only arises from numerical errors; there is no mechanism in the MHD equations to generate a divergence of the magnetic field. This is in contrast with the incompressible Navier-Stokes (N-S) equations in which the only mechanism to prevent compression is the presence of the Lagrange multiplier in the form of pressure [131]. Nevertheless, these techniques behave as a mechanism for 'divergence cleaning' of the velocity field.

In this paper, we first outline these methods as they apply to the incompressible transient Navier-Stokes equations, then discuss the SPH implementation showing the results of patch-test numerical experiments. Finally, we show the method applied to three test cases: shear flow down an inclined plane, lid-driven flow in a square cavity, and the collapse of a viscous droplet.

4.2 Existing SPH Formulations of Incompressible Flow

The governing equations for mass and momentum conservation for an incompressible, viscous fluid are given by

$$\frac{\mathrm{D}v}{\mathrm{D}t} = -\frac{1}{\rho}\boldsymbol{\nabla}p + \frac{1}{\rho}\,\boldsymbol{\nabla}\cdot\left(\mu\boldsymbol{\nabla}\boldsymbol{v}\right) + \boldsymbol{g} \qquad \text{momentum} \tag{4.1}$$

$$\boldsymbol{\nabla}\cdot\boldsymbol{v} = 0 \qquad \text{continuity} \tag{4.2}$$

where $\boldsymbol{v}$, p, and $\boldsymbol{g}$ are the velocity, pressure, and body acceleration; μ and ρ are the dynamic viscosity and density; and $\frac{\mathrm{D}}{\mathrm{D}t} = \frac{\partial}{\partial t} + \boldsymbol{v}\cdot\boldsymbol{\nabla}$ is the material time derivative.

4.2.1 Weakly compressible SPH

The standard SPH formulation for incompressible free-surface flow is outlined in [82] and involves solving the compressible form of the continuity equation but with an equation of state that only allows for minor density fluctuations.

$$\frac{1}{\rho}\frac{\mathrm{D}\rho}{\mathrm{D}t} = -\boldsymbol{\nabla}\cdot\boldsymbol{v} \tag{4.3}$$

$$p = D\left[\left(\frac{\rho}{\rho_0}\right)^{\gamma} - 1\right] \tag{4.4}$$

where $D = c_s^2\rho$ and c_s is the speed of sound. This formulation is sometimes referred to as 'weakly compressible' [23] since c_s can be chosen much lower than the true speed of sound, thereby accepting greater perturbations in density and velocity divergence than are physical. Accepting this error allows for larger time steps to be used and leads to a more efficient, albeit less accurate, calculation. Monaghan [82] noted that with this formulation, density perturbations will be approximately 1% if c_s is chosen to be approximately 10 times the typical flow velocity of the problem. In a sense, Eq. 4.3 can be thought of as a perturbed form of Eq. 4.2 where the perturbation is $-\frac{1}{\rho}\frac{\mathrm{D}\rho}{\mathrm{D}t}$.

4.2.2 Pressure Projection

Projection methods are commonly used for incompressible flow calculation and are particularly successful for flow at moderate Reynolds number (Re) [138]. These methods involve two steps for each time increment. First the momentum equation is integrated to an intermediate velocity while neglecting the pressure gradient term. The second step uses the divergence of the intermediate velocity to determine the pressure necessary to maintain incompressibility. This involves solving a Poisson equation for pressure for which there are fast solvers, particularly for grid-based methods.

Cummins and Rudman [23] implemented an SPH formulation of a projection method which resulted in a symmetric system of equations and could therefore take advantage of fast symmetric solvers.

The advantage of this scheme, particularly for moderate Re flows, is that time steps are not constrained by the CFL condition, whereas a large c_s would need to be chosen in the WCSPH formulation to approximate incompressibility. For viscous flow, the associated time step restriction from viscous diffusion would still need to be observed in calculating the intermediate velocity.

4.2.3 Constant volume formulation

An alternative approach to enforcing incompressibility, proposed by Ellero et al. [30], is to focus on constraining the evolution of a volume element of the fluid. This kinematic constraint is imposed through Lagrange multipliers which behave as a non-thermodynamic pressure.

4.3 Quasi-Compressibility Formulations

The quasi-compressibility methods (also called pseudo-compressibility methods [123]) of approximating incompressible Stokes flow result from relaxing the strictly divergence-free velocity condition by a perturbation as follows.

$$\frac{\partial \boldsymbol{v}}{\partial t} = \frac{1}{\rho}\boldsymbol{\nabla}\cdot\left(\mu\boldsymbol{\nabla}\boldsymbol{v}\right) + \boldsymbol{g} - \frac{1}{\rho}\boldsymbol{\nabla}p \tag{4.5}$$

$$\mathcal{D}(p) = -\boldsymbol{\nabla}\cdot\boldsymbol{v} \tag{4.6}$$

where $\mathcal{D}$ is a linear operator applied to pressure. Note that we are only considering a perturbation to the Stokes equations and are neglecting the non-linear term of the N-S equations (i.e. $\partial/\partial t \simeq \mathrm{D}/\mathrm{D}t$). This generalized perturbation is analogous to a coupling of the solenoidal magnetic field constraint to the MHD equations through 'generalized Lagrange multipliers' as proposed by Dedner et al. [26]. Eq.'s 4.5 and 4.6 are in the form analogous to Eq.'s 4 and 5 of Dedner et al. [26]. In applying his analysis to the Stokes equations (with homogeneous material properties), we first take the divergence of Eq. 4.5 which leads to

$$\frac{\partial}{\partial t}\left(\boldsymbol{\nabla}\cdot\boldsymbol{v}\right) = -\frac{1}{\rho}\boldsymbol{\nabla}^2 p \tag{4.7}$$

Then taking the time derivative of Eq. 4.6 leads to

$$\frac{\partial}{\partial t}\mathcal{D}(p) + \frac{\partial}{\partial t}(\boldsymbol{\nabla}\cdot\boldsymbol{v}) = 0 \tag{4.8}$$

which, combined with Eq. 4.7 gives

$$\frac{\partial}{\partial t}\mathcal{D}(p) - \frac{1}{\rho}\boldsymbol{\nabla}^2 p = 0 \tag{4.9}$$

Applying the $\mathcal{D}$ operator to Eq. 4.7 results in

$$\mathcal{D}\Big(\frac{\partial}{\partial t}(\boldsymbol{\nabla}\cdot\boldsymbol{v})\Big) = -\frac{1}{\rho}\mathcal{D}\Big(\boldsymbol{\nabla}^2 p\Big) \tag{4.10}$$

and applying the Laplacian to Eq. 4.6 leads to (assuming $\mathcal{D}$ and $\boldsymbol{\nabla}^2$ commute)

$$\mathcal{D}\Big(\boldsymbol{\nabla}^2 p\Big) + \boldsymbol{\nabla}^2\Big(\boldsymbol{\nabla}\cdot\boldsymbol{v}\Big) = 0 \tag{4.11}$$

which together (assuming $\frac{\partial}{\partial t}$ and $\mathcal{D}$ commute) result in

$$\frac{\partial}{\partial t}\Big(\mathcal{D}(\boldsymbol{\nabla}\cdot\boldsymbol{v})\Big) - \frac{1}{\rho}\boldsymbol{\nabla}^2\Big(\boldsymbol{\nabla}\cdot\boldsymbol{v}\Big) = 0 \tag{4.12}$$

When comparing Eq. 4.12 with Eq. 4.9, we see that in homogeneous media both p and $\boldsymbol{\nabla}\cdot\boldsymbol{v}$ follow the same evolution equation, regardless of the form of $\mathcal{D}$. This is useful since we can then use Eq. 4.9 to determine the behavior of p as a proxy for how velocity divergence is evolved.

The equation we are primarily interested in solving, however, is the momentum equation with inhomogeneous material properties (Eq. 4.1). This modifies Eq. 4.9 to

$$\frac{\partial}{\partial t}\mathcal{D}(p) - \frac{1}{\rho}\boldsymbol{\nabla}^2 p = -\Gamma \tag{4.13}$$

where Γ is a parameter that depends on the spatial gradients of the material properties as follows.

$$\Gamma = \frac{1}{\rho}\left[\boldsymbol{\nabla}\cdot\Big[\boldsymbol{\nabla}\cdot\Big(\mu\boldsymbol{\nabla}\boldsymbol{v}\Big)\Big] + \boldsymbol{\nabla}\rho\cdot\Big(\boldsymbol{g} - \frac{\partial\boldsymbol{v}}{\partial t}\Big)\right]$$

If $\mathcal{D}$ is set identically to zero, Eq. 4.13 reduces to the Poisson equation

$$\boldsymbol{\nabla}^2 p = \rho\Gamma \tag{4.14}$$

which has the numerically difficult elliptic character. Eq. 4.6 then reduces to $\boldsymbol{\nabla}\cdot\boldsymbol{v} = 0$ and the incompressibility constraint is strictly enforced.

4.3.1 Artificial Compressibility $\mathcal{D}(p) = \epsilon_1 \frac{\partial p}{\partial t}$

The artificial compressibility method [19] is a commonly used perturbation in which the form of $\mathcal{D}$ is the time derivative of p. This transforms Eq. 4.13 to a wave equation

$$\frac{\partial^2 p}{\partial t^2} - \frac{1}{\epsilon_1 \rho}\left(\boldsymbol{\nabla}^2 p - \rho\Gamma\right) = 0 \tag{4.15}$$

which can easily be solved with explicit solvers since the time step restriction is $\Delta t \leq \epsilon_1 \Delta x$. In this case, p is evolved via Eq. 4.6 following $\frac{\partial p}{\partial t} = -\frac{1}{\epsilon_1}\boldsymbol{\nabla} \cdot \boldsymbol{v}$. This form arises from using the equation of state given in Eq. 4.4 with $\gamma = 1$ and $D = \frac{1}{\epsilon_1}$. In a sense, the equations of this formulation do not significantly differ from that of the weakly compressible SPH formulation. In one, the pressure is evolved while in the other, density is evolved. In the incompressible limit, ϵ_1 becomes zero, c_s becomes infinite, and Eq. 4.15 reduces to Eq. 4.14.

Strictly speaking, this scheme is designed to efficiently calculate a steady-state incompressible flow solution by calculating the evolution of a non-physical transient solution to steady-state.

4.3.2 Penalty $\mathcal{D}(p) = \epsilon_2 p$

If the operator $\mathcal{D}(p)$ is set proportional to p, Eq. 4.13 reduces to a diffusion equation

$$\frac{\partial p}{\partial t} - \frac{1}{\epsilon_2 \rho}\left(\boldsymbol{\nabla}^2 p - \rho\Gamma\right) = 0 \tag{4.16}$$

In this case, p (and velocity divergence) will diffuse away from sources with at a rate controlled by the diffusivity $\frac{1}{\epsilon_2 \rho}$.

An advantage of this formulation is that pressure can be removed from the problem by substituting $p = -\frac{1}{\epsilon_2}\boldsymbol{\nabla} \cdot \boldsymbol{v}$ into Eq. 4.5. Although this is an attractive step in reducing the number of variables, we have found that this formulation leads to oscillations in the velocity field and prefer the mixed formulation of solving Eq. 4.5 coupled with $p = -\frac{1}{\epsilon_2}\boldsymbol{\nabla} \cdot \boldsymbol{v}$. This mixed formulation produces smooth velocity fields, although the pressure solution can exhibit oscillations. The diffusive character of Eq. 4.6 places a restrictive time step criterion on an explicit integration of this formulation.

4.3.3 Pressure Stabilization $\mathcal{D}(p) = -\epsilon_3\left(\boldsymbol{\nabla}^2 p - \rho\Gamma\right)$

This form is motivated by the fact that in the previously mentioned forms of pressure evolution, p is susceptible to spurious, checkerboard solutions. Solving $\boldsymbol{\nabla}^2 p = \rho\Gamma$ in place of Eq. 4.2 will suppress these spurious modes by imposing an additional degree of smoothness on p [60]. If $\mathcal{D}$ is set

to $-\epsilon_3\left(\boldsymbol{\nabla}^2 p - \rho\Gamma\right)$ then Eq. 4.13 reduces to

$$\frac{\partial}{\partial t}\Big(\boldsymbol{\nabla}^2 p - \rho\Gamma\Big) + \frac{1}{\epsilon_3\rho}\Big(\boldsymbol{\nabla}^2 p - \rho\Gamma\Big) = 0 \tag{4.17}$$

which has the solution

$$\boldsymbol{\nabla}^2 p - \rho\Gamma = Ae^{-\frac{t}{\epsilon_3\rho}} \qquad \text{where} \qquad A = (\boldsymbol{\nabla}^2 p - \rho\Gamma)\Big|_{t=0} \tag{4.18}$$

This equation describes the decay of excess curvature of p to the Poisson equation consistent with the momentum equation ($\boldsymbol{\nabla}^2 p = \rho\Gamma$). As $\epsilon_3 \to 0$, the rate of decay becomes infinite and Eq. 4.17 reduces to Eq. 4.14. With this form for $\mathcal{D}$, Eq. 4.6 reduces to

$$\left(\boldsymbol{\nabla}^2 p - \rho\Gamma\right) - \frac{1}{\epsilon_3}\boldsymbol{\nabla}\cdot\boldsymbol{v} = 0$$

This technique is referred to as "pressure stabilization" [60] and is of a similar form to the equation for solving for pressure using the Pressure Projection method [122]

$$\boldsymbol{\nabla}^2 p = \frac{\boldsymbol{\nabla}\cdot\boldsymbol{v}}{\Delta t}$$

with the small parameter ϵ_3 taking the value Δt. As opposed to the Pressure Projection method, which is a fractional step method, the pressure stabilization approach solves the two equations simultaneously.

4.3.4 Pressure Correction $\mathcal{D}(p) = -\epsilon_4\frac{\partial}{\partial t}\left(\boldsymbol{\nabla}^2 p - \rho\Gamma\right)$

The pressure correction method [123, 124, 104] is a perturbation that shares some properties with both the artificial compressibility and pressure stabilization methods. The motivation for proposing this form is that projection methods based on $\nabla^2 p$ are stable with $\epsilon \sim \Delta t$ while those based on $\partial/\partial t(\nabla^2 p)$ are stable with $\epsilon \sim (\Delta t)^2$ [123]. Using this $\mathcal{D}$, Eq. 4.6 becomes

$$\Phi_{tt} + \frac{1}{\epsilon_4\rho}\Phi = 0 \tag{4.19}$$

where $\Phi = \nabla^2 p - \rho\Gamma$. This is just a simple harmonic oscillator in the term Φ and has the solution

$$\nabla^2 p - \rho\Gamma = A\sin\Big(\frac{t}{\sqrt{\epsilon_4\rho}}\Big) + B\cos\Big(\frac{t}{\sqrt{\epsilon_4\rho}}\Big) \tag{4.20}$$

where A and B are initial and boundary conditions on Φ. With this form for $\mathcal{D}$, Eq. 4.6 reduces to

$$\frac{\partial}{\partial t}\left(\nabla^2\psi - \rho\Gamma\right) - \frac{1}{\epsilon_4}\nabla\cdot\mathbf{v} = 0$$

From this form, it is clear that $\nabla\cdot\mathbf{v} \to 0$ as $\epsilon_4 \to 0$. From Eq. 4.6 we can see that $\epsilon_4 \sim \frac{t^2}{\rho}$ and that it controls the frequency of oscillation of Φ.

4.3.5 Hybrid Formulations

Each of the above forms of $\mathcal{D}$ has strengths and weaknesses. The artificial compressibility method, for example, leads to a hyperbolic equation for pressure which can be integrated efficiently, however there is no inherent dissipation mechanism for velocity divergence. The penalty method does have this dissipation, but requires prohibitively small time steps for explicit solvers. Pressure stabilization results in a smooth pressure solution, but requires solving a Poisson equation for pressure. There has been some effort in combining these methods in the hopes of combining their strengths. Several possible combinations are described below.

Telegraph – Artificial Compressibility/Penalty

The most widely studied of these hybrid formulations is the addition of a damping mechanism to the artificial compressibility method [8, 145, 110, 109, 111, 28, 78]. For example, the artificial compressibility method can be combined with the penalty method resulting in a form for $\mathcal{D}$ given by

$$\mathcal{D}(p) = \epsilon_1\frac{\partial p}{\partial t} + \epsilon_2 p$$

Convergence behavior of this form was studied by Yanenko et al. [145]. Eq. 4.13 then becomes

$$\frac{\partial^2 p}{\partial t^2} + \frac{\epsilon_2}{\epsilon_1}\frac{\partial p}{\partial t} - \frac{1}{\epsilon_1\rho}\left(\nabla^2 p - \rho\Gamma\right) = 0$$

which is the damped wave (telegraph) equation. Taking the Fourier transform of this expression leads to an equation for a damped harmonic oscillator of the transform [146]. The wave number that is critically damped in this oscillator can be adjusted by the parameters ϵ_1 and ϵ_2 and is given by:

$$\lambda = \frac{\epsilon_2}{2}\sqrt{\frac{\rho}{\epsilon_1}} \tag{4.21}$$

The primary advantage of this formulation is that a mechanism of dissipation can be retained while casting the equations in hyperbolic form, thereby removing the restrictive time step criterion of the

penalty method.

Damped Oscillator – Pressure Stabilization/Correction

Similar to the artificial compressibility method, the pressure correction method does not include a mechanism for the dissipation of velocity divergence. However, similar to the telegraph formulation, the pressure stabilization method can be combined with the pressure correction method resulting in a form for $\mathcal{D}$ given by

$$\mathcal{D}(p) = -\epsilon_3 \left(\nabla^2 p - \rho\Gamma\right) - \epsilon_4 \frac{\partial}{\partial t}\left(\nabla^2 p - \rho\Gamma\right) \tag{4.22}$$

This results in Eq. 4.13 becoming

$$\Phi_{tt} + \frac{\epsilon_3}{\epsilon_4}\Phi_t + \frac{1}{\epsilon_4 \rho}\Phi = 0 \tag{4.23}$$

This is the equation for a damped harmonic oscillator of the quantity $\Phi = \nabla^2 p - \rho\Gamma$. This system is driven to $\nabla^2 p = \rho\Gamma$ fastest when Eq. 4.23 is critically damped, which occurs when

$$\epsilon_4 = \frac{\rho \epsilon_3^2}{4} \tag{4.24}$$

Stationary Hybrid – Penalty/Pressure Stabilization

Combining the terms lacking time derivatives leads to: $\mathcal{D}(p) = \epsilon_2 p - \epsilon_3 \left(\boldsymbol{\nabla}^2 p - \rho\Gamma\right)$ This form is stationary in the sense that there is no t in Eq. 4.6, however the evolution equation (Eq. 4.13) leads to:

$$\epsilon_2 \frac{\partial p}{\partial t} - \epsilon_3 \frac{\partial}{\partial t}\left(\nabla^2 p - \rho\Gamma\right) - \frac{1}{\rho}\left(\nabla^2 p - \rho\Gamma\right) = 0 \tag{4.25}$$

This is a singular perturbation to a diffusion equation which we expect p and $\nabla \cdot v$ to follow after an initial transition layer. Convergence behavior of this form was also studied by Yanenko et al. [145].

Other hybrid forms have been proposed and studied [104], however we will focus on the above three.

Parameter Estimation

Each of the ϵ-terms carries a dimension as can be seen from each particular form of Eq. 4.6. The dimensions contain various combinations of Δx and Δt, but since we want to avoid solutions that are dependent on the particular resolution and time step, we scale the perturbations by characteristics

of the flow as follows.

$$\begin{aligned}
\epsilon_1 &\sim \tfrac{(\Delta t)^2}{\rho(\Delta x)^2} &&\sim \frac{1}{\rho V^2} \\
\epsilon_2 &\sim \tfrac{\Delta t}{\rho(\Delta x)^2} &&\sim \frac{1}{\mu} \\
\epsilon_3 &\sim \tfrac{\Delta t}{\rho} &&\sim \frac{\mu}{V^2\rho^2} \\
\epsilon_4 &\sim \tfrac{(\Delta t)^2}{\rho} &&\sim \epsilon_3^2\rho
\end{aligned}$$

V is a characteristic velocity of the flow.

4.4 SPH Implementation

4.4.1 SPH discretization

The terms of the momentum and continuity equations are discretized as follows:

$$\frac{1}{\rho}\boldsymbol{\nabla} p_i = \sum_j m_j \Big(\frac{p_j}{\rho_j^2} + \frac{p_i}{\rho_i^2}\Big)\boldsymbol{\nabla} W \tag{4.26}$$

$$\frac{1}{\rho}\,\boldsymbol{\nabla}\cdot\left(\mu_i \boldsymbol{\nabla}\boldsymbol{v}_i\right) = \frac{1}{\rho_i}\sum_j \frac{m_j}{\rho_j}(\mu_j+\mu_i)(\boldsymbol{v}_j-\boldsymbol{v}_i)\frac{(\boldsymbol{x}_j-\boldsymbol{x}_i)\cdot\boldsymbol{\nabla} \boldsymbol{W}}{|\boldsymbol{x}_j-\boldsymbol{x}_i|^2} \tag{4.27}$$

$$\boldsymbol{\nabla}\cdot\boldsymbol{v}_i = \sum_j \frac{m_j}{\rho_j}\left(\boldsymbol{v}_j-\boldsymbol{v}_i\right)\cdot\widetilde{\boldsymbol{\nabla} W} \tag{4.28}$$

$$\nabla^2 p_i = \sum_j 2\frac{m_j}{\rho_j}\left(p_j-p_i\right)\frac{(\boldsymbol{x}_j-\boldsymbol{x}_i)\cdot\boldsymbol{\nabla} \boldsymbol{W}}{|\boldsymbol{x}_j-\boldsymbol{x}_i|^2} - 2\widetilde{\boldsymbol{\nabla} p_i}\cdot\left[\sum_j \frac{m_j}{\rho_j}\widetilde{\boldsymbol{\nabla} W}\right] \tag{4.29}$$

where $\widetilde{\boldsymbol{\nabla}}$ is a corrected [18] gradient given by

$$\begin{aligned}
\widetilde{\boldsymbol{\nabla} W}_\alpha &= \mathbf{C}_{\alpha\beta}\boldsymbol{\nabla} W_\beta \\
\mathbf{C}_{\alpha\beta} &= \left[\int \left[(\boldsymbol{x}_j-\boldsymbol{x}_i)\otimes\boldsymbol{\nabla} W\right]\mathrm{d}x\right]^{-1} \\
&\simeq \left[\sum_j \frac{m_j}{\rho_j}\left(x-x_i\right)_\alpha \boldsymbol{\nabla} W_\beta\,\mathrm{d}x\right]^{-1}
\end{aligned}$$

In the above equations, the Latin indices correspond to particles while the Greek indices correspond to coordinates. This correction matrix arises from examining the Taylor series expansion of $f(\boldsymbol{x})$

and is needed to restore first order accuracy. This leads to a corrected form for the gradient operator

$$\boldsymbol{\nabla} f_i = \sum_j \frac{m_j}{\rho_j} \left(f_j - f_i\right) \widetilde{\boldsymbol{\nabla} W} \tag{4.30}$$

Although this form of the SPH gradient operator has a higher order of accuracy than Eq. 4.26, it does not guarantee conservation of momentum. Unfortunately, the form given by Eq. 4.26 cannot be corrected by using $\widetilde{\boldsymbol{\nabla} W}$ [103]. The kernel gradient in Eq. 4.27 is also not in a position to benefit from $\mathbf{C}_{\alpha\beta}$. Throughout this study, we use the quintic spline kernel given by:

$$W(s) \quad = \quad \frac{w_0}{h^n} \begin{cases} (3-s)^5 - 6(2-s)^5 + 15(1-s)^5 & : \quad 0 \leq s < 1 \\ (3-s)^5 - 6(2-s)^5 & : \quad 1 \leq s < 2 \\ (3-s)^5 & : \quad 2 \leq s < 3 \\ 0 & : \quad s > 3 \end{cases}$$

where w_0 is given by $\frac{1}{120}$, $-\frac{7}{478\pi}$, $-\frac{3}{359\pi}$ in 1, 2, and 3 dimensions respectively.

4.4.2 Time Integration

Eq.'s 4.5 and 4.6 are integrated explicitly for the telegraph perturbation as follows.

$$\begin{aligned} \boldsymbol{v}^{(n+1)} &= \boldsymbol{v}^n + \Delta t \Big[\frac{1}{\rho} \boldsymbol{\nabla} \cdot \Big(\mu \boldsymbol{\nabla} \boldsymbol{v}^n \Big) + \boldsymbol{g} - \frac{1}{\rho} \boldsymbol{\nabla} p^n \Big] \\ p^{(n+1)} &= p^n + \Delta t \Big[- \frac{\epsilon_2}{\epsilon_1} p^n - \frac{1}{\epsilon_1} \boldsymbol{\nabla} \cdot \boldsymbol{v}^n \Big] \end{aligned}$$

Since in this study, we are primarily focusing on the slow flow of a very viscous fluid, the hybrid methods were also implemented using an implicit scheme. Although only first order accurate, we choose the Backward Euler scheme due to its large stability region.

Using the pressure boundary condition (described more fully in Sec. 4.4.4)

$$\frac{\partial}{\partial n} p^{(n+1)} = \hat{\boldsymbol{n}} \cdot \left[(\rho \boldsymbol{g}) + \boldsymbol{\nabla} \cdot \Big(\mu \boldsymbol{\nabla} \boldsymbol{v}^{(n+1)} \Big) \right]$$

the variables v and p are integrated for the implicit telegraph form according to

$$\begin{bmatrix} \mathbf{A} & \mathbf{B}_1 & \mathbf{B}_2 \\ \mathbf{C} & \mathbf{D}_1 & \mathbf{D}_2 \\ \mathbf{E} & \mathbf{F}_1 & \mathbf{F}_2 \end{bmatrix} \begin{bmatrix} \boldsymbol{v} \\ p \\ p_g \end{bmatrix}^{(n+1)} = \begin{bmatrix} \boldsymbol{v} + \Delta t \boldsymbol{g} \\ p + \Delta t \frac{\beta^2}{\eta} \rho \Gamma \\ \hat{\boldsymbol{n}} \cdot (\rho \cdot \boldsymbol{g}) \end{bmatrix}^{(n)} \tag{4.31}$$

where

$$\begin{aligned} \mathbf{A} &= \mathbf{1} - \Delta t\left[\tfrac{1}{\rho}\,\boldsymbol{\nabla}\cdot\left(\mu\boldsymbol{\nabla}\right)\right] & \mathbf{B} &= \tfrac{\Delta t}{\rho}\boldsymbol{\nabla} \\ \mathbf{C} &= \Delta t\beta^2\boldsymbol{\nabla}\cdot & \mathbf{D} &= \mathbf{1} + \Delta t\tfrac{\epsilon_2}{\epsilon_1} \\ \mathbf{E} &= -\hat{\boldsymbol{n}}\cdot\boldsymbol{\nabla}\cdot\left(\mu\boldsymbol{\nabla}\right) & \mathbf{F} &= \hat{\boldsymbol{n}}\cdot\boldsymbol{\nabla} \end{aligned}$$

Particle positions are then updated according to

$$\boldsymbol{x}^{(n+1)} = \boldsymbol{x}^{(n)} + \Delta t\boldsymbol{v}^{(n+1)}$$

D takes other forms for the damped oscillator and stationary hybrid methods.

The matrix in Eq. 4.31 is not symmetric and is, in general, sparse. To solve for the vector of unknowns, we use the GMRES routine from the SPARSKIT package [114].

One of the benefits of Lagrangian fluid schemes such as SPH is that the acceleration term is the full material time derivative which removes the need to deal with the non-linear advective term. For the scheme as described above to calculate the correct velocities at the correct positions at the next time step, the positions would need to be updated throughout the iterative process based on the current best estimate of $\boldsymbol{v}^{(n+1)}$, a quantity not readily available from the SPARSKIT GMRES routine [114]. This would require a reassessment of all interacting pairs which would dramatically increase the computational effort as well as meddle with the structure of **A**. In the scheme we employ, the velocities calculated are essentially based on $\frac{\partial \boldsymbol{v}}{\partial t}$, not $\frac{\mathrm{D}\boldsymbol{v}}{\mathrm{D}t}$, however for slow flows, the difference is negligible and in the limit of Stokes flow, all accelerations tend to zero. For flows with a non-negligible advective term, the velocities generated from the iterative solver would have to be modified to include the $\boldsymbol{v}\cdot\boldsymbol{\nabla}\boldsymbol{v}$ term.

4.4.3 Evolution of a velocity divergence source on a periodic patch

These tests show the evolution of velocity divergence errors for various perturbations to the continuity equation. In all the patch test cases Eq.s 4.5 and 4.6 are solved on a unit square with 6400 particles placed on a grid with an average spacing of 0.0125 m. The time step was held fixed at 0.0001 s, and the material properties were constant at $\rho = 1.0$ kg/m^3 and $\mu = 1.0$ Pa s. The stopping criterion was given by

$$||\text{residual}|| \leq 10^{-7} * ||\text{initial residual}|| + 10^{-10}$$

All particles were initialized with a zero velocity except for the divergence source, a region where the velocity field has a specified divergence. All particles within a radius of $r_0 = 0.1$ from $\boldsymbol{x}_0 = (0.3, 0.3)$ have a velocity initialized according to

$$\boldsymbol{v} = -\frac{0.01}{r_o}\frac{\boldsymbol{x}_0 - \boldsymbol{x}}{||\boldsymbol{x}_0 - \boldsymbol{x}||}$$

In all cases, the quintic spline kernel was used with a fixed smoothing length of 1.2 times the initial particle spacing. This kernel uses a broader support region than the widely used cubic spline kernel which increases the number of interacting particles and therefore the computational cost of each Matrix-Vector multiplication. However, the quintic spline is known to improve the stability of interpolating higher-order derivatives [89], which generally leads to faster convergence of the iterative solver resulting in an insignificant difference in the total computational cost. For larger problems, the cubic spline may be more efficient due to its smaller memory footprint.

The evolution of an initial velocity divergence on a unit square with periodic boundary conditions can be seen in Fig. 4.1. The shading in this figure corresponds the magnitude of the velocity divergence with each plot scaled according to the minimum and maximum for that time step. This figure provides a check that the velocity divergence evolves according to Eq. 4.12. We expect, for example, that since the artificial compressibility method leads to the propagation of pressure waves (Eq. 4.15), $\nabla \cdot \boldsymbol{v}$ should behave similarly. The plots in the top row of Fig. 4.1 demonstrate that when integrating Eq. 4.6, perturbations in $\nabla \cdot \boldsymbol{v}$ propagate as expected. The penalty method resulted in a diffusion equation for pressure so we expect that $\nabla \cdot \boldsymbol{v}$ should behave similarly, as we can see from the second row from the top in Fig. 4.1. With both the pressure stabilization method and the pressure correction method, there is not a mechanism for the transport of pressure perturbations, only the decay or oscillation of the quantity $\nabla^2 p - \rho\Gamma$. As expected, there is no transport of the quantity $\nabla \cdot \boldsymbol{v}$ in the test patch.

4.4.4 Boundary Conditions

Boundary conditions with SPH generally require some additional attention since the overlapping "shape functions" from the kernel do not retain the delta property needed for enforcing essential boundary values [43, 49, 143, 136]. Boundary conditions are usually imposed either through fixed boundary particles, or through ghost particles which are positioned so that the boundary is a line of symmetry of the fluid [66]. The ghost particles inherit properties of the corresponding source particle in the interior. In this study, ghost particles are used to impose boundary conditions.

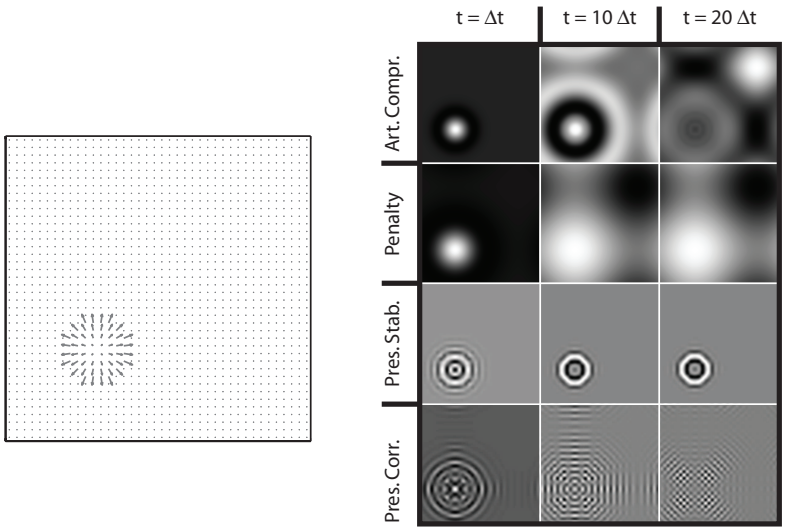

Figure 4.1: Periodic patch with a velocity divergence source. The evolution of $\nabla \cdot v$ for each perturbation type can be seen on the right.

Solid Wall Boundary Conditions (Ghost particles)

Ghost particles are placed as shown in Fig. 4.2. Each particle that interacts with a boundary element is projected across that element (i.e. particle P is projected across element B_{e2} producing ghost particle G_5). Near concave corners in the boundary, such as near boundary point B_{p1}, interior particles must also be mapped through the corners to prevent a ghost particle deficiency in the wedge-shaped region near G_2. In this case, the interior particle N_1 produces three ghost particles, G_1, G_3, and G_2 by projecting the position across boundary elements B_{e1} and B_{e2} and through boundary point B_{p1}. Near convex corners, such as near boundary point B_{p2}, the problem is not a deficiency of ghost particles, but a duplicity. In this case, interior particles are projected only across elements and the resulting ghost particle accepted only if the position is in the closer half of the bisection. For example, particle N_4 projects across B_{e3} to G_6 and is accepted while N_2 projects across B_{e2} to G_4 which is in the further half and is therefore rejected. Note that particle N_3 does not produce a ghost particle since it does not project orthogonally onto either B_{e2} or B_{e3}. The ghost particles are included in the summations when they are within the support domain even if their source particle is not (i.e. G_7 is in the support domain of P while its source N_5 is not.).

Velocity Boundary Conditions Although it is cumbersome to map the position of the ghost particles at each step, an advantage of this arrangement is that it produces a line of symmetry which

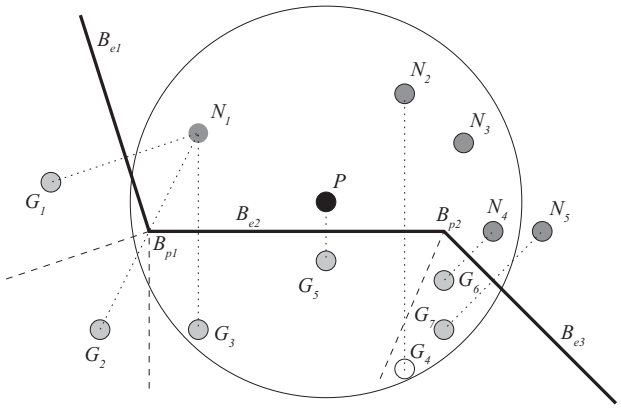

Figure 4.2: Ghost particles are positioned by projecting the interior particles across boundaries.

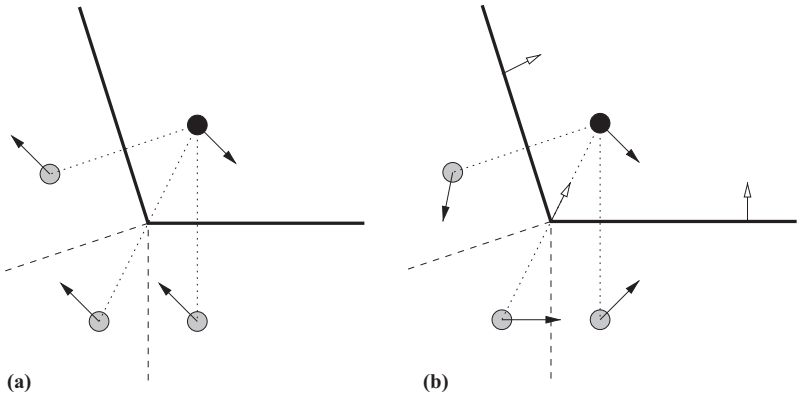

Figure 4.3: Velocity boundary conditions for no-slip (a) and free-slip (b) walls.

simplifies enforcing free-slip and no-slip boundary conditions. For the no-slip condition all velocities of the ghost particles are the negated value of the source particle (Fig. 4.3a). This ensures that the velocity will go to zero at the boundary. For the free-slip condition, the ghost particle inherits the velocity of the source particle with the component of the velocity perpendicular to the corresponding boundary negated (Fig. 4.3b). This configuration ensures that the ghost particle will not impede tangential flow along the boundary while preventing (or discouraging) the interior particle from crossing the boundary. The normal used for negating the component of the source particle's velocity is the same as that used for positioning the ghost particle. For example, in Fig. 4.3b, all three ghost particles inherit velocity V_1, but with components negated with respect to n_1, n_2, and n_3 respectively.

For boundary geometries where a free-slip element joins a no-slip element (such as the viscous droplet case of section 4.6.2), the ghost particles in the wedge-shaped region are located as in Fig. 4.4b. Ghost particles for which $\alpha < \beta$ acquire a velocity according to B_1 while those for which the converse is true use B_2.

Moving or traction boundaries can be included by simply supplementing the free-slip or no-slip velocities with that of the boundary.

A point to note with this configuration is that normal velocities are encouraged to tend to zero at the boundary by imposing a non-zero velocity divergence at the boundary. This essentially means that solid-wall boundaries are sources of divergence errors. Using a penalty formulation, divergence errors will diffuse away to zero if $\boldsymbol{\nabla} \cdot \boldsymbol{v} = 0$ at the boundary. If not, divergence errors can diffuse into the domain.

Pressure Boundary Conditions Homogeneous Neumann pressure boundary conditions are sometimes imposed by assigning to each ghost particle the pressure of that ghost particle's source. This arrangement leads to the boundary being a line of symmetry of the pressure field and therefore ensures that $\partial p/\partial n$ vanishes on the boundary. The pressure of the ghost particles is no longer an unknown which leads to faster convergence of the iterative solver. Unfortunately, for flows with body forces or with large viscous forces, a homogeneous Neumann pressure condition leads to a poor approximation of flow dynamics [42]. Boundaries will eventually leak particles if there is an insufficient pressure gradient to oppose the flow in spite of the anti-symmetric velocity of the ghost particles. For these flows, the pressure boundary condition can be found by taking the dot product of the momentum equation (Eq. 4.1) with the normal and assuming normal velocities and accelerations go

to zero on the boundary [96].

$$\frac{\partial p}{\partial n} = \hat{\boldsymbol{n}} \cdot \left[(\rho \boldsymbol{g}) + \boldsymbol{\nabla} \cdot \Big(\mu \boldsymbol{\nabla} \boldsymbol{v} \Big) \right]$$

Since the Laplacian calculation can deteriorate for the ghost particles due to the deficient kernel support, we neglect the viscous term of the above expression. In the limit of Stokes flow, this neglect should result in minor errors. Moreover, as noted by Gresho [41], the neglect of this term can lead to the diffusion of $\boldsymbol{\nabla} \cdot \boldsymbol{v}$ errors from the boundaries into the domain.

With an explicit integration scheme, pressure values for the ghost particles are incremented from its source particle's pressure according to its relative position and the pressure gradient. For an implicit integration scheme, we have found it to be more stable to allow the pressure value to be an unknown subject to the constraint that the pressure gradient satisfy the boundary condition. Since

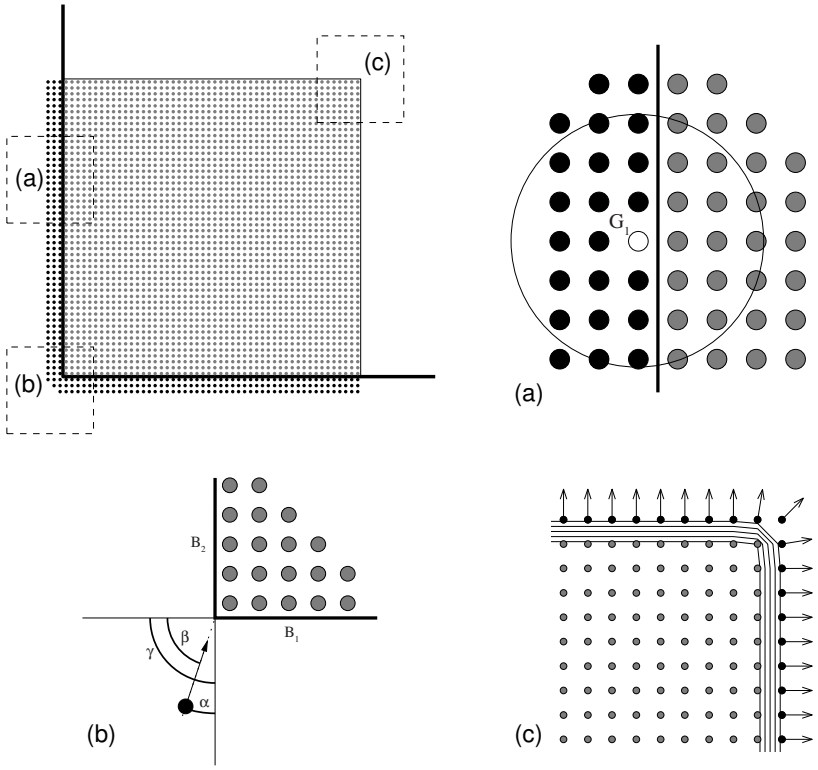

Figure 4.4: Geometry of bounded patch. Solid walls are along the base and left side. The top and right sides are free-surfaces. (a) illustrates the kernel deficiency of the ghost particles, (b) diagrams the ghost particles in the corners, (c) shows the identification of free-surface particles (from the kernel volume) and the associated surface normal.

nearly all ghost particles will have a deficient support domain (see Fig. 4.4a), the pressure gradient equation used for imposing the boundary conditions is the corrected form given in Eq. 4.30.

Free-Surface Boundary Conditions

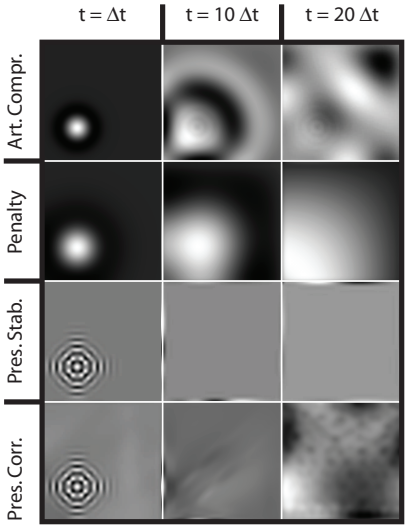

Figure 4.5: Bounded patch with a velocity divergence source. The evolution of $\nabla \cdot v$ for each perturbation type can be seen.

Free surfaces are identified by flagging particles whose support domain falls below a threshold value (0.82 for the quintic kernel) as shown in Fig. 4.4c. A similar identification process was used by Shao and Lo [120] but with a much higher threshold. We found that this threshold value, however usually results in an identified surface that is continuous and one particle thick. The boundary condition we would like to impose on this surface is that it is traction-free. We can approximate this condition by setting the pressure to zero, however, this allows deviation from the divergence-free velocity constraint.

Evolution of a velocity divergence source on a bounded patch

To test the effect of these velocity and pressure boundary conditions applied at both solid walls and surfaces, on the evolution of $\nabla \cdot \boldsymbol{v}$, the same tests as described in Sec. 4.4.3 were run using a bounded patch. The boundary configurations is as shown in Fig. 4.4a with solid walls on the left and bottom sides of the patch and a surface elsewhere. This test is important because although $\nabla \cdot \boldsymbol{v}$

and p evolve in concert, the boundary conditions applied for $\boldsymbol{v}$ at walls and p at free-surfaces can be thought of as non-zero boundary conditions on $\nabla \cdot \boldsymbol{v}$.

From the top row of Fig. 4.5, we see that both the wall and free-surface behave as a reflective boundary for the waves of $\nabla \cdot \boldsymbol{v}$. The penalty case is similar in that neither type of boundary transports $\nabla \cdot \boldsymbol{v}$ out of the domain. Ideally, these boundary should be absorbing to most rapidly remove $\nabla \cdot \boldsymbol{v}$ from the patch, however they do not behave as sufficient sources of $\nabla \cdot \boldsymbol{v}$ to corrupt the solution. The pressure stabilization method does lead to large values of $\nabla \cdot \boldsymbol{v}$ that persist near the boundaries. The pressure correction method also retains the largest $\nabla \cdot \boldsymbol{v}$ near the boundaries.

Instead of setting $p = 0$, an alternative boundary condition at free-surfaces is to require that the surface particles remain divergence-free and to assign the pressure necessary to enforce this constraint. Although, this boundary condition did reduce velocity divergence errors, it also required approximately 10% more iterations for the solver to converge. In the tests of sections 4.5 and 4.6, the free-surface boundary condition, $p = 0$, was used.

4.5 Numerical tests – Transient viscous shear flow

To study the performance of the quasi-compressible SPH formulation for viscous free-surface flow, the transient flow of a thin sheet of fluid down an inclined plane was chosen as a test problem. A schematic of this test problem is shown in Fig. 4.6. The density and viscosity of the fluid were set to $\rho = 10^3\,\mathrm{kg/m^3}$ and $\mu = 10^{-1}\,\mathrm{Pa\,s}$ with a depth of $h = 0.6\,\mathrm{mm}$ and a slope of $10°$. The transient and steady-state solutions for this test problem are:

$$\begin{aligned}
\boldsymbol{v}_{x[ss]} &= \frac{\rho g \sin\theta}{2\mu}\Big(y^2 - 2yh\Big) \\
\boldsymbol{v}_x(y,t) &= \boldsymbol{v}_{x[ss]} + \sum_{n=1}^{\infty} a_n \sin\Big(\frac{n\pi y}{h}\Big)\, \exp\Big[-\frac{\mu}{\rho g \sin\theta}\Big(\frac{n\pi}{h}\Big)^2 t\Big] \\
a_n &= \frac{2}{h}\int_0^h -\boldsymbol{v}_{x[ss]} \sin\Big(\frac{n\pi y}{h}\Big)\,\mathrm{d}y \qquad (4.32) \\
&= \frac{16 g h^2 \rho \sin\theta}{n^3 \mu \pi^3} \qquad \text{(If } n \text{ is odd.)} \qquad (4.33)
\end{aligned}$$

This is essentially the solution given by Morris et al. [89] for transient Poiseuille flow. The model set-up consists of an array of 12 by 12 particles with an average spacing of $5\,\mathrm{x}\,10^{-5}\,\mathrm{m}$, a no-slip boundary along the base and periodic conditions in the downslope direction. Although solving for the pressure and velocity profiles is really a one-dimensional problem, it is useful to simulate the flow in two dimensions to see the effect, if any, of particle disorder.

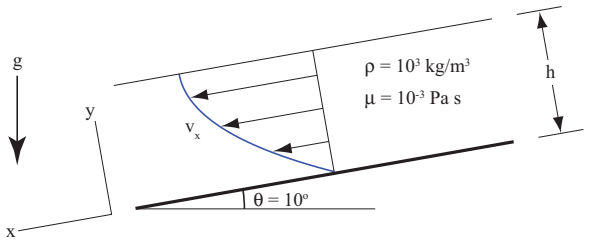

Figure 4.6: Schematic of the test case for the transient viscous flow down an inclined plane.

4.5.1 Explicit Integration

As an initial test, the system was evolved to 0.02 s using the WCSPH formulation. The most restrictive constraint on the time step for this problem is due to the viscosity ($\Delta t = \rho h^2/8\mu = 3.125 \times 10^{-6}$ s), requiring approximately 6400 time steps. We found that we could increase the time step slightly 4.5×10^{-6} s and still maintain a stable solution. The speed of sound, which controls the pressure response to density perturbations and therefore the compressibility, was set so that the associated time step restriction from the CFL condition was comparable to the viscous restriction. Pressure and velocity profiles at $t = 0.02$ s for the WCSPH solution are shown in Fig. 4.7. Despite the course resolution, the velocity solution matches the analytic solution very well, although the pressure solution shows some perturbations from the expected linear profile. As mentioned above, this problem is solved on a 2-dimensional domain to verify that the deformation does not significantly effect the solution. This was found to be the case. All 144 particles are plotted in Fig. 4.7.

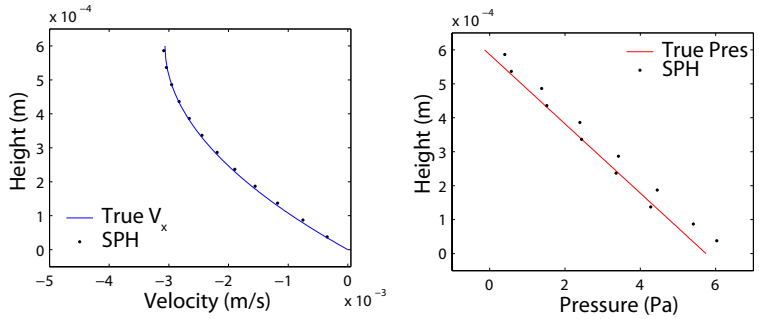

Figure 4.7: Solution for transient shear flow at $t = 0.02$ s using explicitly integrated WCSPH.

For comparison, the pressure and velocity profiles at $t = 0.02\,\mathrm{s}$ for the explicitly integrated quasi-compressible telegraph ($\epsilon_1 = 10^{-5}$, $\epsilon_2 = 10^{-8}$) model are shown in Fig. 4.8. The time step for this formulation is also constrained by the viscosity. The value of ϵ_1 was chosen so that its associated time step restriction was comparable to that from the viscosity. As with the WCSPH formulation, the explicit telegraph formulation returns a velocity solutions that compares very well with the analytic solution. The pressure solution does not show the same perturbations as seen with the WCSPH solution, but the values are slightly greater than the analytic solution.

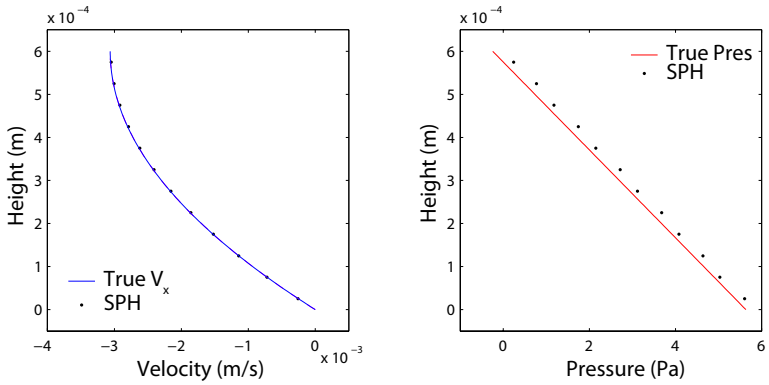

Figure 4.8: Solution for transient shear flow at $t = 0.02\,\mathrm{s}$ using explicitly integrated telegraph formulation.

To determine how well the telegraph formulation enforces incompressibility, cases were run with ϵ_1 spanning the range from 10^{-1} to $10^{-5.5}$ and ϵ_2 spanning the range from 10^{0} to 10^{-8}. Since the time step in each of these cases was set by the viscosity, each case used the same number (4445) of steps. The degree to which the incompressible transient Stokes equations were satisfied is expressed with four measures: the relative error of the solution (velocity and pressure), the relative error in the final thickness of the sheet of fluid, the average velocity divergence, and the maximum velocity divergence. These measures, as a function of ϵ_1 and ϵ_2, are contoured along the top row of Fig. 4.9.

The expectation is that one perturbation or the other of the hybrid formulation (either $\epsilon_1 \frac{\partial p}{\partial t}$ or $\epsilon_2 p$) will provide the dominant balance against $\nabla \cdot \boldsymbol{v}$ in Eq. 4.6. If $\epsilon_2 << \epsilon_1$, the system will behave similar to the artificial compressibility method. If $\epsilon_1 << \epsilon_2$, then $\nabla \cdot \boldsymbol{v}$ will diffuse as in the penalty method. If the two ϵ–terms are of the same order of magnitude, then $\nabla \cdot \boldsymbol{v}$ should evolve according to the damped wave equation. The top row of Fig. 4.9 shows that there is a transition from one dominant behavior to the other. For this explicit case in which the time step is constrained by the viscosity, all points on the ϵ_1–ϵ_2 range require the same computational effort. As such, there

is no reason to choose any ϵ_1–ϵ_2 pair other than the most restrictive, the pair that results in the lowest error. For the implicit integration scheme, the different choices of ϵ_1 and ϵ_2 results in differing numbers of iterations required by the solver.

4.5.2 Implicit Integration

Using an implicit integration scheme removes the restrictive time step criterion associated with the high viscosity. Additionally, it also removes time step restrictions associated with ϵ_1 and ϵ_2 allowing for smaller perturbations to Eq. 4.6. The telegraph formulation was run with ϵ_1 over the range 10^0 to 10^{-7} and ϵ_2 spanning the range from 10^0 to 10^{-8}. In these cases, 20 time steps of $\Delta t = 0.001$ were used and a convergence criterion for the iterative solver given as follows.

$$||\text{residual}|| \leq 10^{-5} * ||\text{initial residual}|| + 10^{-8}$$

Results for the same four measures of error are contoured in the second row of Fig. 4.9. The results show the same pattern of error as with the explicit integration. This is to be expected since the underlying equations are the same. Error results from the other two hybrid formulations (stationary hybrid and damped oscillator) are also displayed in Fig. 4.9 over a range of their respective perturbation parameters. In each formulation, there is a transition from one end member of the hybrid formulation to the other.

Fig. 4.9 shows how well incompressibility is approximated for each hybrid formulation over the range of ϵ–values, however it does not show how efficiently the constraint is enforced, or how much numerical effort is required. For the three implicit hybrid formulations, the total number of iterations required for the 20 time steps, as a function of the two perturbation parameters, is contoured in Fig. 4.10. In each of the three hybrid formulations, the total number of iterations required increases as each of the perturbation terms decrease. This is expected since negligible ϵ–values leads to the constraint $\nabla \cdot \boldsymbol{v} \simeq 0$ which results in a numerically expensive elliptic system of equations. There is essentially a trade-off between numerical effort and the enforcement of incompressibility. However, for this implicitly integrated viscous flow problem, any choice of formulation, whether one of the hybrid formulations or any of the individual perturbations, results in less numerical effort that the explicit formulations. Although it is not straight-forward to directly compare the implicit and explicit schemes, with the convergence criterion given above, the implicit methods require approximately a third as many calls to the matrix-vector multiply routine as do the explicit methods. This could possibly be further reduced by preconditioning. There are, however, additional storage requirements for the implicit formulation.

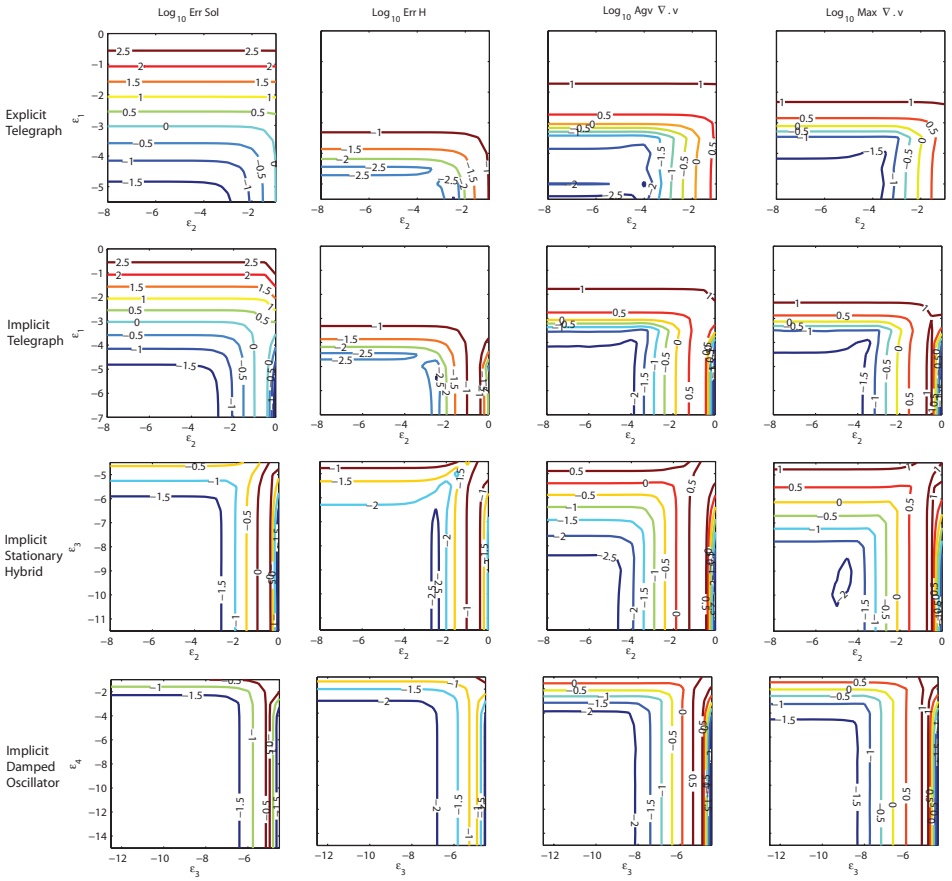

Figure 4.9: Various error/$\nabla \cdot v$ measures for the hybrid formulations.

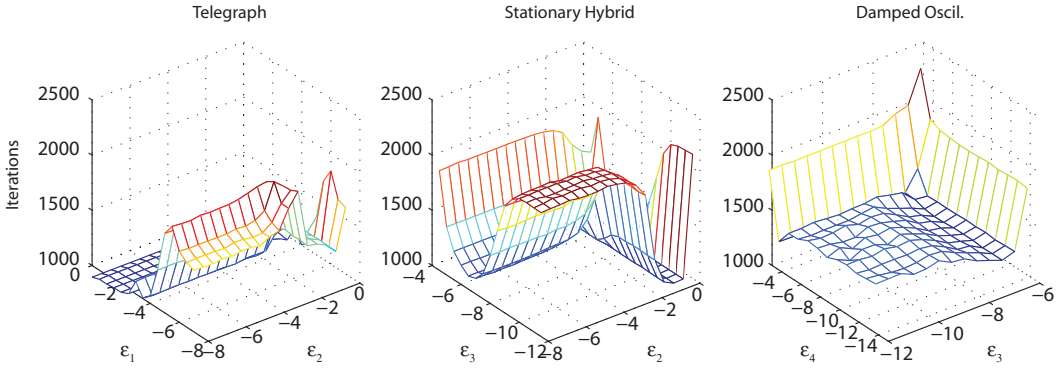

Figure 4.10: Total number of iterations required for the three implicit hybrid formulations.

A point to note in Fig. 4.10, is that both the telegraph and damped oscillator formulations show a simple increase in numerical effort with decreasing ϵ (any of ϵ_{1-4}). The stationary hybrid, in contrast, shows a trough of fewer iterations along $\epsilon_3 = 10^{-7}$. A similar pattern will be seen in Sec. 4.6 where it is found to be related to the suppression of pressure oscillations. An ϵ_3 too small allows pressure oscillations to occur while an ϵ_3 too large does not provide an adequate constraint on $\nabla \cdot \boldsymbol{v}$. It is not clear to what extent the optimal choice of ϵ_3 is problem dependent.

4.6 Numerical tests – Stokes Flow

In the case of stationary Stokes flow, accelerations are negligible resulting in the following equations.

$$\frac{1}{\rho}\boldsymbol{\nabla}\cdot\left(\mu\boldsymbol{\nabla}\boldsymbol{v}^{(n+1)}\right) - \frac{1}{\rho}\boldsymbol{\nabla}p^{(n+1)} = -\boldsymbol{g}$$
$$\epsilon_2 p^{(n+1)} - \epsilon_3\nabla^2 p^{(n+1)} - \frac{1}{\epsilon_1}\boldsymbol{\nabla}\cdot\boldsymbol{v}^{(n+1)} = 0$$

The continuity equation is perturbed using the stationary hybrid formulation. This scheme is applied to two test cases: lid-driven shear flow in a square cavity, and the collapse of a viscous droplet.

4.6.1 Lid-driven shear flow in a square cavity at $Re = 1$

The circulation of fluid in a square cavity with a tangential velocity applied along the top boundary, is a classic problem in fluid mechanics [27, 100]. We used the boundary conditions, geometry, and material properties as described by Liu and Liu [66] and shown in Fig. 4.11 which results in a Reynolds number of $Re = 1$. 1600 regularly-spaced particles were used with an average spacing of $s = 2.5\,\mathrm{x}\,10^{-5}$ m.

The steady-state solution was calculated with the stationary hybrid formulation with ϵ_2 spanning the range from 10^0 to 10^{-8} and ϵ_3 spanning the range from 10^0 to 10^{-12}. For the case of the most restrictive perturbation ($\epsilon_2 = 10^{-8}$ and $\epsilon_3 = 10^{-12}$), plots of the velocity along the two mid-lines and pressure along the top boundary are shown in Fig. 4.12. This choice of ϵ_2 and ϵ_3 results in essentially the same solution as simply solving the Stokes equations (i.e. $\boldsymbol{\nabla}\cdot\boldsymbol{v} = 0$). The SPH solution is plotted with symbols while a solution using a finite difference method with a staggered-MAC grid [27] is shown as a line. The velocity solution is smooth, but the pressure solution suffers a checkerboard oscillation.

Fig. 4.13 shows the effect of increasing ϵ_2 and ϵ_3 on the solution and the computational expense. The total number of iterations required, the maximal velocity divergence and the relative error for

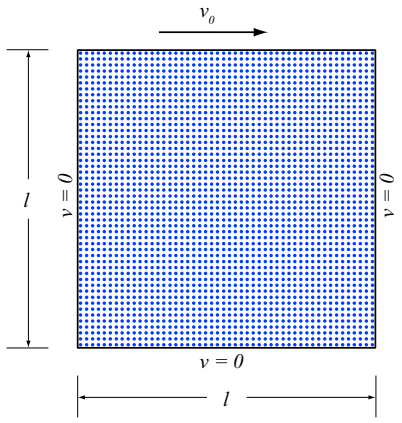

Figure 4.11: Initial particle positions for the lid-driven flow in a square cavity. In this problem, $v_0 = 10^{-3}\,\mathrm{m/s}$, $l = 10^{-3}\,\mathrm{m}$, $\mu = 10^{-3}\,\mathrm{Pa\,s}$, $\boldsymbol{g} = 0\,\mathrm{m/s^2}$, and $\rho = 10^3\,\mathrm{kg/m^3}$ resulting in $Re = 1$.

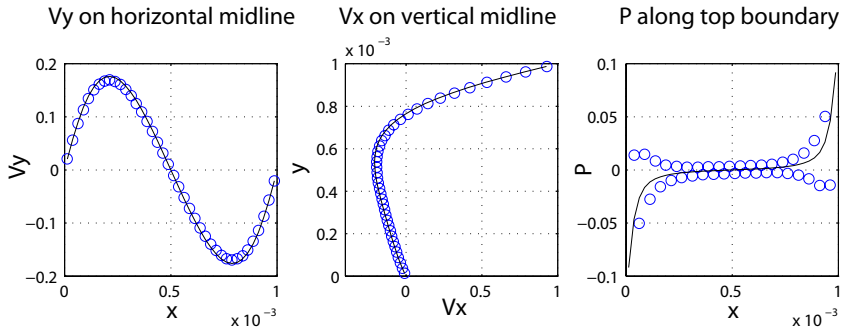

Figure 4.12: Lid-driven shear flow solution profiles at $\log \epsilon_2 = -8$, $\log \epsilon_3 = -12$.

the suite of ϵ_2–ϵ_3 values are plotted in Fig. 4.13. The relative error is given by

$$\text{Relative Error} = \left[\sum_i \left(\frac{u_0 - u}{u_0} \right)^2 \frac{m_i}{\rho_i} \right]^{0.5} \tag{4.34}$$

where u is the SPH solution (in both $\boldsymbol{v}$ and p) and u_0 is the true solution. A finite difference solution on a MAC grid was considered the true solution.

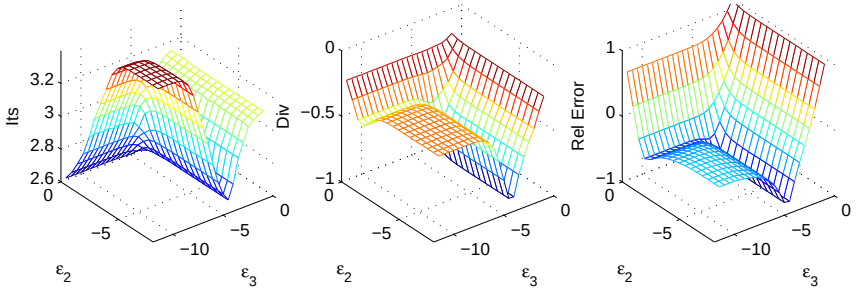

Figure 4.13: Log of iterations, velocity divergence, and relative error (compared with MAC solution) for the lid-driven flow test case with the stationary hybrid perturbation.

A striking feature of all three surface plots in Fig. 4.13 is the prominent trough along $\epsilon_3 = 10^{-4.5}$. The reduction in the error coupled with the increased convergence rate makes this a desirable choice for ϵ_3. This benefit is primarily a result of the pressure stabilization (ϵ_3) term smoothing the pressure solution. If ϵ_3 is very small, $\nabla^2 p$ can be large (i.e. oscillatory p) and still have the $\epsilon_2 p$ term be the dominant balance against $\nabla \cdot \boldsymbol{v}$. If ϵ_3 is too large, then $\nabla \cdot \boldsymbol{v}$ will be far from zero. Results of a case with perturbation parameters in this trough ($\epsilon_2 = 10^{-3}$ and $\epsilon_3 = 10^{-4.5}$) are shown in Fig. 4.14.

The SPH solution will be more susceptible to pressure oscillations when the particles are regularly spaced [66]. This is because a regular spacing can give rise to zero-energy modes which allow a checker-boarding of the pressure solution. Irregular spacing should suppress these zero-energy modes, however we have found this pressure oscillation to be persistent even with particle disorder when pressure smoothing is not included ($\epsilon_3 \sim 10^{-12}$). In Fig. 4.15, a disordered array of particles is shown which was generated by displacing, in both x and y, each of the regularly-spaced particles by a random amount between $-0.4s$ and $0.4s$, where s is the initial particle spacing. Using this array, the same suite of cases were run and results for the pairs $\epsilon_2 = 10^{-8}$, $\epsilon_3 = 10^{-12}$ and $\epsilon_2 = 10^{-3}$, $\epsilon_3 = 10^{-4.5}$ shown in Fig.s 4.16 and 4.17, respectively.

As can be seen in Fig. 4.16, the velocity solution when using $\epsilon_2 = 10^{-8}$, $\epsilon_3 = 10^{-12}$ is adequate,

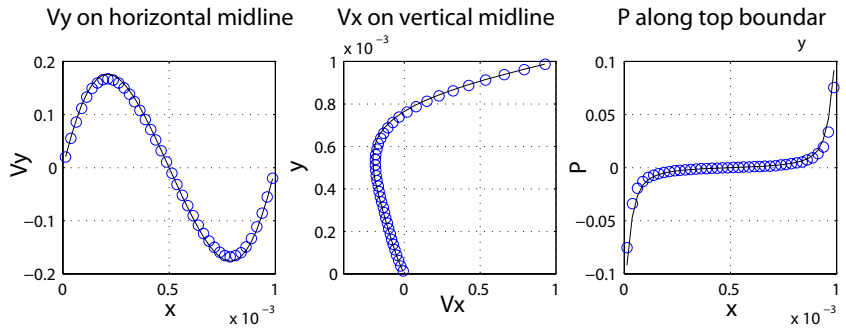

Figure 4.14: Lid-driven shear flow solution profiles at $\log \epsilon_2 = -3$, $\log \epsilon_3 = -4.5$.

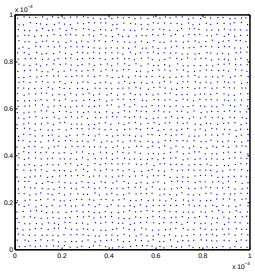

Figure 4.15: Lid-driven shear flow disordered particle configuration.

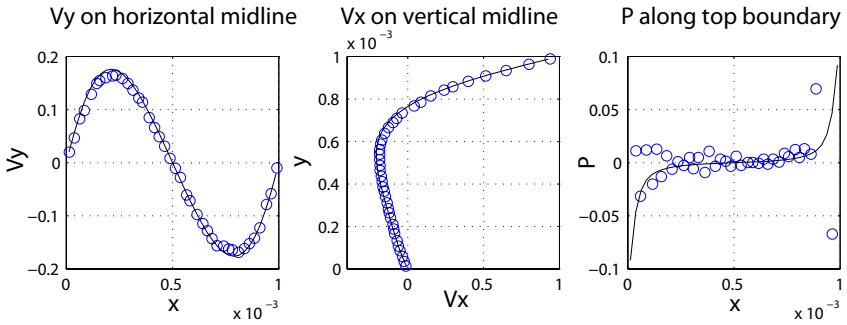

Figure 4.16: Profiles at $\log \epsilon_2 = -8$, $\log \epsilon_3 = -12$ with disordered particles. The pressure solution remains noisy despite the disordered array.

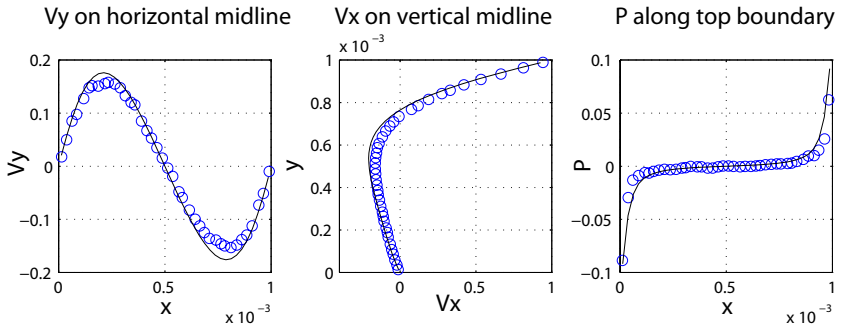

Figure 4.17: Profiles at $\log \epsilon_2 = -3$, $\log \epsilon_3 = -4.5$ with disordered particles.

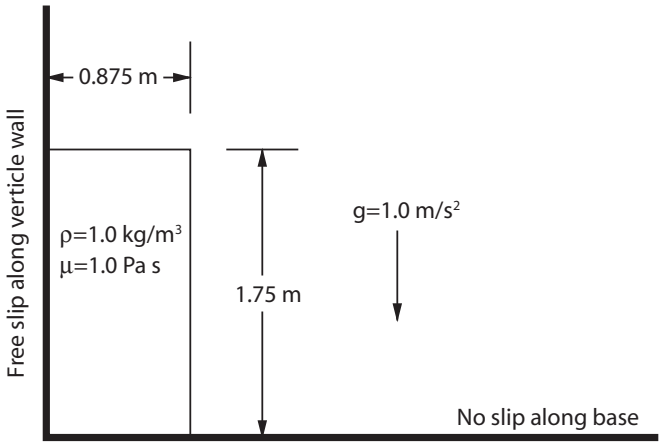

Figure 4.18: Viscous droplet initial configuration.

but the pressure solution shows strong oscillations. Using the pair $\epsilon_2 = 10^{-3}$, $\epsilon_3 = 10^{-4.5}$ results in a smoother pressure solution, although the velocity solution is degraded (Fig. 4.17).

4.6.2 Collapse of a viscous droplet

As a final test case, we model the creeping collapse of a viscous droplet. The model configuration is shown in Fig. 4.18 and consists of a square of fluid (1.75 m by 1.75 m) with $\rho = 1.0\,\mathrm{kg/m^3}$, $\mu = 1.0\,\mathrm{Pa\,s}$ and $g = 1.0\,\mathrm{m/s^2}$. Due to symmetry, only half of the domain is modeled. This is the same configuration used by Betulu et al. [4] who modeled the collapse using a boundary element method.

For the initial profiles, we will compare the SPH solution with the boundary element solution

from Betulu et al. [4]. A similarity solution exists [53] for the advance of a viscous gravity current which we will compare with the late-stage behavior of the collapsing droplet. The profile of the advancing front of the collapse of a droplet will approach this similarity solution, regardless of the initial shape of the droplet. Essentially, the initial profile will diffuse towards the similarity solution.

The line of symmetry along the left boundary corresponds to a free-slip velocity boundary condition and a homogeneous Neumann pressure condition. The boundary condition along the base is no-slip. Since the origin is a stagnation point of the flow, there is a tendency for the SPH particles to accumulate in this region. To mitigate this effect, the SPH particles are initially placed in a hexagonal configuration [86]. For this gravity-driven flow, it is important to use the full Neumann pressure boundary condition as outlined in section 4.4.4. Using a homogeneous Neumann boundary condition for pressure is insufficient and will allow particles to leak across the boundary.

SPH results of the initial collapse are compared with the BEM solution in Fig. 4.19. The evolution of the SPH solution matches the evolution of the surface profiles of the BEM solution, however the timing of the two solutions is not consistent with the SPH solution arriving at a profile before the BEM solution predicts.

As the droplet collapses, variations in the initial profile decay towards the similarity solution. A comparison of the late-stage behavior of the SPH solution with the similarity solution of Huppert [53] is shown in Fig. 4.20. In this case the timing of the profile from the similarity solution matches the timing of the profile of the SPH solution.

4.7 Conclusions

In any numerical method, the incompressibility constraint is a global restriction that is difficult or expensive to enforce. With Eulerian, grid-based methods, a commonly used technique is to add a pressure perturbation to the continuity equation that leads to an evolution of pressure. This transient non-physical solution can be integrated to a steady-state solution, a solution that solves the true steady-state, incompressible flow problem. With a Lagrangian particle scheme, advecting the particles during this non-physical transient phase does not result in a steady-state solution and does not guarantee that incompressibility will ultimately be achieved. In the traditional WCSPH formulation which evolves density through the continuity equation and an equation of state, there is an implicit acceptance of an error in the incompressibility condition, an error that can be quantified and adjusted based on the imposed speed of sound. However, since the WCSPH formulation treats density as a variable and since the equations of motion are non-linear in density, this formulation is not well suited for very viscous flow for which explicit integration is not practical. The iterative

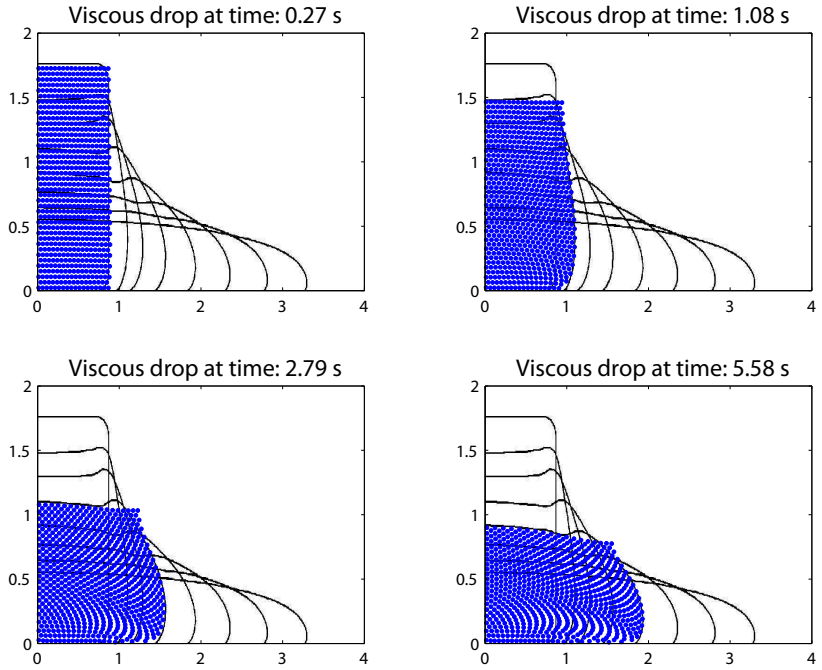

Figure 4.19: The SPH solution of the collapse of a viscous droplet tracks the evolution as predicted by Betelu et al. [4] using the Boundary Element Method. Although the SPH solution arrives at the profiles faster predicted by the BEM solution (profiles correspond to 0, 1, 4, and 8 s in the BEM solution), the SPH solution follows the similarity solution of Huppert [53] once the initial profile decays (see Fig. 4.20).

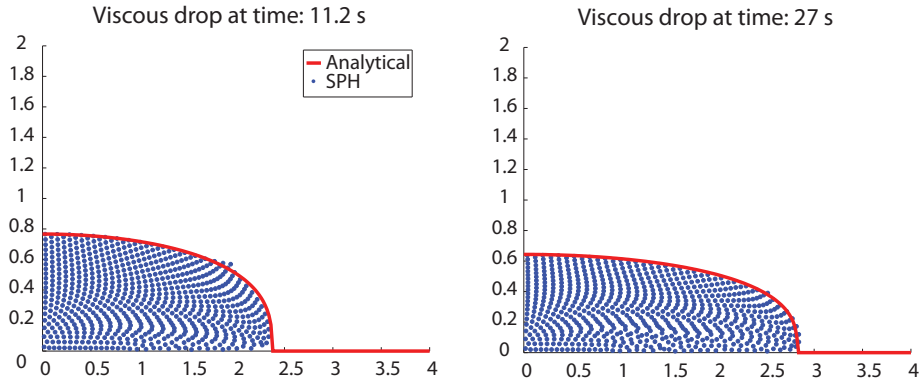

Figure 4.20: Collapse of a viscous droplet at 11 sec (left) and 27 sec (right) (Similarity solution from [53])

.

solvers used for implicit integration rely on a linear relationship of the unknown variables in the equations of motion.

The quasi-compressibility family of perturbations to the divergence-free velocity condition instead treats density as a constant and evolves pressure. This formulation results in a set of equations linear in pressure and velocity and therefore suited for linear iterative solvers. Casting the equations in this form then allows highly viscous fluids to be efficiently modeled by implicit integration. These quasi-compressibility methods include the artificial compressibility method (shown to be similar to the WCSPH formulation), the mixed form of the penalty method (i.e. solving the momentum and continuity equations simultaneously), as well as methods that involve higher-order derivatives of pressure (pressure stabilization and pressure correction). Each of these methods results in a different behavior for the evolution of pressure. It was shown that this evolution behavior for pressure also describes the evolution of $\nabla \cdot \boldsymbol{v}$. We found that combining these methods into hybrid forms can be advantageous. For example, combining the artificial compressibility and penalty methods results in an evolution equation for $\nabla \cdot \boldsymbol{v}$ that is a damped wave equation which is both hyperbolic (lending itself to explicit solvers) as well as damping of the $\nabla \cdot \boldsymbol{v}$ perturbations.

For quasi-static, creeping flows, the hybrid formulation consisting of the stationary, quasi-compressibility forms (penalty and pressure stabilization) performed well for the two test cases; steady-state flow in a lid-driven square cavity, and the collapse of a viscous droplet. The mixed form of the penalty method is greatly improved by including this pressure stabilization term as the penalty method used independently results in an oscillatory pressure solution. Including the $\epsilon_3 \nabla^2 p$ term suppresses these oscillations and leads to faster convergence of the iterative solver and lower errors. A full exploration of $\epsilon_2 - -\epsilon_3$–space for the lid-driven cavity flow case revealed an obvious choice for ϵ_3 that balanced $\nabla \cdot \boldsymbol{v} = 0$ against the spurious oscillatory pressure modes. However, further work is needed to quantify the appropriate choice of ϵ_3 for a given problem.

Although more efficient for creeping flows than WCSPH, convergence can still be slow. This could possibly be improved using preconditioning.

Acknowledgments

Figures 4.1 and 4.5 was generated using SPH visualization software SPLASH [101]

Chapter 5

APPLICATIONS OF SPH TO TECTONIC DEFORMATION

5.1 Introduction

Although elasticity does play a role in the shorter time scales of tectonic deformation, it is less important in the longer time scales. As such, many of the early numerical models [32, 31] of tectonic deformation modeled the crust as a viscous fluid. The use of this simple rheology, has been successful in explaining some of the broad features of mountain belts [33, 31, 10] such as the topography of the Tibetan Plateau [32] and the extension seen in some convergent margins [10, 141].

Deformation in the upper crust, however, is neither viscous nor elastic, but instead the crust behaves as a frictional plastic material. The plastic failure is governed by the Mohr-Coulomb failure criterion [127]. Although on a crustal scale, this deformation is localized on distinct planes of brittle failure, this failure criterion has also been successfully used in critical wedge theory to describe the growth of a prism of sand where the material is at failure everywhere [25]. To model this more diffuse mode of Mohr-Coulomb failure we have implemented a non-linear viscoplastic rheology in our Stokes flow SPH code.

An attractive feature of mesh-free numerical methods is that they can, in principle, accommodate highly localized deformation without the detrimental effects of mesh entanglement suffered by grid-based methods. Moreover, grid-based methods show a mesh sensitivity of failure planes [92] whereas with a mesh-free model, the initiation of these failure planes should, in principle, be less sensitive to the geometry of the underlying stencil [62].

This chapter is organized as follows. In section 5.2 we apply the Stokes flow SPH model to linear viscous models of a doubly-vergent wedge and a symmetric rift. In section 5.3 we outline the Mohr-Coulomb SPH formulation and apply it to the doubly-vergent wedge and the symmetric rift. In section 5.4, we address the issue of strain localization. We outline several improvements, both to the visco-plastic constitutive law and to the numerical implementation, which sharpen the shear bands into more localized failure planes.

5.2 Linear viscous models

The rheologic model we use is that of quasi-static incompressible creeping flow. The equations describing this motion were outlined in chapter 4 and are given by:

$$\begin{aligned} \tfrac{1}{\rho}\boldsymbol{\nabla} p &= \tfrac{1}{\rho}\,\boldsymbol{\nabla}\cdot\Big(\mu\boldsymbol{\nabla}\boldsymbol{v}\Big) + \boldsymbol{g} && \text{Momentum} \\ \boldsymbol{\nabla}\cdot\boldsymbol{v} &= \epsilon_3\Big(\boldsymbol{\nabla}^2 p - \rho\Gamma\Big) - \epsilon_2 p && \text{Continuity} \end{aligned}$$

where Γ results from inhomogeneous material properties and is given by

$$\Gamma = \boldsymbol{\nabla}\cdot\Big[\,\boldsymbol{\nabla}\cdot\Big(\mu\boldsymbol{\nabla}\boldsymbol{v}\Big) + \boldsymbol{\nabla}\rho\cdot\boldsymbol{g}\Big].$$

At each time step, an equilibrium velocity and pressure are determined by solving these equations using an iterative solver. Because the implementation of the boundary conditions, as described in the previous chapter, results in a non-symmetric system of equations, we use the GMRES iterative solver from SPARSKIT [114] with a stopping criterion given by

$$||\text{residual}|| \leq 10^{-8} * ||\text{initial residual}|| + 10^{-11}$$

The particles are then advected according to

$$x^{(n+1)} = x^n + \Delta t\, v^n$$

where v^n is the velocity solution returned by the GMRES solver at the current time step. For particles near boundaries, particularly near stagnation points of the flow, this integration scheme can result in particles being advected across the boundary. To prevent this penetration of the boundary, the time step is reduced until all offending particles plot within the boundaries. Repeatedly offending particles are assumed to have a streamline intersecting a stagnation point and are given a random perturbation to their position.

5.2.1 Wedge cases

The first model geometry is that of a doubly-vergent accretionary wedge as described in [142, 141]. A schematic of the geometry is outlined in Fig. 5.1. A horizontal velocity is imposed on the left side and a zero velocity on the right. The velocity singularity in the middle is referred to as the 'S-point.' Velocity boundary conditions are no-slip, supplemented with the convergence velocity on

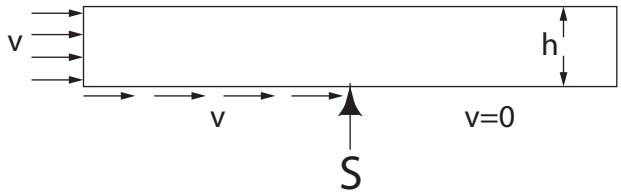

Figure 5.1: Schematic of the doubly-vergent wedge. The S-point is located at the velocity singularity.

the left side of the wedge.

A non-dimensional number that characterizes the viscous response of a mountain to an accretionary flux is the Argand (Ar) number [141] give by:

$$\mathrm{Ar} = \frac{\rho g h^2}{\mu v}$$

This number can be interpreted as the ratio of gravitational stresses to viscous stresses and determines the propensity of a mountain to undergo a gravitational collapse. For high values of Ar, viscous stresses are too weak to sustain orogeny, low values result in higher mountains. For a given model geometry, the Argand number can be scaled by adjusting the convergence rate, v. An example of the SPH solution of the linear viscous wedge case is shown in Fig. 5.2. Time is non-dimensionalized (scaled by $\frac{h}{v}$) and can be interpreted as the number of thicknesses (h) accreted. Particles are shown in orange (shaded according to the square root of the second invariant of the rate of deformation tensor) and velocity vectors drawn in black. A finite element solution (FEM) with an arbitrary Lagrangian-Eulerian (ALE) formulation [141] with this geometry is also shown in Fig. 5.2. The FEM solution solves the equations of Stokes flow without the perturbation to the continuity equation. These equations are solved on an Eulerian grid with a Lagrangian grid advected based on Eulerian velocities [36]. The Lagrangian grid is plotted in Fig. 5.2 with regions of high horizontal strain rate ($\dot{\varepsilon}_{xx}$) shaded (See Fig. 6 of Willett [141]).

In general, the profile and the pattern of deformation of the SPH solution compares favorable with the FEM solution. There are some differences, however, between the models. The SPH solution, for example, shows a greater rate of deformation in the vicinity of the S-point than the FEM solution. The topography of the FEM solution also is slightly higher than the SPH solution. The FEM solution shows the beginning of an overturning of the Lagrangian mesh on the backside of the mountain, a feature not observed in the SPH solution.

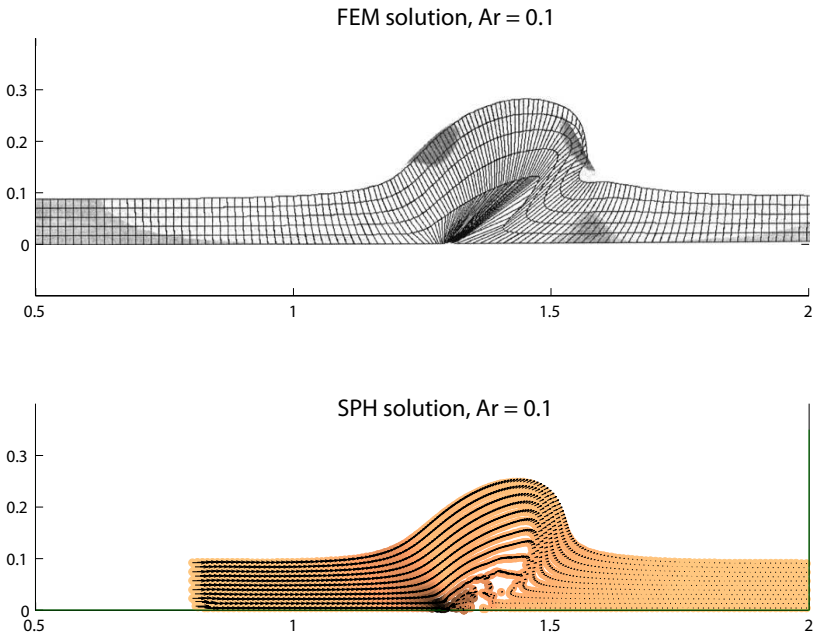

Figure 5.2: Linear viscous (Ar = 0.1) doubly-vergent wedge at non-dimensional time, $t = 5$. The finite element solution of Willett [141] is shown above; the SPH solution is shown below with velocity vectors plotted.

5.2.2 Rift cases

A schematic diagram of the symmetric rift case is shown in Fig. 5.3. The Argand number is not generally used in this case since the viscous stresses contribute to a tensile state of stress. In the convergent case, it is plausible to model the crust as a viscous material and compare gravitational stresses to viscous stresses. In the divergent case, requiring gravitational stresses to overcome tensile viscous stresses is a poor model of geomaterials. However, since non-linear, Mohr-Coulomb model will be based on a viscous model, it is useful to see how linear viscous material behaves in this symmetric rift environment.

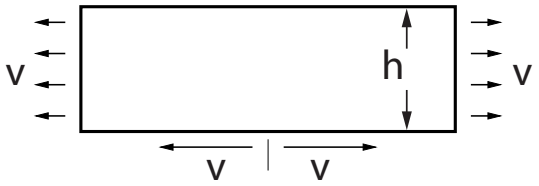

Figure 5.3: Schematic of the symmetric rift.

Results of the linear viscous rift are shown in Fig. 5.4. In this figure and in figures of the results of rift cases that follow, time increases from top to bottom. In general, the column on the left of each of the rift figures will be plots of particles with size corresponding to the characteristic width and colors corresponding to some scalar variable (pressure in the case of Fig. 5.4). The column to the right will be either a velocity vector plot or a tensor plot of the rate of deformation tensor. In the case of Fig. 5.4, both the vector and tensor plots are shown. In the tensor plots, particles are shown as ellipsoids scaled and oriented according to the rate of deformation tensor. The ellipsoids are colored according to the square root of the second invariant of the rate of deformation tensor. The coloring sequence of all of these plots is (from low values to high values) blue, cyan, green, yellow, red.

The effect of the no-slip boundary condition can be seen from the progressive necking of the fluid. The divergent velocity singularity initiates a tear. The bulk of the deformation occurs near the S-point as can be seen by large values (size of glyphs and warm colors) in the tensor plot of the rate of deformation tensor. Continued deformation results in the fluid separating into two blobs.

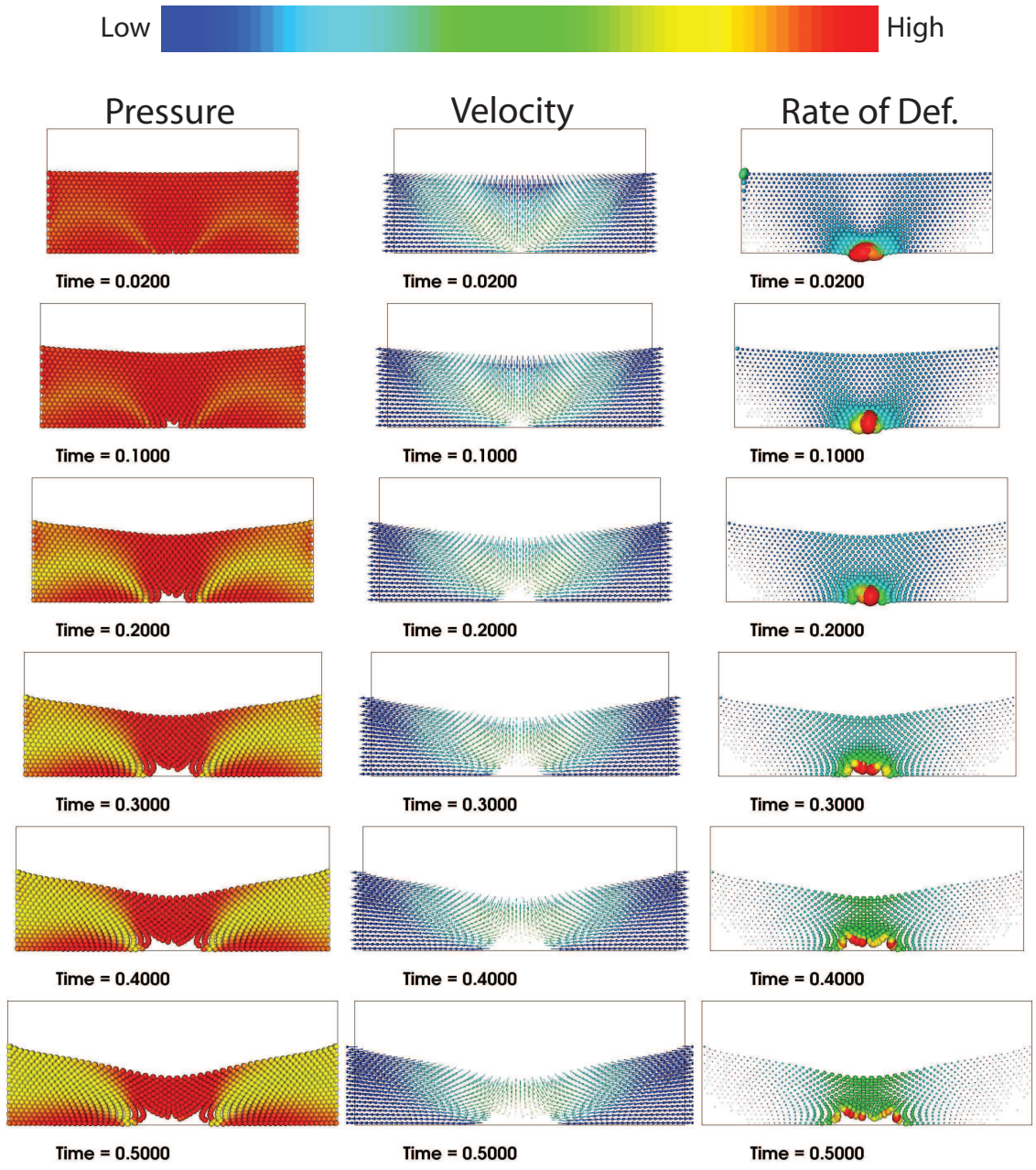

Figure 5.4: Linear viscous ($\mu = 10^4\,\mathrm{Pa\,s}$) rift. Pressure is plotted in the left column (warm colors correspond to higher values) and velocity vectors are plotted in the middle column. In the right column, the rate of deformation tensor is plotted, scaled by the eigenvalues and colored by the square root of the second invariant.

5.3 Non-linear viscous models

5.3.1 Algorithm

Plasticity is incorporated into our model using a non-linear effective viscosity given by $\mu_p = \frac{\sigma^Y}{2\sqrt{I_2'}}$ where I_2' is the second invariant of the deviatoric rate of deformation tensor given by

$$I_2' = \frac{1}{2}\mathbf{D}_{ij}\mathbf{D}_{ij}$$

σ^Y is the yield stress. For a Mohr-Coulomb material in 2-D, the yield stress is given by

$$\sigma^Y = C\cos\phi + p\sin\phi \tag{5.1}$$

where C is the cohesion and ϕ is the internal angle of friction [141]. The equation for material in 3-D is slightly more involved (see Eq. 19 of Willett [140] or Eq. 6.3.23 of Vardoulakis and Sulem [134] for three-dimensional varieties.), however since all the simulations that follow are 2-D, we use Eq. 5.1. This model does not include a temperature dependent viscosity.

A similar SPH implementation of the Mohr-Coulomb rheology using this non-linear plastic viscosity was used in modeling the dynamics of ice-floes [45, 44, 46, 94, 121]. These studies differ from the present implementation in that the equations were integrated explicitly. Small time-steps were used (due to the large viscosity) so plastic viscosities did not need to be equilibrated with the velocity and pressure fields at a given time-step.

The calculations proceed as follows. At the start of the simulation, the material is initialized to a high viscosity. The equilibrium velocity and pressure for the imposed boundary conditions is calculated. From the new pressure and velocity field, $\mathbf{D}_{ij}$, σ^Y and μ_p are calculated. If the new μ_p is less than the initialized value, the viscosity is reassigned to the new μ_p and a new velocity and pressure field are calculated. The iterations proceed until the relative error of the velocity solution is less than 10^{-6}.

5.3.2 Numerical Tests

Angle of Repose

To test this implementation of Mohr-Coulomb plasticity in our SPH model, we use the dam break test. In this case, the initial square of Mohr-Coulomb material should collapse and come to rest in a pile with an angle of repose. This angle of repose is an approximate measure of the internal angle of friction (ϕ) [59, 95].

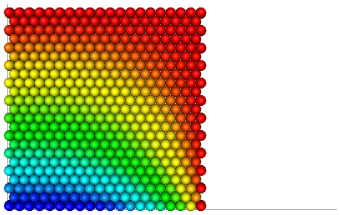

Figure 5.5: Mohr-Coulomb Dam Break – Initial configuration. Colors correspond to pressure.

The initial configuration is shown in Fig. 5.5 and consists of a square of material against a wall. Two simulations were run with material with internal angles of friction of $\phi = 30°$ and $\phi = 60°$. Results are shown in Fig. 5.6. Again, the colors correspond to pressure. The angle of repose increases with increasing internal angle of friction, as expected. However it differs slightly from the imposed internal angle of friction (36° for $\phi = 30°$ and 57° for $\phi = 60°$). Aside from this slight discrepancy, this visco-plastic SPH formulation simulates Mohr-Coulomb material as expected.

Figure 5.6: Mohr-Coulomb Dam Break – Shown on the left, $\phi = 30°$ (The actual angle of repose is approximately 36°), On the right, $\phi = 60°$ (The actual angle of repose is approximately 57°)

Wedge

Using the Mohr-Coulomb rheology with the doubly-vergent wedge boundary conditions, leads to the a broad zone of plastic deformation near the S-point. This zone of plastic deformation can be seen in the left column of Fig. 5.7 where the colors correspond to plastic viscosity (cooler colors are lower viscosities). After a short amount of convergence, deformation bands form in the expected locations. Fig. 5.7 shows the deformation bands in both the pro- and retro-wedge. The deformation bands, however, are fairly diffuse. As can be seen in the last time step of plastic viscosity plot of Fig. 5.7,

a triangular block is being uplifted. From the velocity plot in the right column, the orientation of uplift is along the retro-wedge shear zone.

Rift

Applying this rheology to the rift geometry also generates two prominent shear zones as can be seen in Fig. 5.8. In this case (Case 1), a quintic spline kernel was used with $h = 1.2$ as is typically used for viscous flow problems. Although the velocity vectors in Fig. 5.8a indicate that the central block descends fairly uniformly, the plot of plastic viscosity (left column of Fig. 5.8b) indicates that the entire central region is experiencing plastic failure. This plastic failure zone broadens with increasing deformation, however there is some flux of material across the deformation zones. The material in this case has no history dependence so it might be expected that the deformation bands would be located primarily by the geometry. This would lead to a material flux across the 'failure plane' as the material is deformed across the shear zone. The localization of deformation can most easily be seen in the right column of Fig. 5.3.2b where the rate of deformation tensor is plotted, scaled according to the eigenvalues of the tensor and colored according to its second invariant. The larger the glyphs, the more intense the deformation.

Figures 5.9 and 5.10 show the same rheology and geometry modeled with two other numerical methods, the finite element (FEM) and distinct element (DEM) methods. The finite element case was run by Chris Fuller [118] using a variant of the ALE software shown in Fig. 5.2. In this plot, the color scheme is reversed so that blue corresponds to no plastic deformation and red to low plastic viscosity. The plastic viscosity for the FEM solution shows a similar shear banding as was seen in the SPH model. In the SPH model, however, the descending triangular block was also undergoing plastic deformation although not as severely as in the shear zones.

The distinct element method (DEM) is another Lagrangian particle numerical method for simulating Mohr-Coulomb material. The method was originally described by Cundall and Strack [24] and consists of simulating individual grains interacting with each other through frictional contact forces. The simplest formulation for these grains is radially symmetric grains which exert normal forces on neighboring grains in proportion to the amount of overlap of the particles. Shear forces are limited by this normal force through a frictional constant. In a sense, this method can be thought of as the numerical equivalent of a sandbox experiment. This method has been widely used for modeling the behavior of granular material, material which often exhibits behavior not readily approximated with continuum equations (grain bridging, grain-size sorting [29]). Because the formulation is designed for grains interacting through frictional forces, and because sandbox experiments have been

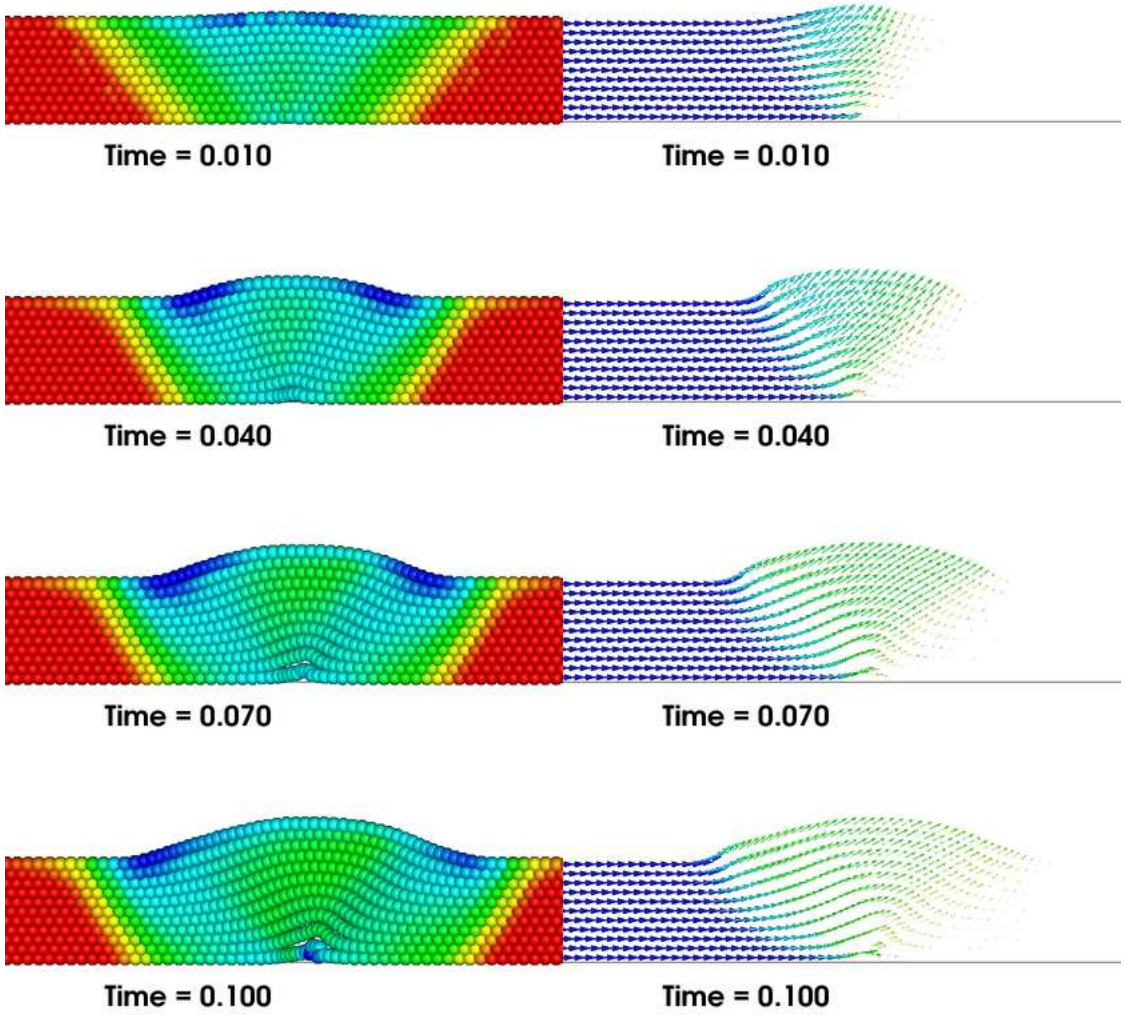

Figure 5.7: Mohr-Coulomb Wedge: The left column shows log of plastic viscosity ($\log_{10} \mu_p$) where red corresponds to high viscosity (no plastic deformation) and blue to low. Velocity vectors are plotted on the right.

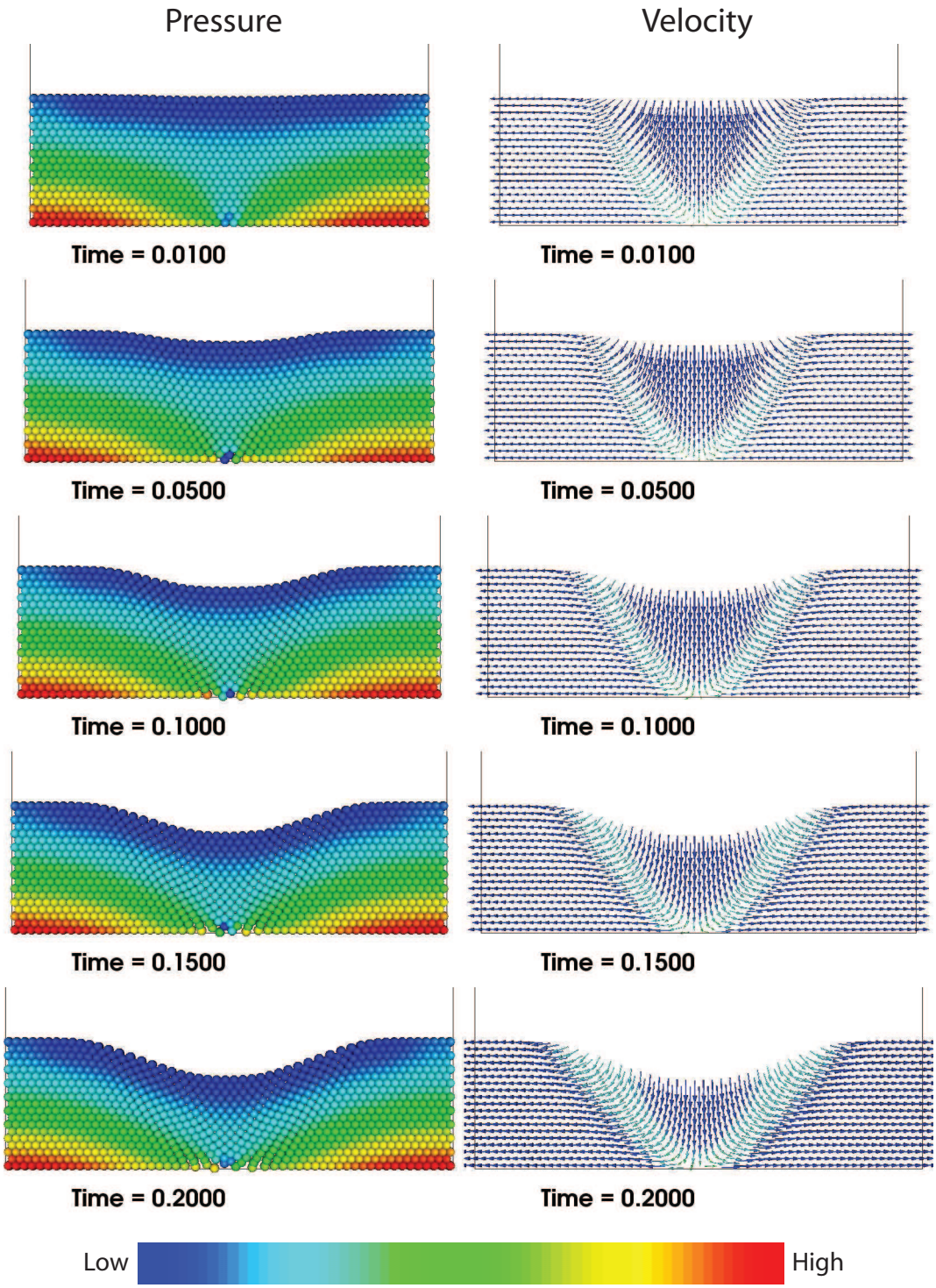

Figure 5.8a: CASE 1: Mohr-Coulomb Rift, (Quintic Spline kernel, $h = 1.2$). Pressure is plotted in the left column (warm colors correspond to higher values) and velocity vectors are plotted in the right column.

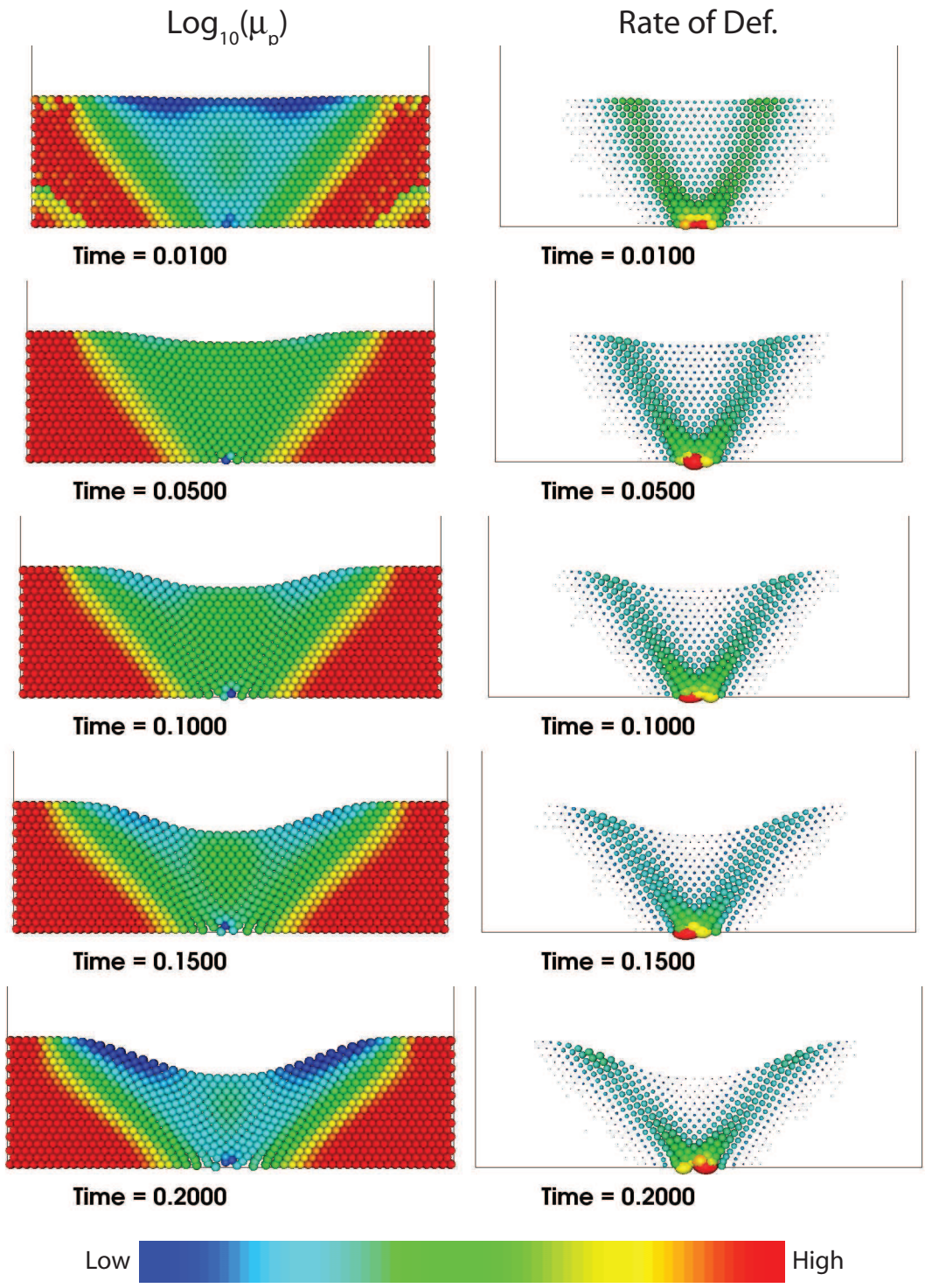

Figure 5.8b: CASE 1: Mohr-Coulomb Rift, (Quintic Spline kernel, $h = 1.2$). $\log_{10} \mu_p$ is plotted in the left column. In the right column, the rate of deformation tensor is plotted, scaled by the eigenvalues and colored by the square root of the second invariant.

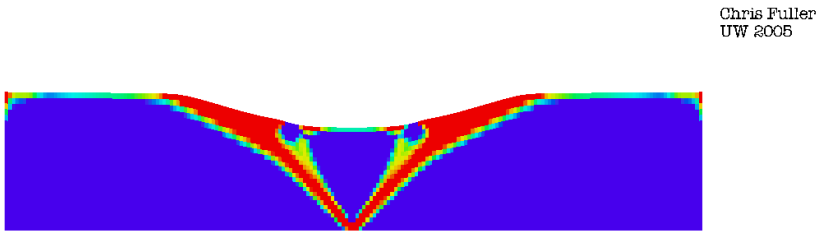

Figure 5.9: Mohr-Coulomb rift: Finite Element Method (FEM) solution, colors correspond to plastic viscosity.

successful in capturing deformation behavior seen on the crustal scale [116], DEM simulations have been extrapolated to crustal-scale processes [12, 126, 13, 135, 34, 119, 91, 144]. In this extrapolation, 'grains' are ten's of meters across. However, deformation patterns can show similarities to features of deformation observed in crustal deformation, as for example, highly localized shear zones (faults) [13].

The results of the DEM model shown in Fig. 5.10 were generated with a subroutine of our particle code that stemmed from software written by Mark Naylor. Naylor has found that grains can be prone to over-rotation unless their angularity is increased such as by considering rigid clusters of grains [91]. In the model shown, grain clusters were not used, only circular grains of non-uniform radius. Cohesion can be included, however it is not included in the model shown, as it was not used either in the SPH or the FEM model. The instantaneous deformation field is not as easy to visualize, however, the elements in Fig. 5.10 are colored according to their initial height which allows the cumulative deformation to be seen.

The resulting topography generated by the three numerical methods are summarized in Fig. 5.11. The DEM model results in a very irregular topography while the SPH and FEM models both generate similar topographies.

Although Fig. 5.10 does not show predominant deformation through faulting (that may be a function of cohesion), DEM is popular because it can exhibit highly localized shear deformation. This is due primarily to the short radius of influence of the neighboring grains. Either grains are in contact, in which case there is an inter-particle force, or they are not in contact, in which case there is no force. In SPH, in contrast, the influence of neighboring particles is much broader, as can be seen in Fig. 5.12, thereby setting a lower limit on the thickness of shear bands.

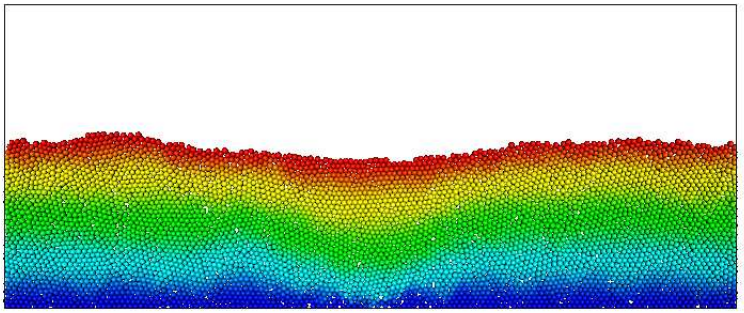

Figure 5.10: Mohr-Coulomb rift: Distinct Element Method (DEM) solution, colors correspond to initial height.

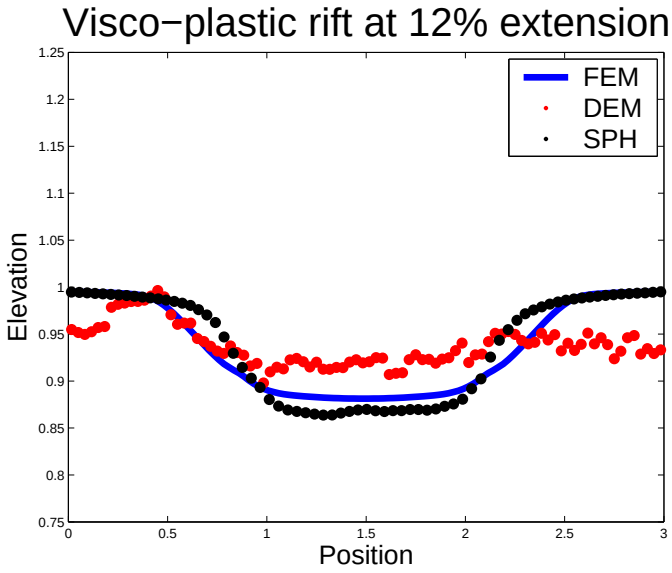

Figure 5.11: Mohr-Coulomb rift: Comparison with finite-element and distinct element models.

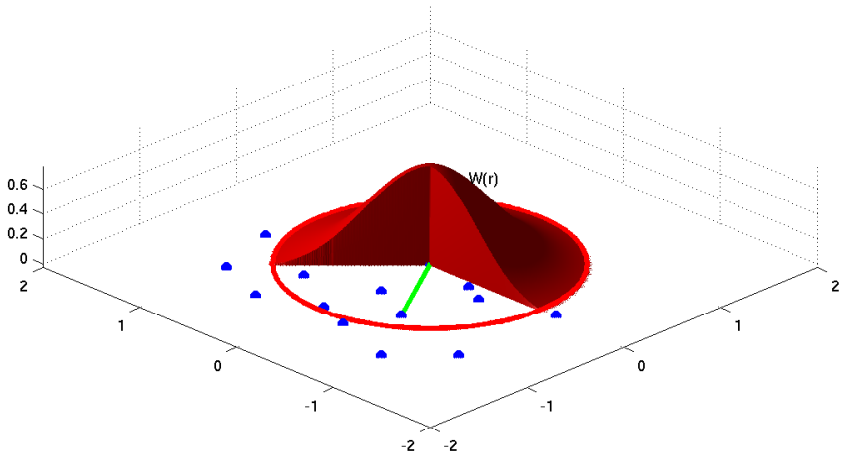

Figure 5.12: Schematic of SPH kernel.

For the remainder of this chapter, modifications to Case 1 will be implemented in order to improve the localization of strain. The next ten cases will include these various modifications and are tabulated in Table 5.1 at the end of section 5.4 on page 125.

5.4 Improvements on non-linear model

In both the doubly-vergent wedge and symmetric rift cases, deformation was partially localized in diffuse shear bands. The hope in using a mesh-free numerical method is to be able to accommodate highly localized deformation, as in brittle deformation along faults, without requiring the regridding necessary with a highly deformed mesh and without suspicions of a mesh dependency on fault initiation. As mentioned in the previous section, DEM has been fairly successful in this endeavor, however the inter-particle contact force formulation makes it difficult to specify behavior more appropriately modeled as a continuum, such as viscous deformation. The SPH approach solves the continuum equations, but the shear bands in neither the convergent nor the divergent cases were localized.

As suggested above, the success of the DEM formulation is due, in part, to the limited range of influence of the neighboring particles. In sections 5.4.1 and 5.4.2, the focus will be on methods of accurately reducing the region of influence of the smoothing kernel. The hope is that there will be a corresponding reduction in the width of the shear bands. The most obvious approaches are to directly decrease the smoothing length (h) or to decrease the order of the smoothing kernel. These are investigated in sections 5.4.2 and 5.4.2. Accuracy, however, will decrease with fewer neighboring particles. Before testing the accuracy of smaller kernels, it is worth applying the same techniques

for correcting the Laplacian of scalar fields as developed in chapter 3 to the Laplacian of $\boldsymbol{v}$. This will compensate for the reduction in accuracy in shrinking the kernel width. This correction term for $\nabla^2\boldsymbol{v}$ is developed and investigated in section 5.4.1

An alternate method of reducing the width of a kernel is to employ some means of adaptively refining the resolution of the problem by splitting particles in regions of large deformation gradients. This is discussed in section 5.4.3.

Finally, in section 5.4.4, the constitutive law is modified to include strain-softening.

5.4.1 Corrected Viscous Term

In chapter 3, a correction term was derived that improves the accuracy of the Brookshaw discretization of the Laplacian of a scalar function f, given by:

$$\begin{aligned}\left\langle \boldsymbol{\nabla}\cdot\left(\tau\boldsymbol{\nabla}f(x_i)\right)\right\rangle &\simeq \frac{\boldsymbol{\Gamma}^{-1}_{\beta\beta}}{n}\left\{\sum_j \varphi_j\left(\tau_j+\tau_i\right)\left(f(x_j)-f(x_i)\right)\frac{\left(x_{ij}\right)_\alpha W_{,\alpha}}{|x_{ij}|^2}\right.\\ &\left.-\left[\left(\tau_i f(x_i)\right)_{,\alpha}-f(x_i)\tau_{i,\alpha}+\tau_i f_{,\alpha}(x_i)\right]\cdot\left[\sum_j \varphi_j W_{,\alpha}\right]\right\} \qquad (5.2)\end{aligned}$$

in which the Latin subscripts refer to particles, Greek subscripts to coordinates, and

$$\boldsymbol{\Gamma}_{\beta\gamma} = \int_\Omega \frac{\left(\Delta x\right)_\alpha W_{,\alpha}}{|\Delta x|^2}\left(\Delta x\right)_\beta\left(\Delta x\right)_\gamma \,\mathrm{d}x \qquad (5.3)$$

This correction can also be applied to the Laplacian of a vector function such as the viscous term of Eq. 5.2 where $\tau \to \mu$ and $f \to \boldsymbol{v}$.

$$\begin{aligned}\left\langle \boldsymbol{\nabla}\cdot\left(\mu\boldsymbol{\nabla}\boldsymbol{v}_\alpha(x_i)\right)\right\rangle &\simeq \frac{\boldsymbol{\Gamma}^{-1}_{\gamma\gamma}}{n}\left\{\sum_j \varphi_j\left(\mu_j+\mu_i\right)\left(\boldsymbol{v}_\alpha(x_j)-\boldsymbol{v}_\alpha(x_i)\right)\frac{\left(x_{ij}\right)_\beta W_{,\beta}}{|x_{ij}|^2}\right.\\ &\left.-\left[\left(\mu_i\boldsymbol{v}_\alpha(x_i)\right)_{,\beta}-\boldsymbol{v}_{\boldsymbol{\alpha}}(x_i)\mu_{i,\beta}+\mu_i\boldsymbol{v}_{\alpha,\beta}(x_i)\right]\cdot\left[\sum_j \varphi_j W_{,\beta}\right]\right\} \qquad (5.4)\end{aligned}$$

In Eq. 5.4, the Γ-term is the same as given in Eq. 5.3. This is fortunate since generating the correction coefficient ($\frac{\boldsymbol{\Gamma}^{-1}_{\gamma\gamma}}{n}$) is expensive both in terms of computation, as it requires inverting a matrix, and in storage. The free-surface, viscous flow test cases of chapter 4 were quite successful without this correction term, however the hope is that the use of this correction will mitigate the decrease in accuracy associated with decreasing the width of the stencil.

As in chapter 3, this correction can be considered in two steps: the additive correction term

associated with the gradients of μ and $\boldsymbol{v}$, and the multiplicative term associated with the Γ-matrix. As noted in chapter 3, this scaling term should be approximately unity in regions of full kernel support, but will become significant in the vicinity of free-surfaces. A plot of the magnitude of this scaling term over a unit patch ($2 < x < 3$, $2 < y < 3$) is shown in Fig. 5.13. This figure shows that the scaling factor indeed differs significantly from unity near the edges of the patch.

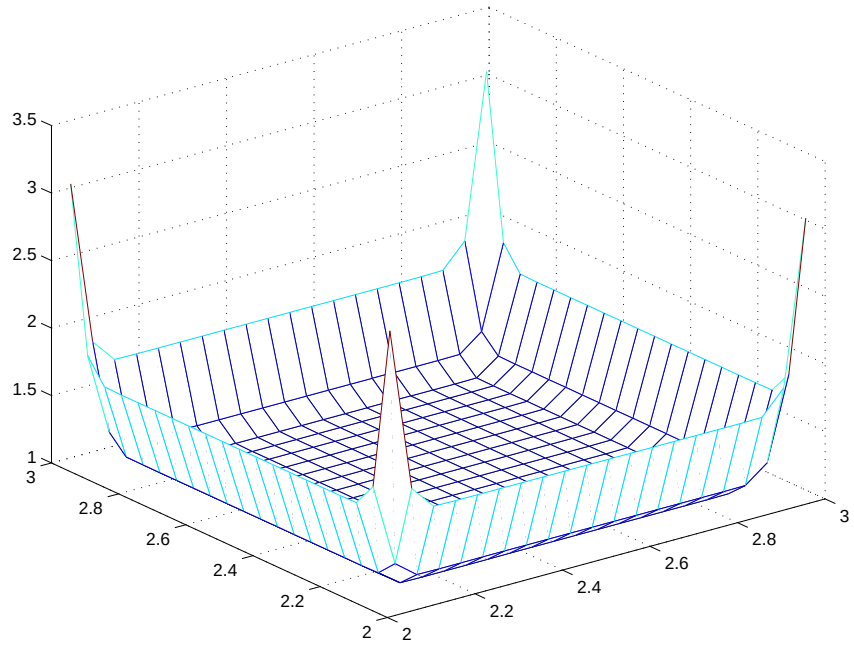

Figure 5.13: Correction factor Γ_{ii}/n over a unit patch.

To test the efficacy of each correction step, the function $\boldsymbol{v} = (x^2 + y^2)\hat{\boldsymbol{i}} + (x^2 + y^2)\hat{\boldsymbol{j}}$ was used to test the three Laplacian discretizations: the Brookshaw form due to Morris et al. [89] (which we refer to as L1), the two-term form without the Γ-scaling factor but with gradients calculated using the CSPH formulation (L2), and the two-term form with the scaling factor as given in Eq. 5.4 (L1-Γ). The true solution is $\boldsymbol{\nabla^2 v} = 4\hat{\boldsymbol{i}} + 4\hat{\boldsymbol{j}}$. In Fig. 5.14, the relative error at each point, given by

$$\text{Relative Error} = \sqrt{\frac{(\nabla^2 \boldsymbol{v}_0 - \nabla^2 \boldsymbol{v}) \cdot (\nabla^2 \boldsymbol{v}_0 - \nabla^2 \boldsymbol{v})}{\nabla^2 \boldsymbol{v}_0 \cdot \nabla^2 \boldsymbol{v}_0}} \tag{5.5}$$

is plotted for the three discretizations on a unit patch of equally-spaced particles. It can be seen that the L2 form performs significantly better than the L1 form near the boundaries. The L2-Γ form to within machine-ϵ for this quadratic test function on a regular array of particles.

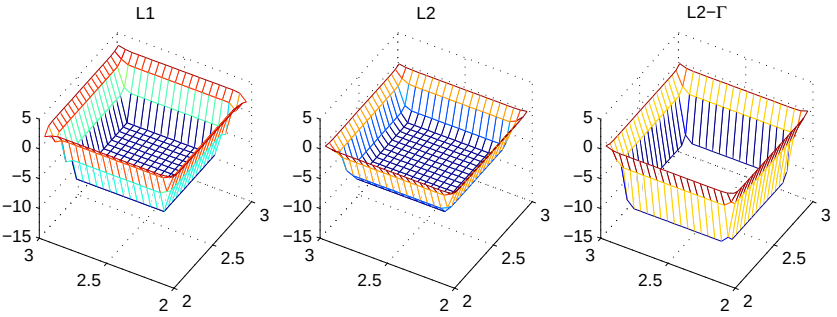

Figure 5.14: Correcting $\nabla^2 \boldsymbol{v}$ where $\boldsymbol{v} = (x^2+y^2)\hat{\boldsymbol{i}}+(x^2+y^2)\hat{\boldsymbol{j}}$ over an ordered array of particles. The left figure shows the log of the relative error in $\nabla^2 \boldsymbol{v}$ with no correction. The middle figure show the effect by including the unscaled second term. The plot on the right shows the effect including the second term scaled by Γ_{ii}/n.

To test the performance of these correction terms for a disordered array of particles, each particle of the regular array was given a random perturbation. This disordered unit patch is the same that was used in section 3.2.4 of chapter 3. Results are shown in Fig. 5.15. The performance of each discretization is hampered by the disorder of the particles, however the same trend can be seen where the L2 form reduces the error by a couple orders of magnitude over just the L1 form. The L2-Γ form results in a further reduction in relative error.

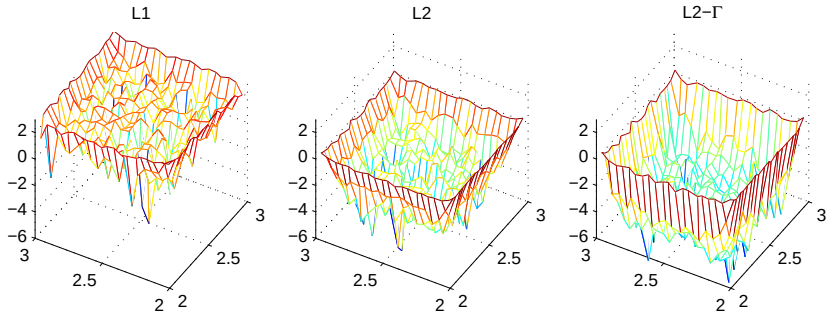

Figure 5.15: Correcting $\nabla^2 \boldsymbol{v}$ where $\boldsymbol{v} = (x^2 + y^2)\hat{\boldsymbol{i}} + (x^2 + y^2)\hat{\boldsymbol{j}}$ over an disordered array of particles. The left figure shows the log of the relative error in $\nabla^2 \boldsymbol{v}$ with no correction. The middle figure show the effect by including the unscaled second term. The plot on the right shows the effect including the second term scaled by Γ_{ii}/n.

As noted above, the motivation for this extra effort is to hopefully retain a level of accuracy while reducing the width of the support domain. The reduction in the kernel width should allow

for more localized deformation by reducing the depth of influence of viscous effects across shear bands. Using a cubic spline kernel and a slightly shorter characteristic width of $h = 1.0$ (the effects of these modifications is investigated in the sections 5.4.2 and 5.4.2), the two corrected Laplacian discretizations (L2 and L2-Γ) were applied to the symmetric rift case. Results of the velocity solution are shown in Fig. 5.16

As can be seen in Fig. 5.16, the velocity solution is not stable with deviations from the expected values most pronounced near the surface. It is not clear why this discretization which more accurately calculates the Laplacian results in a less stable velocity solution returned by the iterative solver. In the test cases of chapter 3, the Laplacian was not actually employed at the surface. The surface particles were treated as boundary particles and were not required to satisfy the differential equation (containing the Laplacian term), only the boundary condition. For the viscous flow cases, a velocity boundary condition is not imposed at the surface. The stress-free condition at the surface can be approximated by setting $p = 0$, however using the stationary hybrid perturbation to the continuity equation results in negligible pressure values at the surface (See the left column of Fig. 5.8a). This lack of enforcement of velocity boundary conditions at the surface is likely the cause of this instability. Velocity of the surface particles could be coupled to the stress-free boundary condition by requiring that the vector equation $\boldsymbol{\sigma} \cdot \boldsymbol{n} = \mathbf{0}$ (where $\boldsymbol{n}$ is the unit normal to the surface) is satisfied instead of assigning $p = 0$.

Because of the velocity instability in the converged solution, the L2 and L2–Γ correction terms will not be used in rift cases presented later in this chapter. The strictly stress-free boundary has not been implemented, but could be at a later time. Therefore the behavior of these corrections will be included in the next section on the effects of reducing the kernel width.

5.4.2 Minimizing the smoothing effect of the kernel

Reduce the characteristic width, h

Higher order kernels such as the quintic spline kernel are normally used in the discretization of Laplacian terms since it has smoother derivatives than the lower-order kernels.

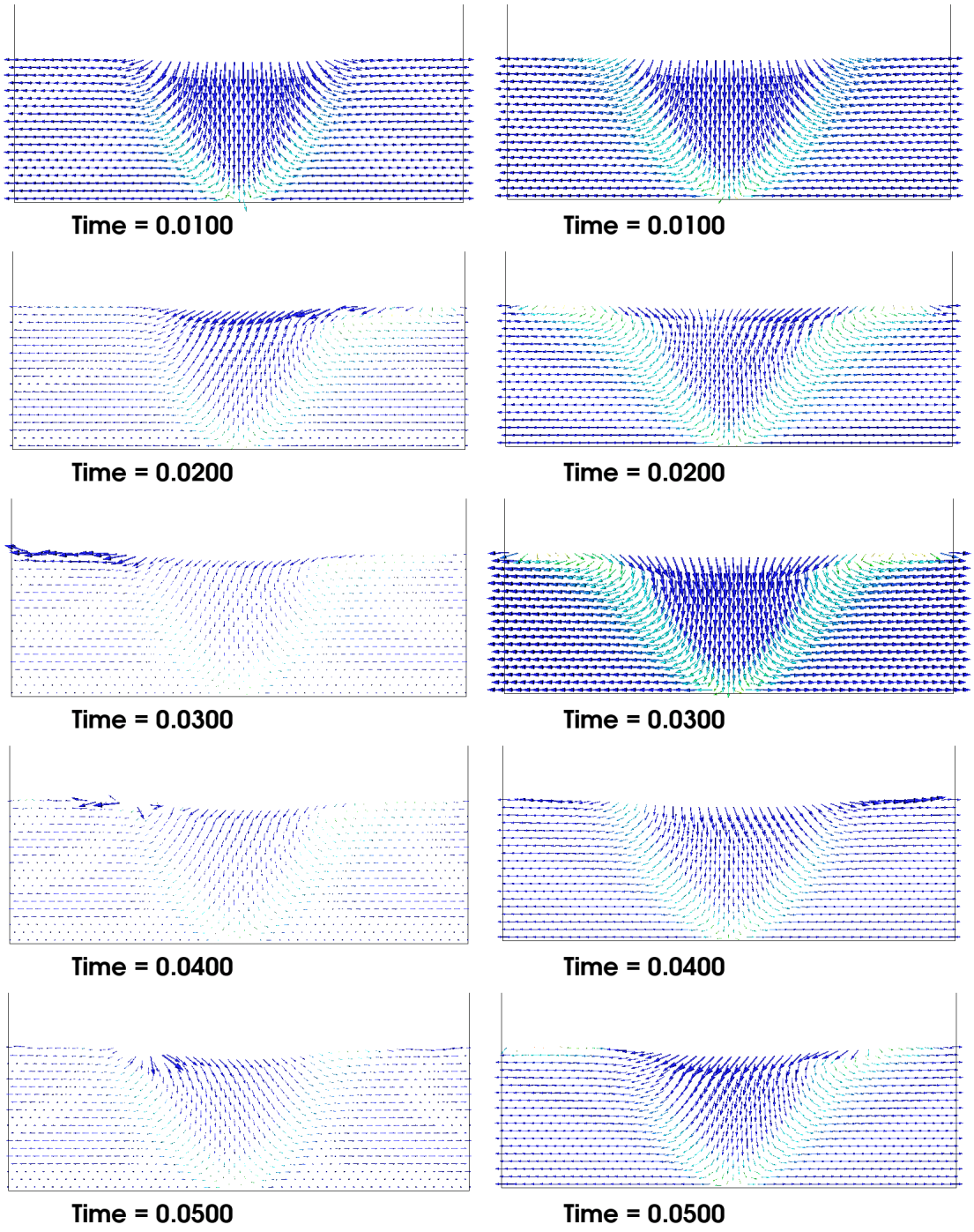

Figure 5.16: CASE 2 and 3: Mohr-Coulomb Rift, (Cubic Spline kernel, $h = 1.0$, Two-term Laplacian (Case 2) and with Γ correction (Case 3)). Velocity vectors for Cases 2 and 3 are plotted in the left and right columns, respectively.

The quintic spline kernel commonly used in viscous flow calculations is given by:

$$W(s) = \frac{w_0}{h^n}\begin{cases} (3-s)^5 - 6(2-s)^5 + 15(1-s)^5 & : \quad 0 \le s < 1 \\ (3-s)^5 - 6(2-s)^5 & : \quad 1 \le s < 2 \\ (3-s)^5 & : \quad 2 \le s < 3 \\ 0 & : \quad s > 3 \end{cases}$$

$$\boldsymbol{\nabla} W(s) = \frac{w_0}{h^{n+1}}\begin{cases} -5\left[(3-s)^4 - 6(2-s)^4 + 15(1-s)^4\right]\hat{\boldsymbol{r}} & : \quad 0 \le s < 1 \\ -5\left[(3-s)^4 - 6(2-s)^4\right]\hat{\boldsymbol{r}} & : \quad 1 \le s < 2 \\ -5\left[(3-s)^4\right]\hat{\boldsymbol{r}} & : \quad 2 \le s < 3 \\ 0 & : \quad s > 3 \end{cases}$$

$$w_0 = \frac{1}{120}, -\frac{7}{478\pi}, -\frac{3}{359\pi} \text{ for } 1, 2, 3\text{D}$$

where h is the adjustable smoothing length. We have found good results for thermal diffusion and viscous flow calculations if we choose $h = 1.2$. If h is decreased, there is a corresponding decrease in the number of neighbors contributing to the integral approximation, however this also leads to a decrease in the range of influence of the viscous effects.

To test how the various Laplacian discretizations perform when the kernel width is reduced, the relative error for the three discretizations are plotted as the kernel width varied from 0.6 to 1.2 in 0.05-step increments. The disordered patch was used and all particles in the subdomain $2.25 < x < 2.75$, $2.25 < y < 2.75$ were considered in order to neglect particles with truncated support as happens near surfaces. The particles were assigned a velocity value according to $\boldsymbol{v} = (x^2 + y^2)\hat{\boldsymbol{i}} + (x^2 + y^2)\hat{\boldsymbol{j}}$. Because of the disorder, each particle had a different number of neighbors, a number which decreased as the characteristic width decreased. To quantify the average performance of the discretizations as a function of the number of neighbors in the support domain, the errors for all particles in the subdomain for each value of h are plotted in the same figure. Results are shown in Fig. 5.17. The log of the average relative error as a function of the number of neighbors, is plotted as the solid lines (Brookshaw (L1) in black, L2 in red, and L2-Γ in blue). As expected, the discretizations all improve with increasing number of neighbors with the corrected versions of the Laplacian outperforming the Brookshaw form.

Figure 5.18 shows the probability distribution of the number of neighbors a particle will have for the quintic spline kernel of different characteristic widths. This is useful since we can see from Fig. 5.17 that for the quintic spline kernel, the solution does not improve much once a particle has at least 25 neighbors. Fig. 5.18 then suggests that 25 neighbors can be reliably achieved by using a

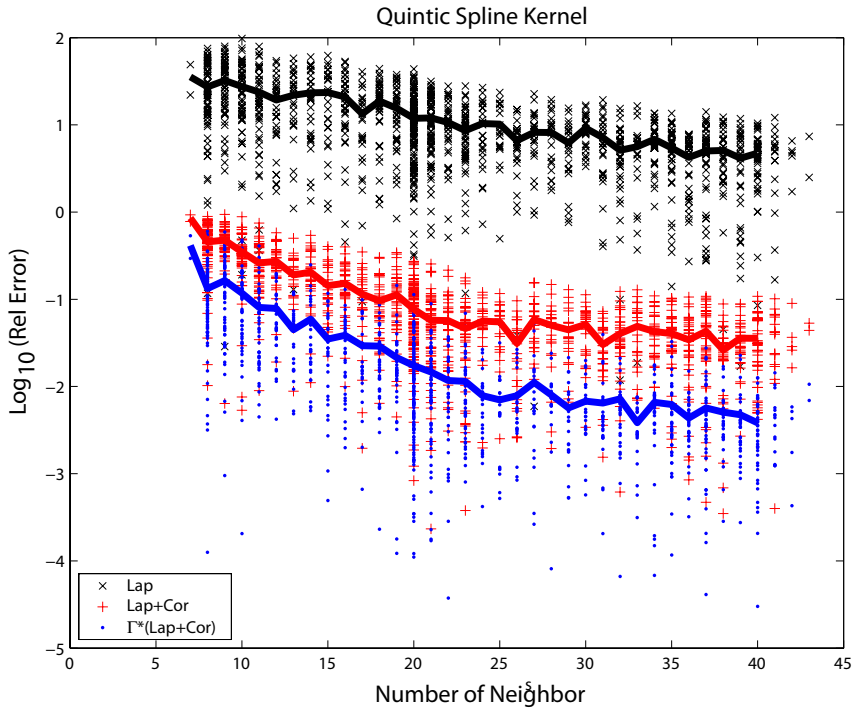

Figure 5.17: Dependence of the relative error of the estimate of $\nabla^2 \boldsymbol{v}$ on the number of neighbors for the quintic spline kernel.

characteristic width of $h = 1.0$.

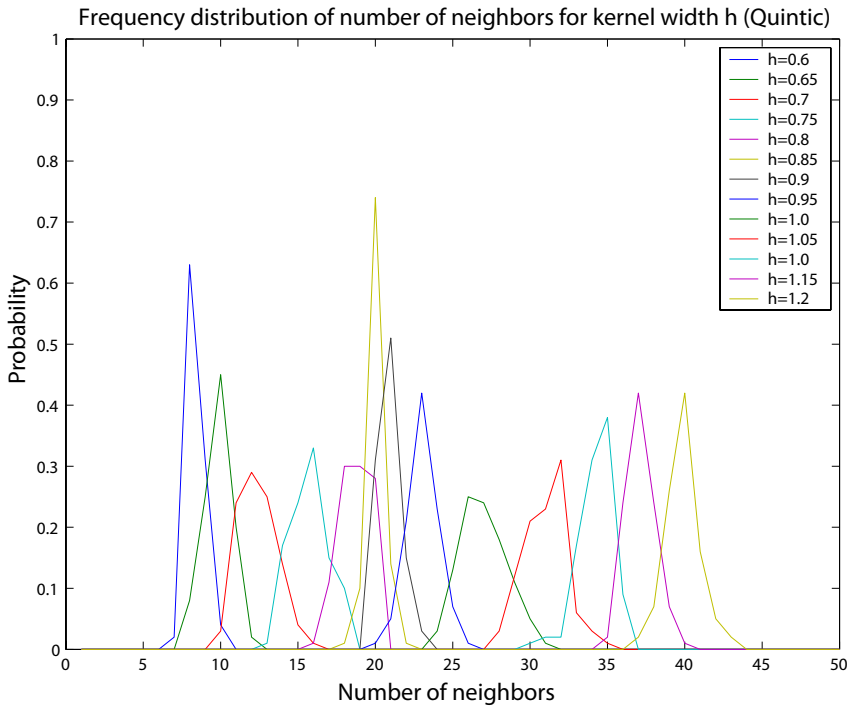

Figure 5.18: Probability distribution of the number of neighbors for the quintic spline kernel with $h = 0.6$–1.2.

Reduce order of smoothing kernel

From the equations for the quintic spline kernel, we see that the range of influence of that kernel is $3h$. Lower order kernels, such as the cubic spline kernel, has a stencil width of only $2h$. Various commonly-used kernels are plotted in Fig. 5.19. First and second derivatives are plotted in Fig.s 5.20 and 5.21. Although the cubic spline kernel is more frequently seen in the literature for general SPH problems, the quintic spline kernel is often used for diffusive problems since the second derivative is smoother than that of the cubic spline kernel.

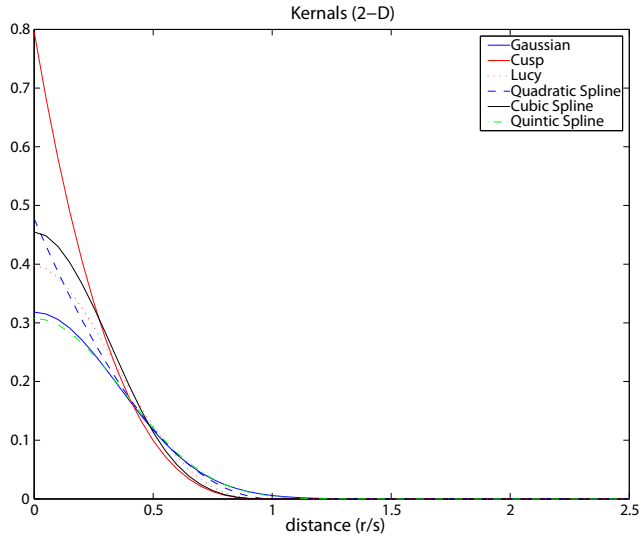

Figure 5.19: Commonly-used smoothing kernels.

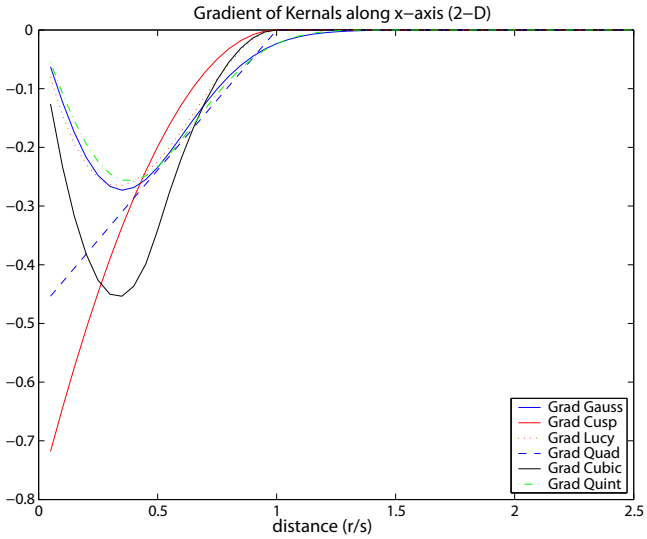

Figure 5.20: First derivatives of the commonly-used smoothing kernels.

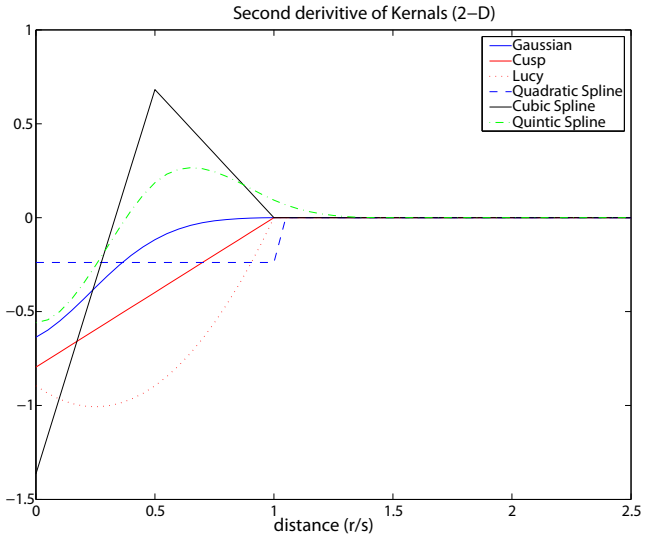

Figure 5.21: Second derivatives of the commonly-used smoothing kernels.

The equations for the cubic spline kernel are given below.

$$W(s) = \frac{w_0}{h^n}\begin{cases} 1-\frac{3}{2}s^2+\frac{3}{4}s^3 & : \quad 0 \le s < 1 \\ \frac{1}{4}(2-s)^3 & : \quad 1 \le s < 2 \\ 0 & : \quad s > 1 \end{cases}$$

$$\boldsymbol{\nabla} W(s) = \frac{w_0}{h^{n+1}}\begin{cases} -3s-\frac{1}{4}s^2\,\hat{\boldsymbol{r}} & : \quad 0 \le s < 1 \\ -\frac{3}{4}(2-s)^2\,\hat{\boldsymbol{r}} & : \quad 1 \le s < 2 \\ 0 & : \quad s > 2 \end{cases}$$

$$w_0 = \frac{2}{3}, -\frac{10}{7\pi}, \frac{1}{\pi} \text{ for } 1, 2, 3-\text{D}$$

To test the performance of this kernel in calculating the various Laplacian discretizations, the same tests were run as for the quintic spline kernel with h spanning the range $0.6 \rightarrow 1.2$. As can be seen in Fig. 5.22, accurate results can be obtained with the cubic spline kernel with far fewer neighbors than required for the quintic spline kernel, despite the particle disorder. As in Fig. 5.17, the log of the average relative error as a function of the number of neighbors is plotted as the solid lines (Brookshaw (L1) in black, L2 in red, and L2-Γ in blue). As expected, the corrected forms of the Laplacian outperform the Brookshaw form. The sharp increase in error for both corrected forms for particles with 5 or fewer neighbors is a result of restrictions on matrix inversions for Γ and $\mathbf{C}$.

Fewer than 6 neighbors can result in ill-posed matrices which lead to spurious accelerations when inverted. Essentially, for particles with very few neighbors, both the L2 and L2-Γ forms are the unscaled two-term correction with the gradients calculated with no gradient corrections.

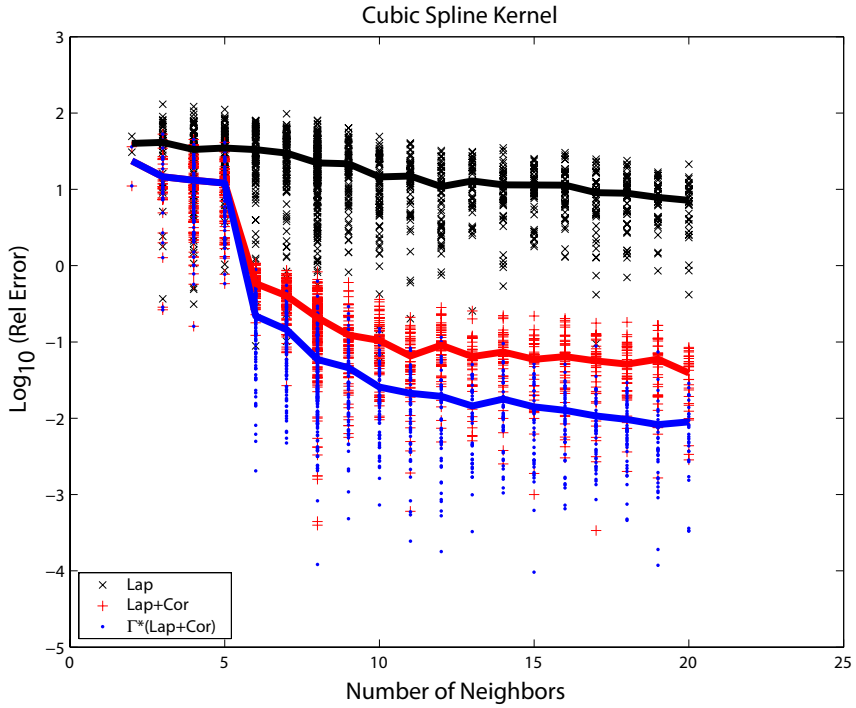

Figure 5.22: Dependence of the relative error of the estimate of $\nabla^2 \boldsymbol{v}$ on the number of neighbors for the cubic spline kernel.

The probability distribution of the number of neighbors as a function of the characteristic width is plotted in Fig. 5.23. From Fig. 5.22, it can be seen that the error is not significantly reduced after a particle has at least 10 neighbors. Fig. 5.23 then shows that this can be achieved using a characteristic width of $h = 1.0$.

Application of narrower kernel to the symmetric rift

To test the effect of using this lower order kernel, a case (Case 4) was run for the symmetric rift using $h = 1.2$ using the cubic spline kernel. Results are shown in Fig 5.24. These results are to be compared with that using the quintic spline kernel (Fig 5.8). The width of the deformation zone, as identified by the size of the ellipsoids of the rate of deformation tensor (right columns of Fig.s 5.8b and 5.24b) is not significantly different when using the cubic spline kernel or the quintic spline

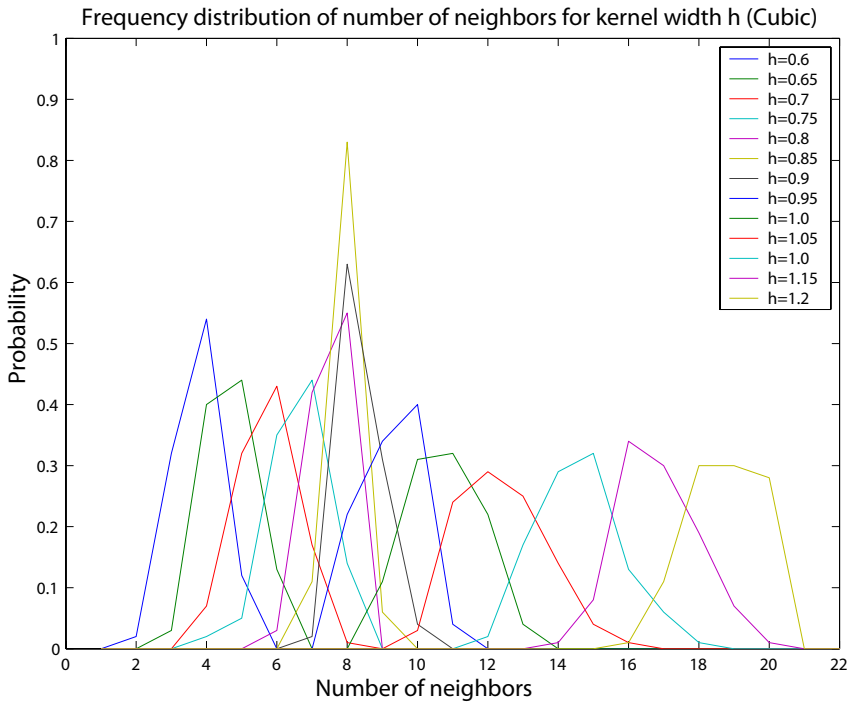

Figure 5.23: Probability distribution of the number of neighbors for the cubic spline kernel with $h = 0.6$–1.2.

kernel. This is somewhat expected since the cubic and quintic spline kernels have nearly the same shape (and first derivative) within a radius of $2h$ (see Fig.s 5.19 and 5.20). The contribution from particles between $2h$ and $3h$ for quintic spline kernel are small. Although the shear bands were not more localized, one beneficial result of this test is that the cubic spline kernel can be used to achieve results similar to the quintic spline kernel. This is beneficial since the cubic spline kernel has far fewer neighbors and is thus computationally much less expensive.

To test the effect of simply reducing the width of the kernel, cases were run with the cubic spline kernel for characteristic widths $h = 1.0$ and $h = 0.85$. For the case (Case 5) with $h = 1.0$ results are shown in Fig 5.25. In this case, comparing the right columns of Fig.s 5.24b and 5.25b shows that there is a slight narrowing of the deformation band, although the change is modest. Further reducing h to 0.85 (Case 6) did not seem to significantly effect the solution (Fig 5.26), however we know from Fig.s 5.22 and 5.23 that the errors can become significant using an h this small.

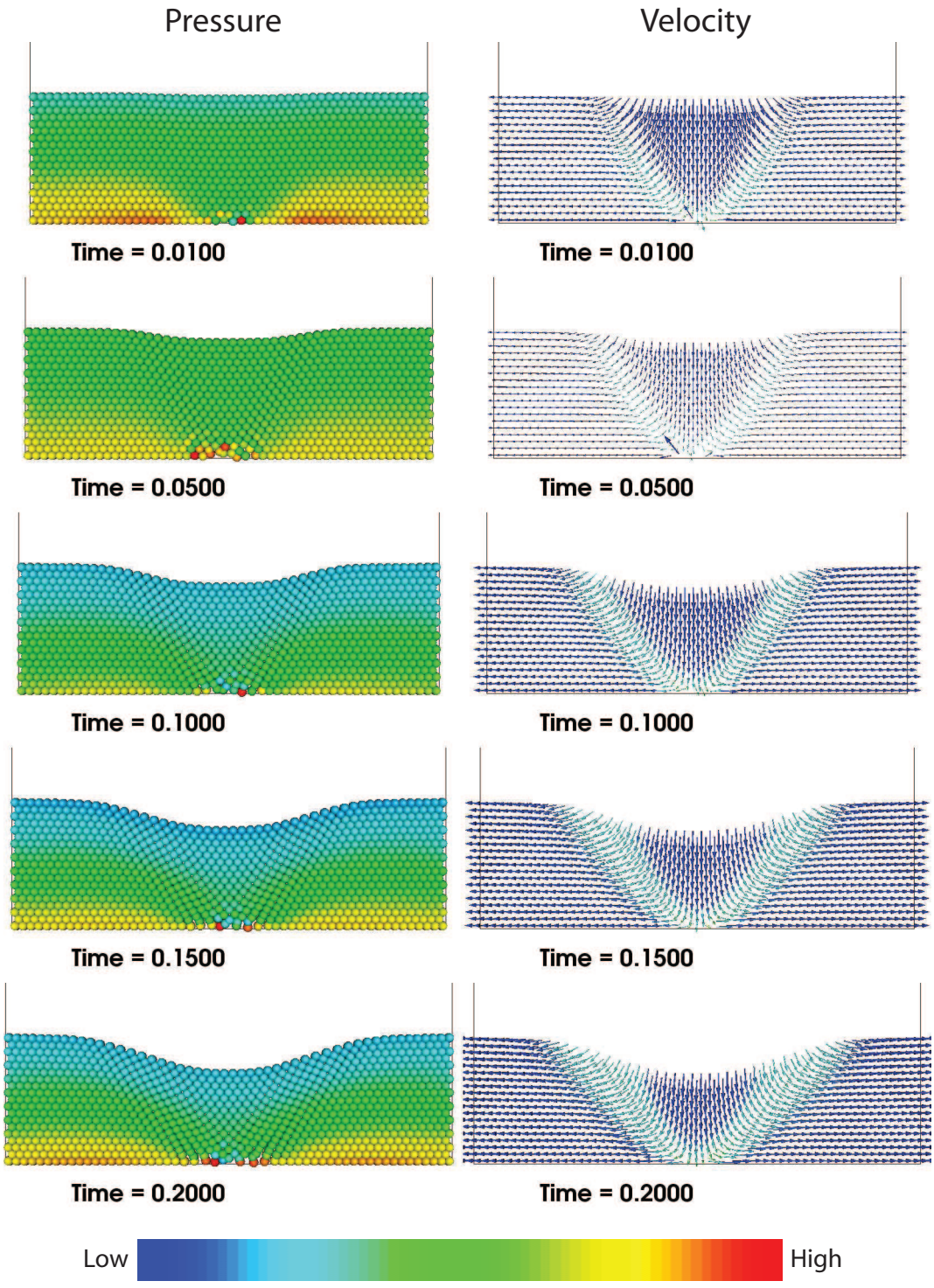

Figure 5.24a: CASE 4: Mohr-Coulomb Rift, (Cubic Spline kernel, $h = 1.2$). Pressure is plotted in the left column (warm colors correspond to higher values) and velocity vectors are plotted in the right column.

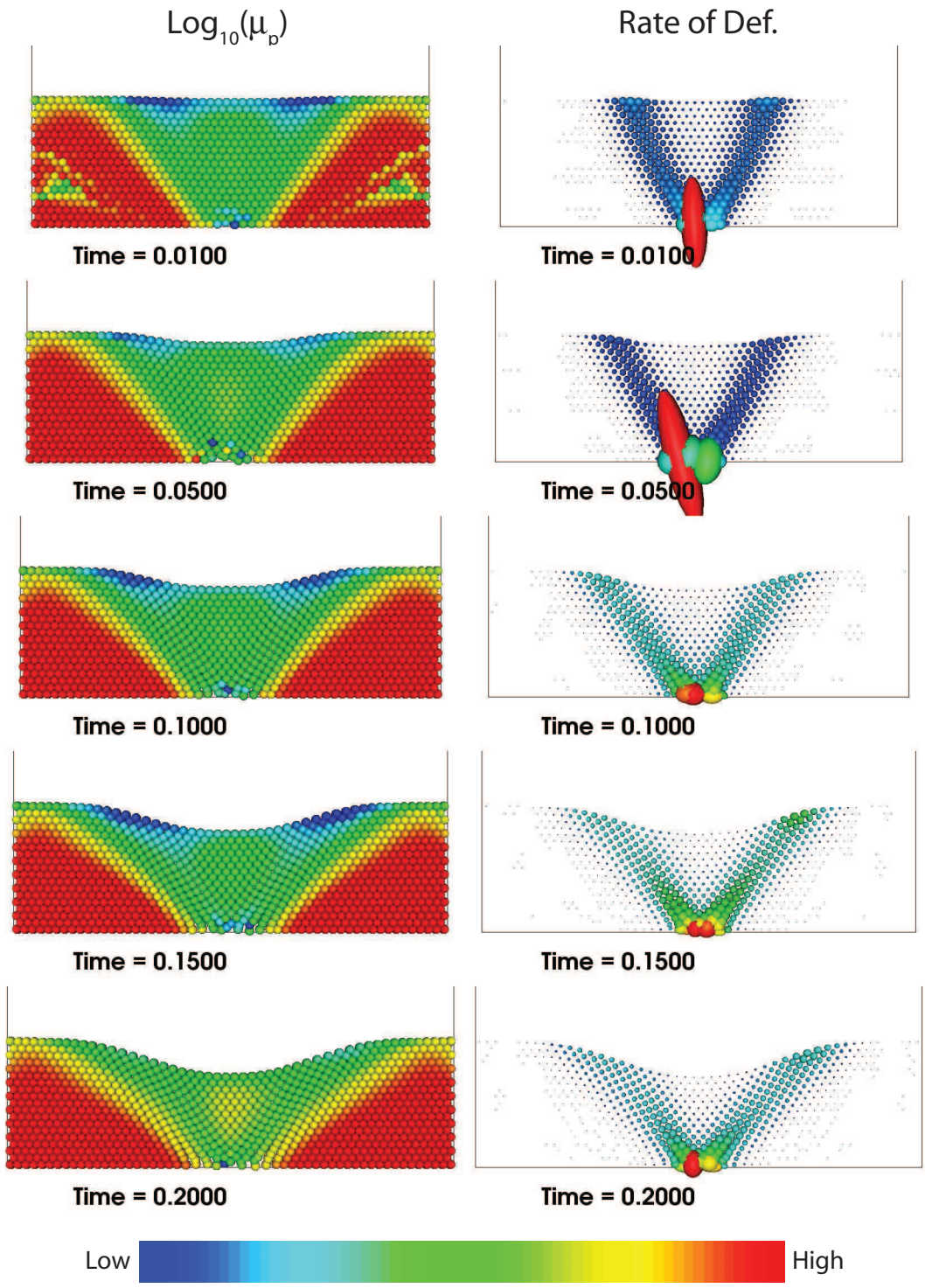

Figure 5.24b: CASE 4: Mohr-Coulomb Rift, (Cubic Spline kernel, $h = 1.2$). $\log_{10} \mu_p$ is plotted in the left column. In the right column, the rate of deformation tensor is plotted, scaled by the eigenvalues and colored by the square root of the second invariant.

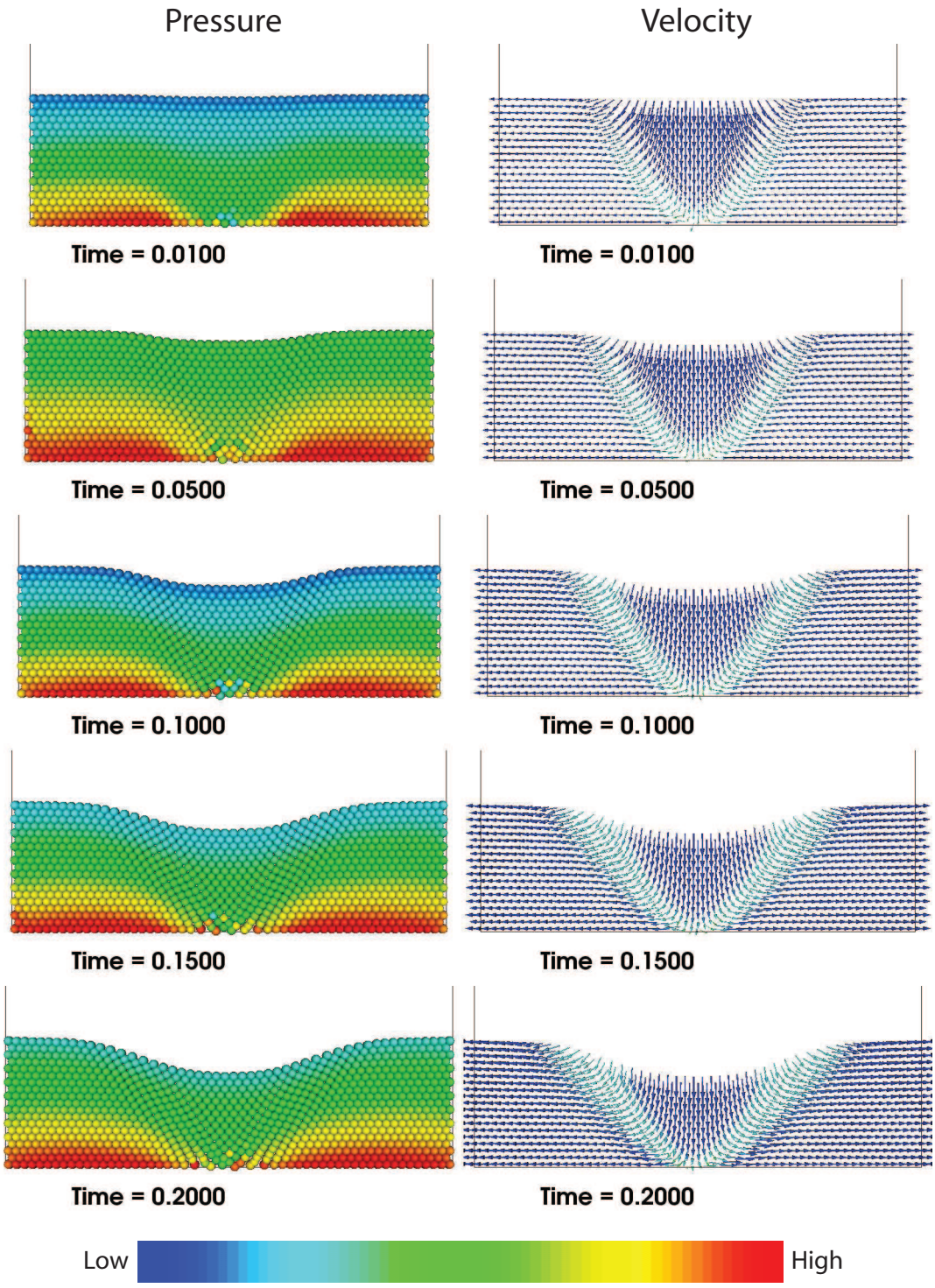

Figure 5.25a: CASE 5: Mohr-Coulomb Rift, (Cubic Spline kernel, $h = 1.0$). Pressure is plotted in the left column (warm colors correspond to higher values) and velocity vectors are plotted in the right column.

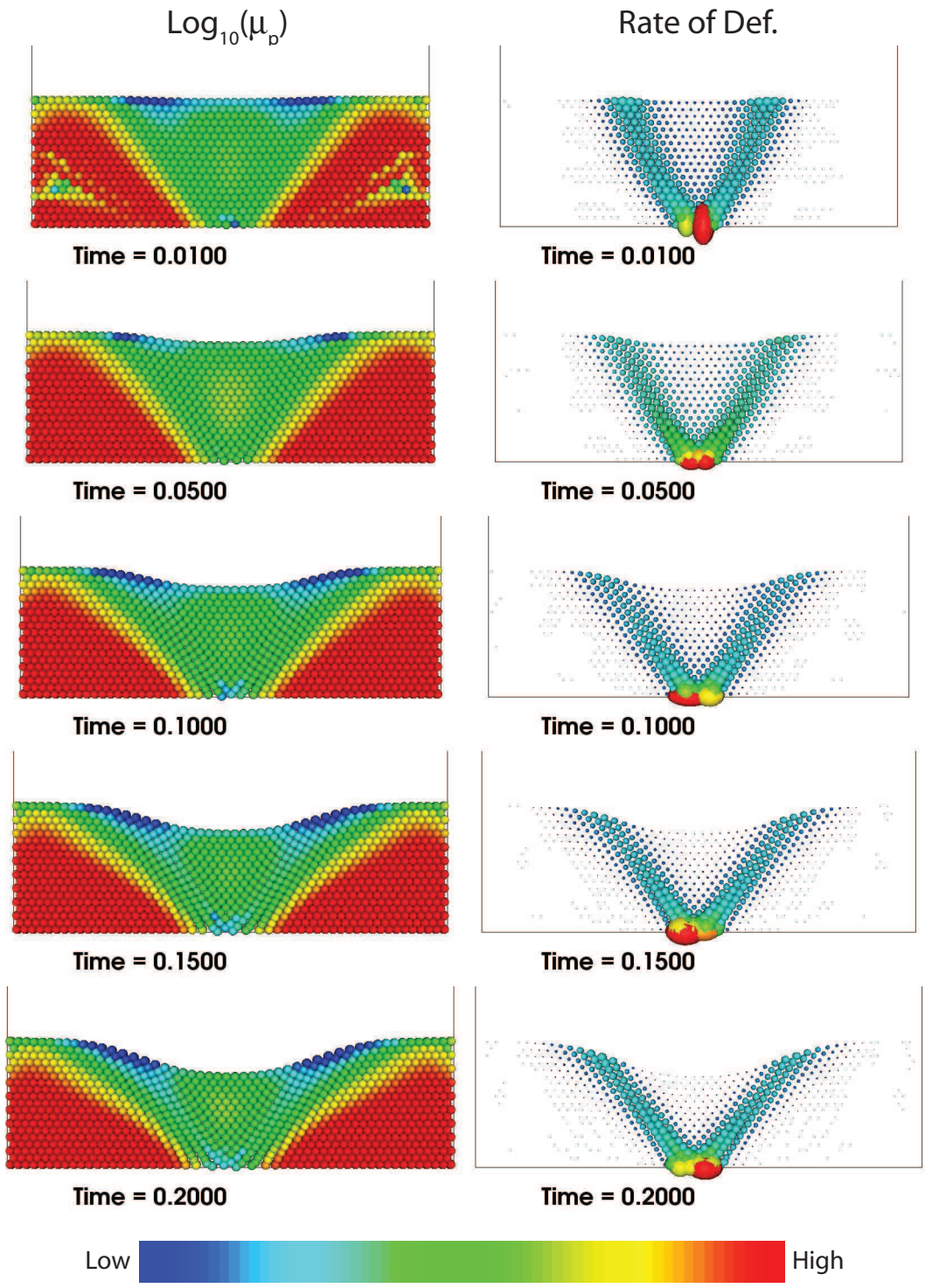

Figure 5.25b: CASE 5: Mohr-Coulomb Rift, (Cubic Spline kernel, $h = 1.0$). $\log_{10} \mu_p$ is plotted in the left column. In the right column, the rate of deformation tensor is plotted, scaled by the eigenvalues and colored by the square root of the second invariant.

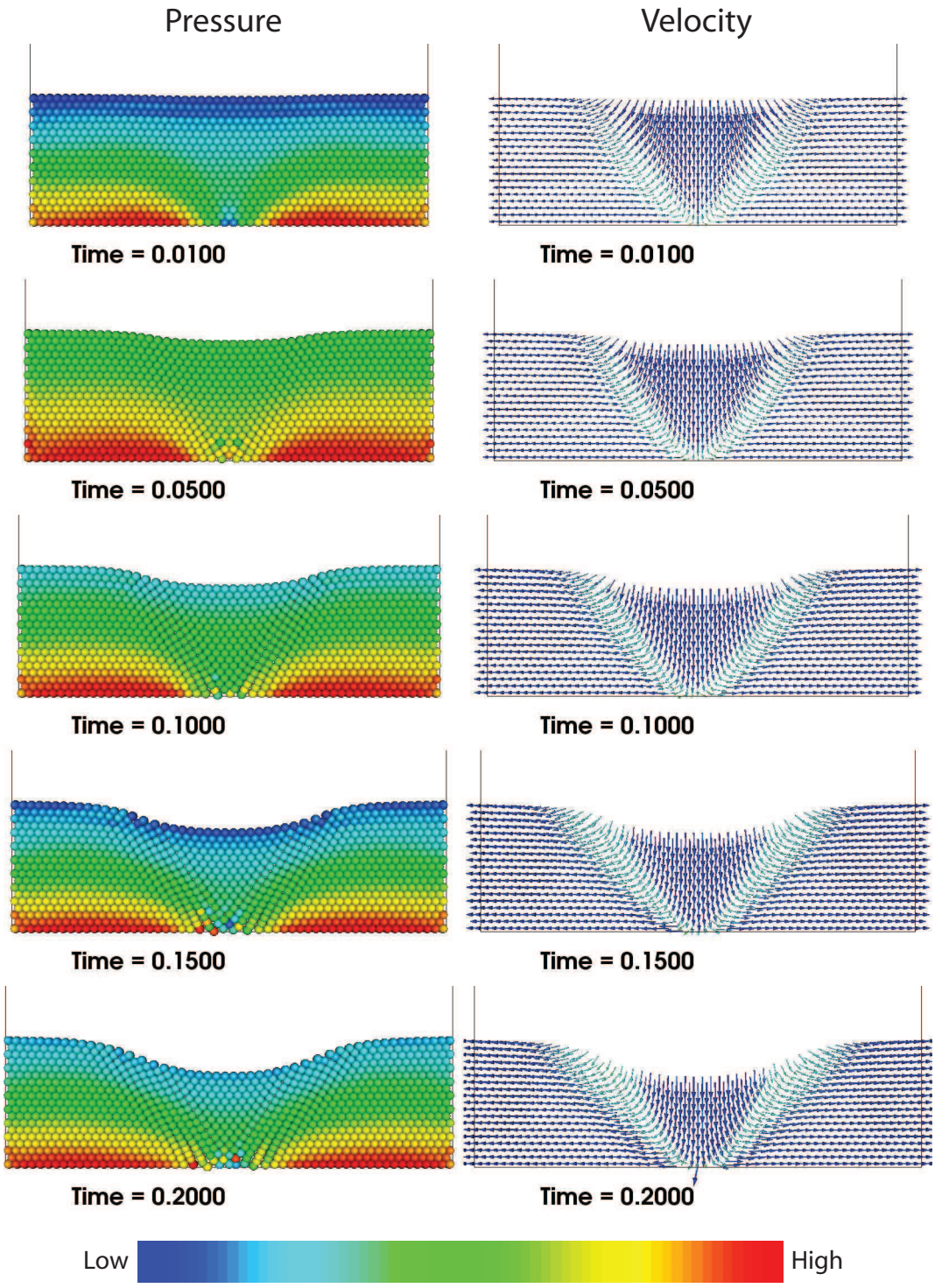

Figure 5.26a: CASE 6: Mohr-Coulomb Rift, (Cubic Spline kernel, $h = 0.85$). Pressure is plotted in the left column (warm colors correspond to higher values) and velocity vectors are plotted in the right column.

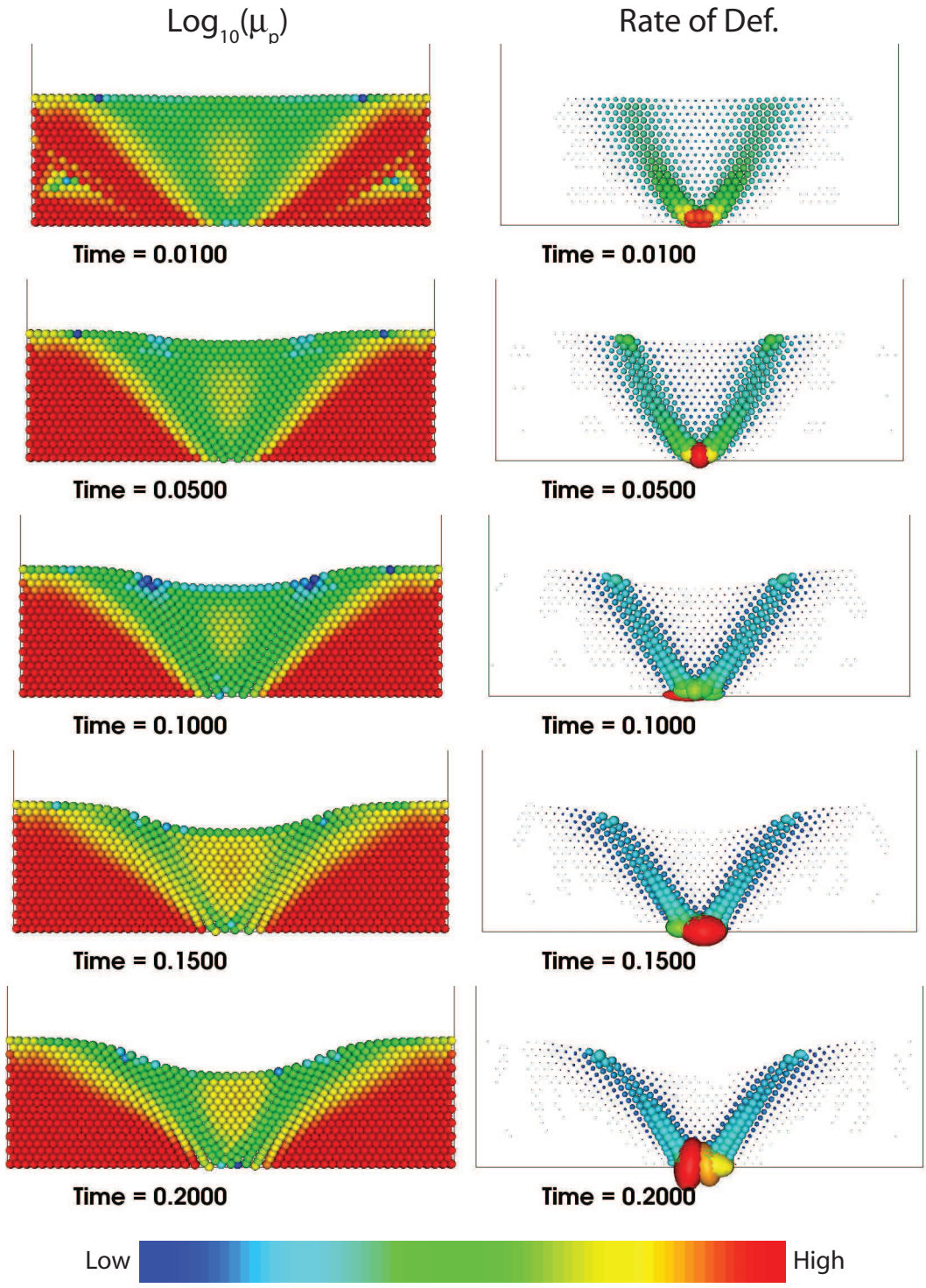

Figure 5.26b: CASE 6: Mohr-Coulomb Rift, (Cubic Spline kernel, $h = 0.85$). $\log_{10} \mu_p$ is plotted in the left column. In the right column, the rate of deformation tensor is plotted, scaled by the eigenvalues and colored by the square root of the second invariant.

5.4.3 Adaptive Refinement (AR)

An alternative method of reducing the kernel width is to have an adaptive characteristic length. This has often been employed in gas dynamics simulations where the smoothing length is evolved in such a way that the mass of the kernel volume remains constant [84]. For incompressible flow problems, this formulation of evolving h to maintain constant volume is no longer feasible. This does not preclude having various kernel widths throughout the domain as a function of the local rate of deformation. However, the kernel width could not be reduced below approximately $h = 0.85$ without a reduction in accuracy (Fig.s 5.17– 5.18 and 5.22–5.23). Unfortunately, this kernel width did not lead to a significant localization of strain.

Rather than just modifying the kernel width, we have implemented an adaptive refinement scheme in which particles are split once the local rate of deformation exceeds a threshold. This allows a locally smaller kernel width by effectivly reducing the particle spacing in the regions where the velocity gradients are highest. The split particles correspond to half the initial volume and mass and acquire the history of the parent particle. For cases where there is a significant flux of material across deformation zones, a method would have to be implemented to merge particles once they have passed through the shear band. Otherwise there is an accumulation of smaller particles which slows down the iterative solver.

In order to capture the high velocity gradients across shear bands, the particles enduring the greatest deformation rates are split. The criterion we employ is the square root of second invariant of the rate of deformation tensor ($\sqrt{I_2}$) exceeding some specified threshold. This value has a dimension of t^{-1} and is problem dependent. Some experimentation is needed to identify a suitable threshold. The choice of the value of the threshold is a balance of the need for increased resolution with the memory and computational constraints. The two daughter particles are placed such that they are normal to the dominant gradient of velocity as determined from the velocity gradient tensor (i.e. placed across the shear band).

At each time step, the velocity and pressure fields are solved on all existing particles. The rate of deformation tensor is calculated with this new velocity field. If the splitting criterion is met, new particles are generated and assigned the history, velocity and pressure of the parent. Particles are then advected and the process repeated.

AR test case

To test the formulation for identifying particles to split and the formulation for the placement of daughter particles, we used the regularly-spaced unit patch with an imposed shear velocity field.

Two levels of refinement were used. The particles were not advected in this test in order to see how many iterations were required for the refinement to be complete. All particles are given a velocity of zero, except those within $r_0 = 1$ of the point ($c_x = 3.25$, $c_y = 3.25$). Particles within this distance were assigned a velocity corresponding to rigid body rotation ($\boldsymbol{v} = \frac{c_x - x}{r}\hat{\boldsymbol{i}} + \frac{c_y - y}{r}\hat{\boldsymbol{j}}$). This initial velocity field is shown in Fig. 5.27.

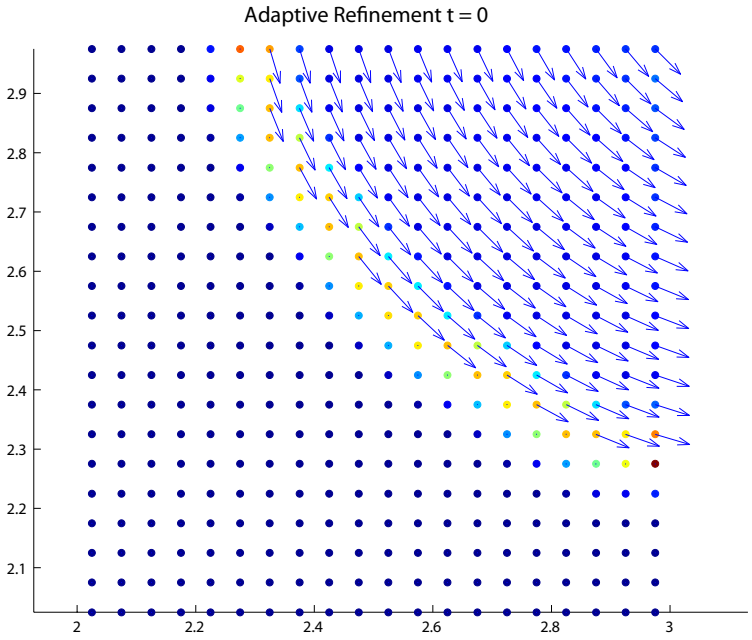

Figure 5.27a: AR test case, t=0. Particle colors correspond to $\sqrt{I_2}$.

Fig. 5.4.3 shows the progressive generation of particles. After four time steps, the shear zone is fully refined to two refinement levels. The orientation of the placement of the daughter particles is in agreement with the local orientation of the shearing along the whole curved shear band.

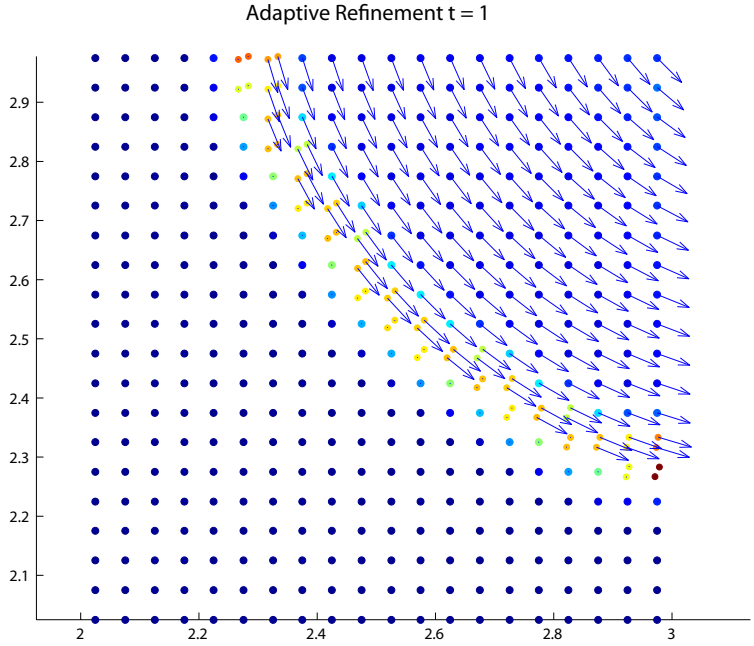

Figure 5.27b: AR test case, t=1.

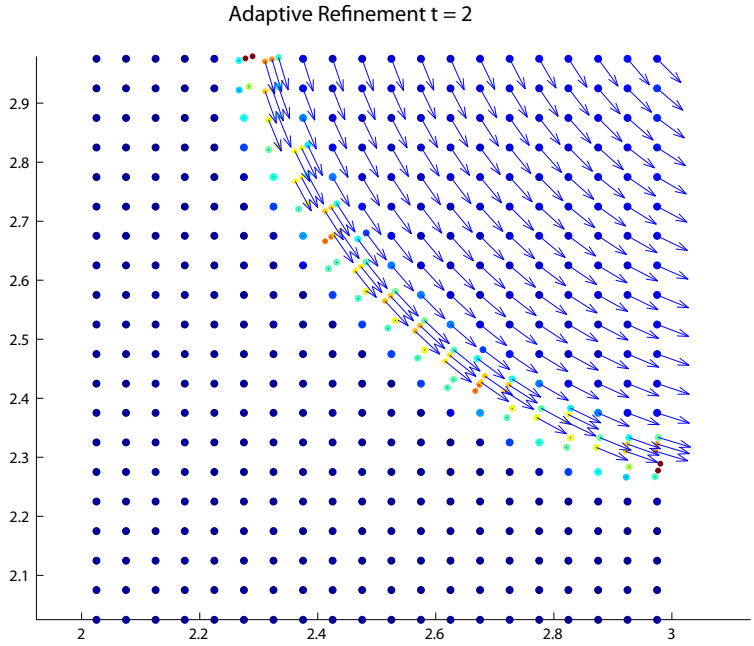

Figure 5.27c: AR test case, t=2.

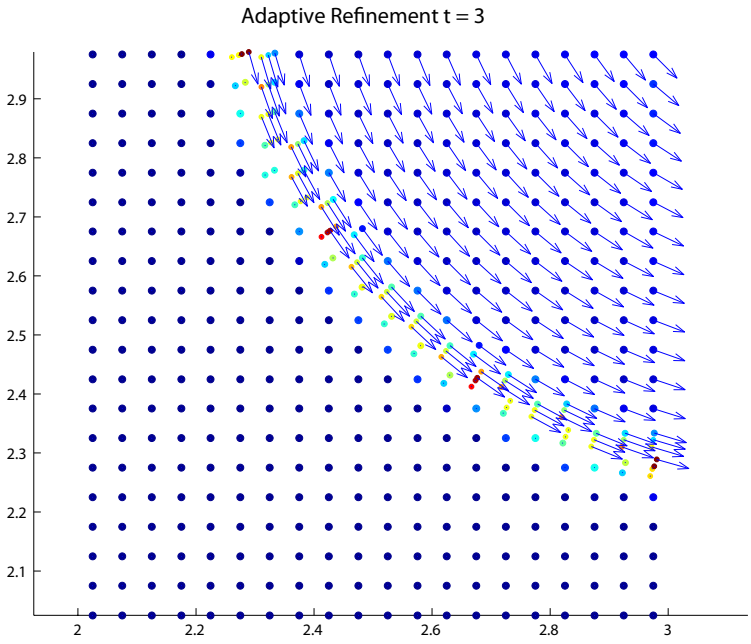

Figure 5.27d: AR test case, t=3.

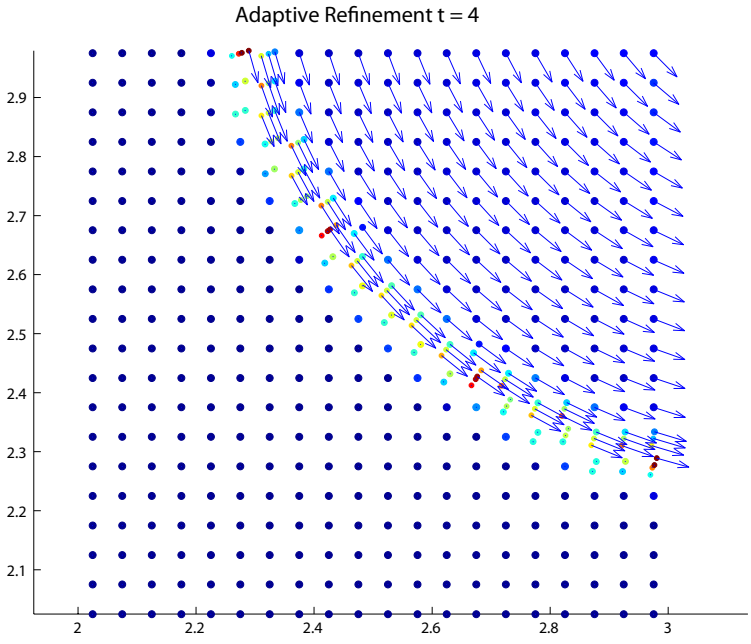

Figure 5.27e: AR test case, t=4.

AR applied to the symmetric rift

This AR scheme was applied to the symmetric rift case with results (Case 7) shown in Fig 5.28. For comparison, the case with the same parameters (h, kernel type) but without the AR scheme is Case 4, shown in Fig 5.24. The plots of plastic effective viscosity show very similar patterns between the two cases, however the AMR does slightly improve the localization of the shear bands as can be seen from the plot of the ellipsoids of the rate of deformation tensor. Two levels of AR refinement were used.

5.4.4 Constitutive Model

Strain-softening

One noticeable feature of the results of the AR model of the symmetric rift is that there is a broad zone of refinement. This broad zone is not a consequence of the lack of localization since the zone is much broader than the deformation bands that do exist. The breadth of this zone is a result of the material flux through the deformation zone. As mentioned in section 5.4.3, a scheme for merging daughter particles once they no longer exceed the threshold deformation rate, has not been implemented. The diffuse shear zone sweeps across the material generating daughter particles that remain refined, resulting in a broad AR zone.

For the shear zone to remain a persistent zone of deformation, some form of rheologic dependence on material history can be included. Although this history dependence is typically thought of as a form of damage or a strain softening, Hobbs et al. [50] noted that strain hardening can also lead to localization. We use strain softening and choose a functional form as suggested by Buiter et al. [11] where there is a linear decrease in the internal angle of friction over a range of finite strain.

There are a number of measures of strain that could be chosen. In our scheme, we follow McKenzie [79] and integrate the finite deformation tensor, F_{ij}, (initialized to the identity matrix) according to

$$F_{ij}^{(n+1)} = F_{ij}^{n} + F_{ik}^{n} v_{k,j}\, \Delta t$$

The right-Cauchy-Green strain tensor [134] (also called the Green deformation tensor [75, 76]) can be calculated according to

$$C = F^{T} \cdot F$$

This is one measure of the full tensor of finite strain, however for the purpose of the strain softening function, we are interested in a scalar measure of finite strain. We use the second invariant of the

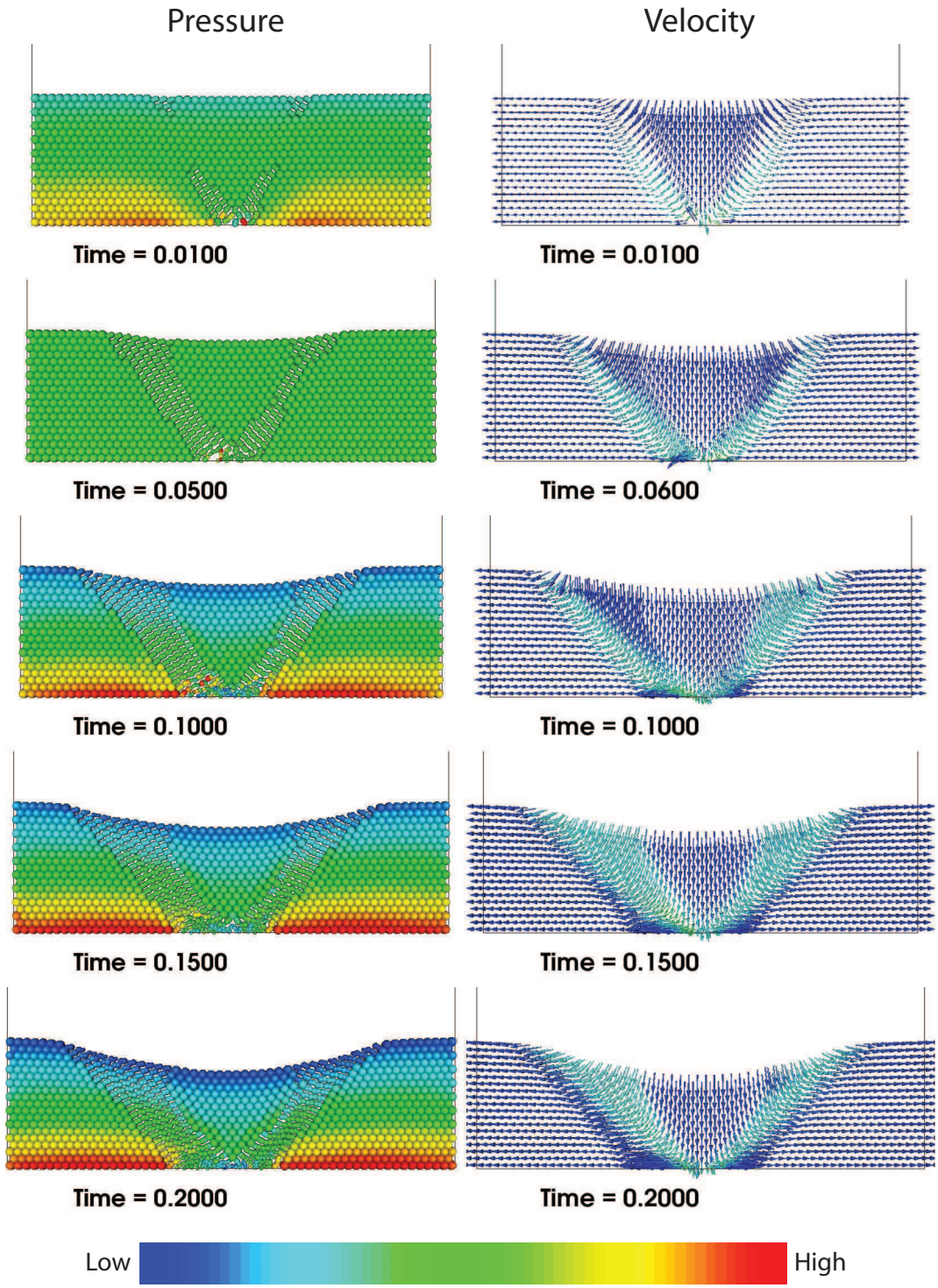

Figure 5.28a: CASE 7: Mohr-Coulomb Rift, (Cubic Spline kernel, $h = 1.2$, Adaptive Refinement). Pressure is plotted in the left column (warm colors correspond to higher values) and velocity vectors are plotted in the right column.

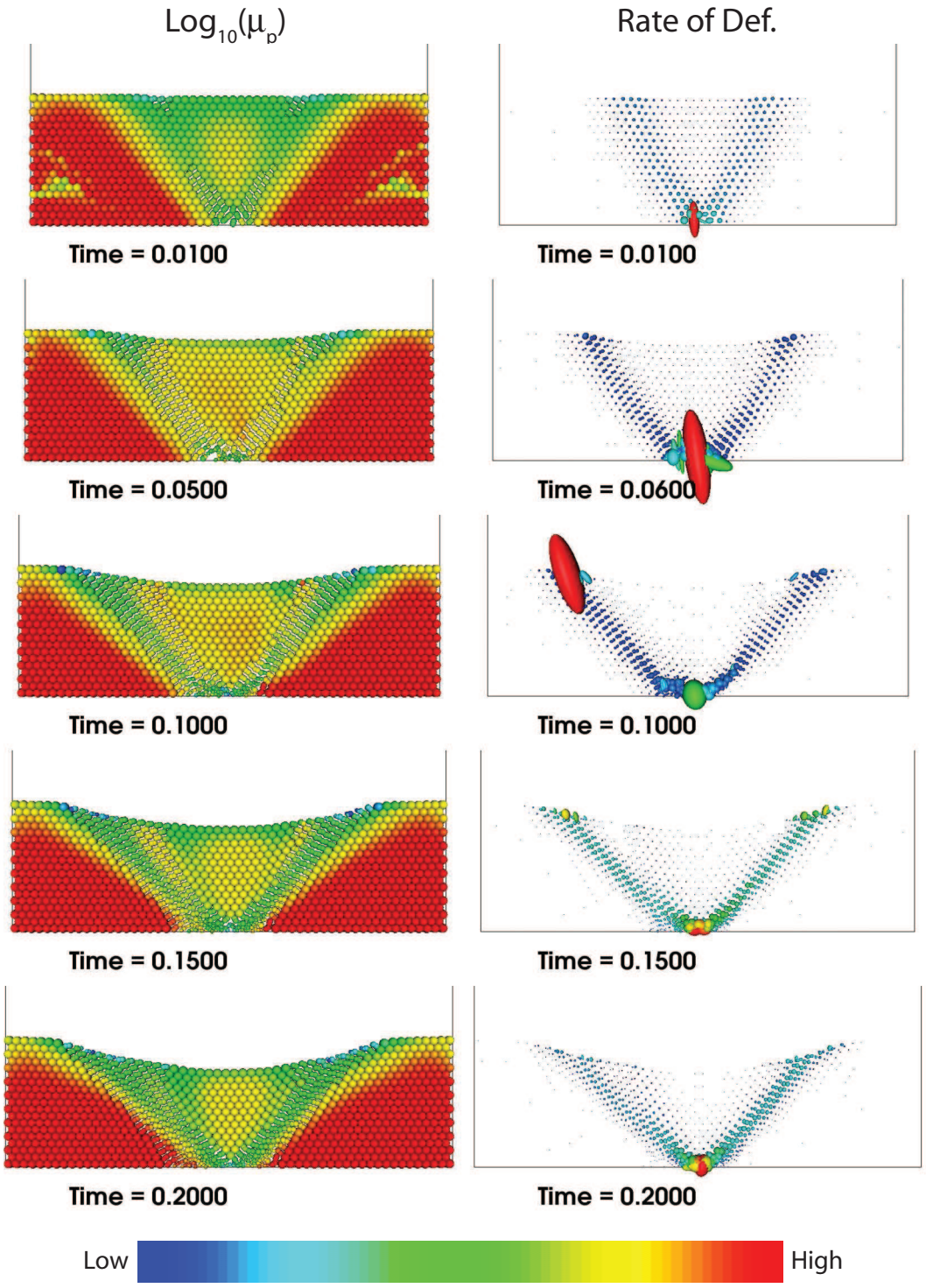

Figure 5.28b: CASE 7: Mohr-Coulomb Rift, (Cubic Spline kernel, $h = 1.2$, Adaptive Refinement). $\log_{10} \mu_p$ is plotted in the left column. In the right column, the ellipsoids of the rate of deformation tensor is plotted, scaled by the eigenvalues and colored by the square root of the second invariant.

right Hencky (or natural) finite strain tensor. The tensor is given by [134]:

$$\lambda_{ij}^{r} = \frac{1}{2}(\ln C)_{ij}$$

The second invariant of λ_{ij}^{r} is simply the natural log of the second invariant of the right-Cauchy-Green strain (C), which can be calculated from the eigenvalues of C according to (for 2-D) [76]

$$C_{II} = \frac{1}{2}\left[(\lambda_1 + \lambda_2)^2 - \left(\lambda_1^2 + \lambda_2^2\right)\right]$$

Application to symmetric rift

As a first test of the effects of strain softening, we use the baseline test (Case 1, quintic spline kernel, $h = 1.2$) but include damage by reducing the internal angle of friction from 40° to 20° over the finite strain interval from 0.2 to 0.7 (Case 8). Results are shown in Fig 5.29. The progressive damage can be seen from the left column of Fig. 5.29b which shows the internal angle of friction. The necking is slightly narrower as well as the shear bands, however the effect is not dramatic.

A second strain softening test function was used where ϕ ranges from 40° to 5° (Case 9) over the same finite strain interval as before. Results are plotted in Fig. 5.30. Again, the difference in localization is minor.

The inclusion of the adaptive refinement scheme with strain softening, however, leads to a dramatic localization of strain. Result from the one-level refinement (Case 10) are shown in Fig. 5.31 while the two-level refinement (Case 11) is shown in Fig. 5.32.

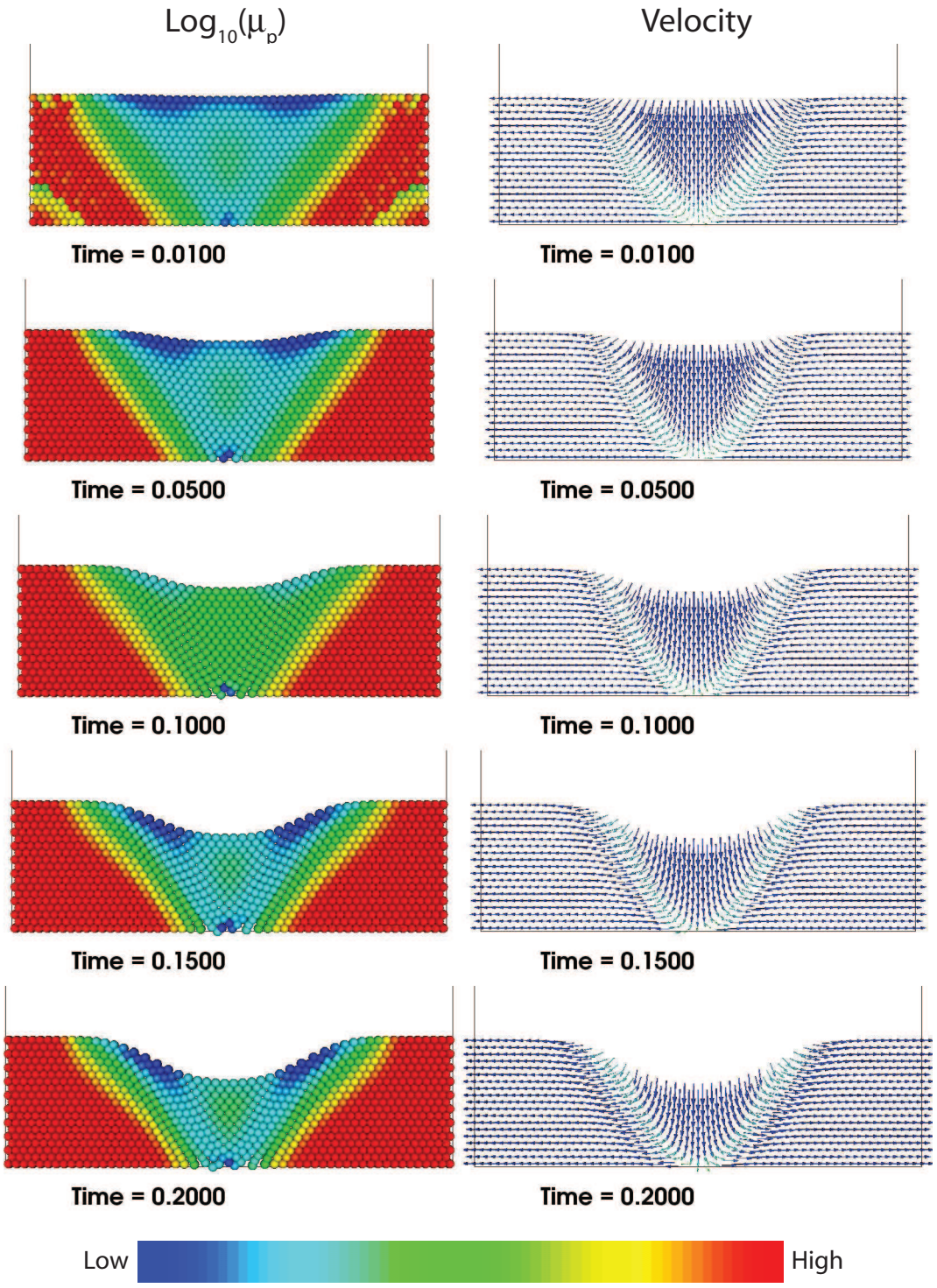

Figure 5.29a: CASE 8: Mohr-Coulomb Rift, (Quintic Spline kernel, $h = 1.2$, Strain-softening ($\phi = 40°$–$20°$)). $\log_{10} \mu_p$ is plotted in the left column (warm colors correspond to higher values) and velocity vectors are plotted in the right column.

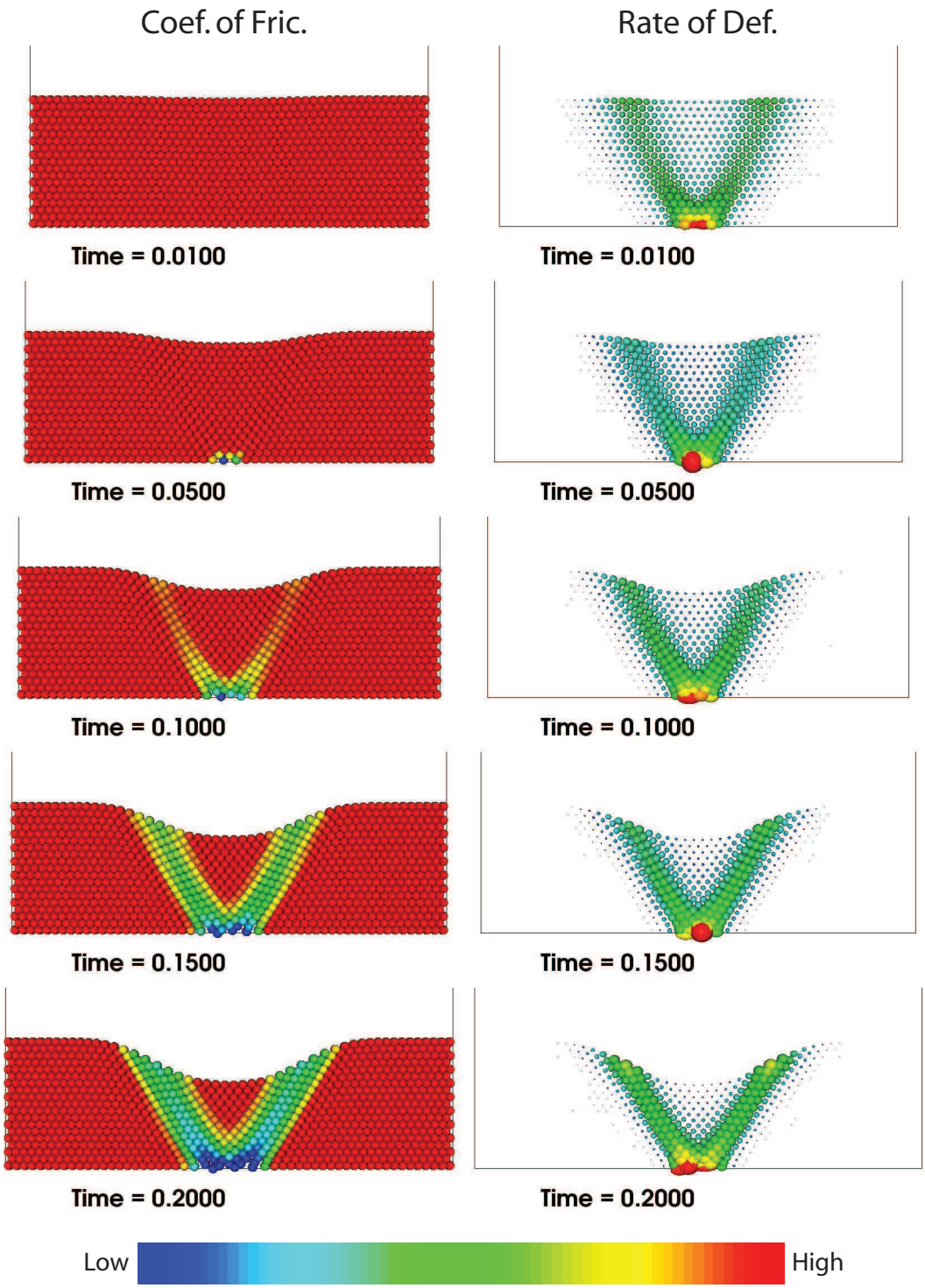

Figure 5.29b: CASE 8: Mohr-Coulomb Rift, (Quintic Spline kernel, $h = 1.2$, Strain-softening ($\phi = 40°$–$20°$)). The coefficient of friction ($\tan\phi$) is plotted in the left column. In the right column, the rate of deformation tensor is plotted, scaled by the eigenvalues and colored by the square root of the second invariant.

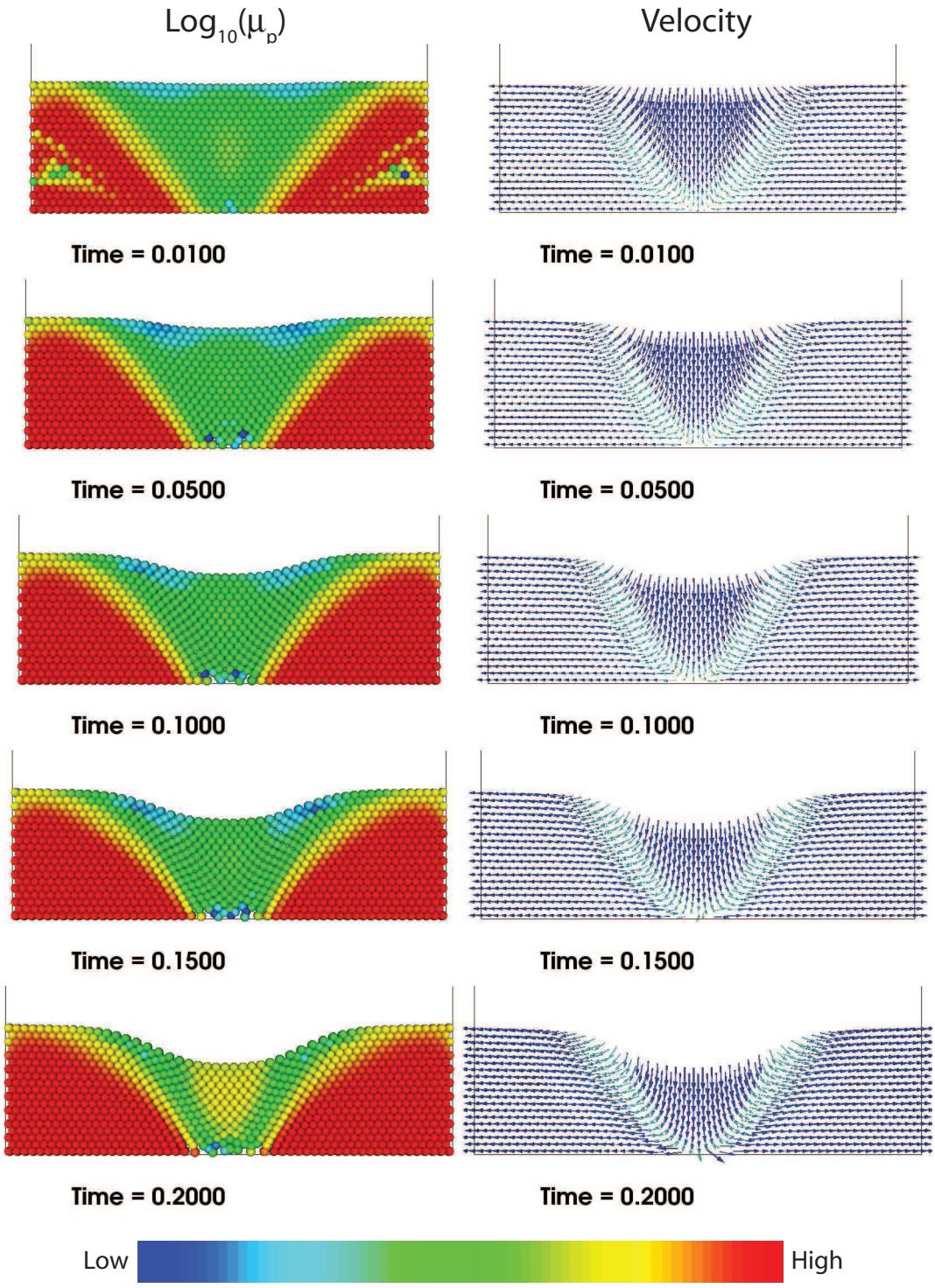

Figure 5.30a: CASE 9: Mohr-Coulomb Rift, (Quintic Spline kernel, $h = 1.2$, Strain-softening ($\phi = 40°$–$5°$)). $\log_{10} \mu_p$ is plotted in the left column (warm colors correspond to higher values) and velocity vectors are plotted in the right column.

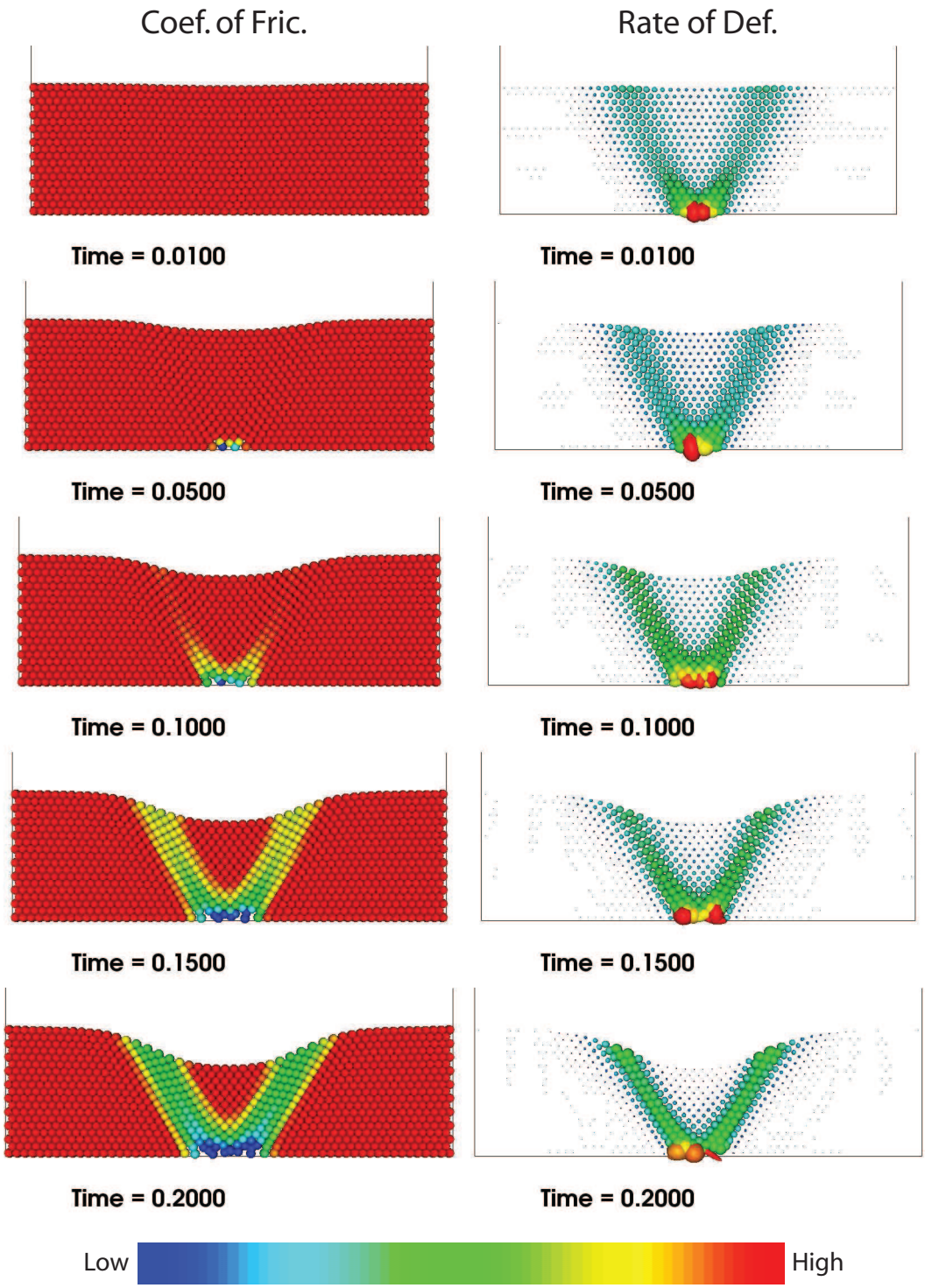

Figure 5.30b: CASE 9: Mohr-Coulomb Rift, (Quintic Spline kernel, $h = 1.2$, Strain-softening ($\phi = 40°$–$5°$)). The coefficient of friction ($\tan\phi$) is plotted in the left column. In the right column, the rate of deformation tensor is plotted, scaled by the eigenvalues and colored by the square root of the second invariant.

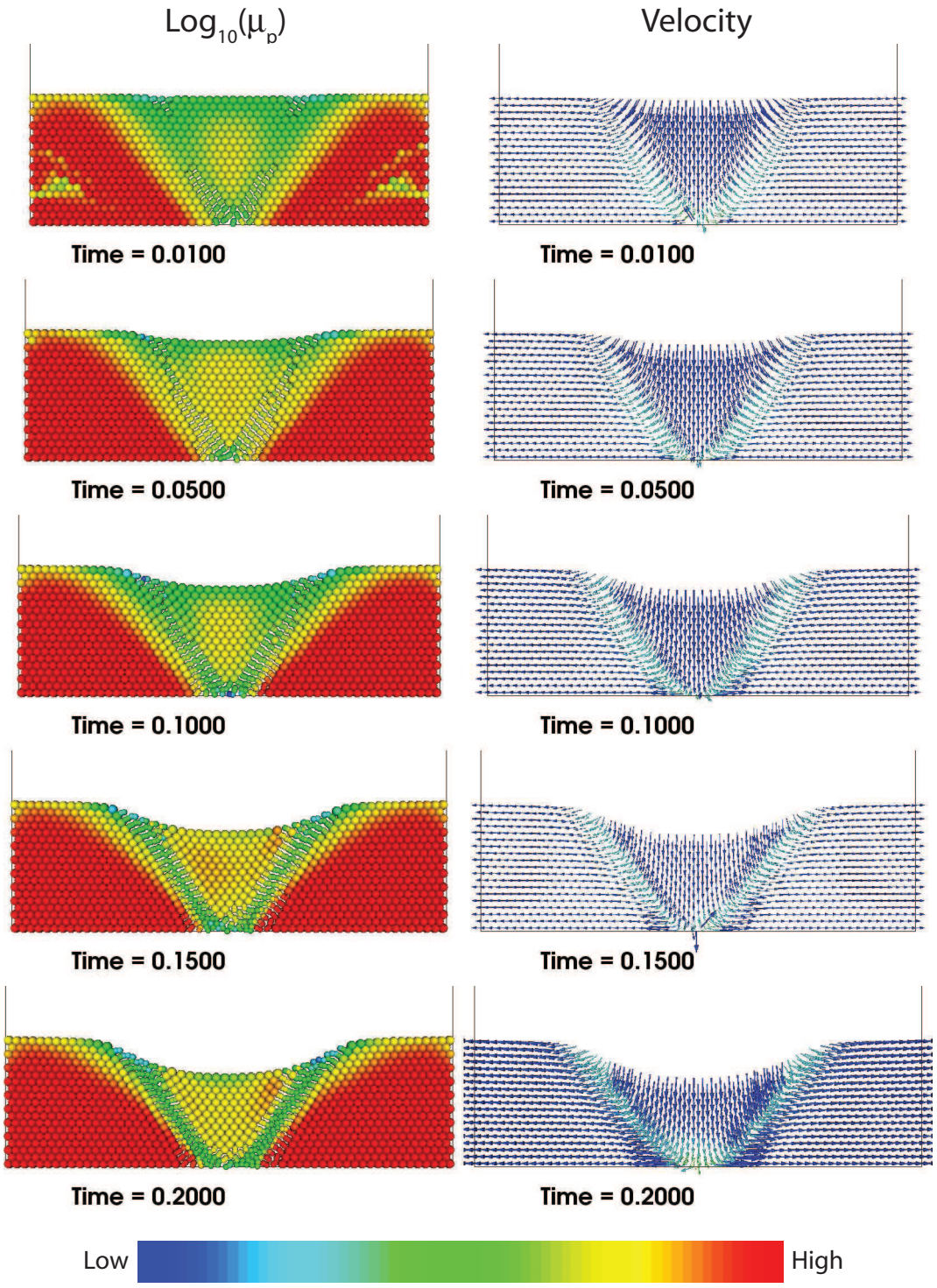

Figure 5.31a: CASE 10: Mohr-Coulomb Rift, (Cubic Spline kernel, $h = 1.2$, Strain-softening ($\phi = 40°$–$5°$), One-level Adaptive Refinement). $\log_{10} \mu_p$ is plotted in the left column (warm colors correspond to higher values) and velocity vectors are plotted in the right column.

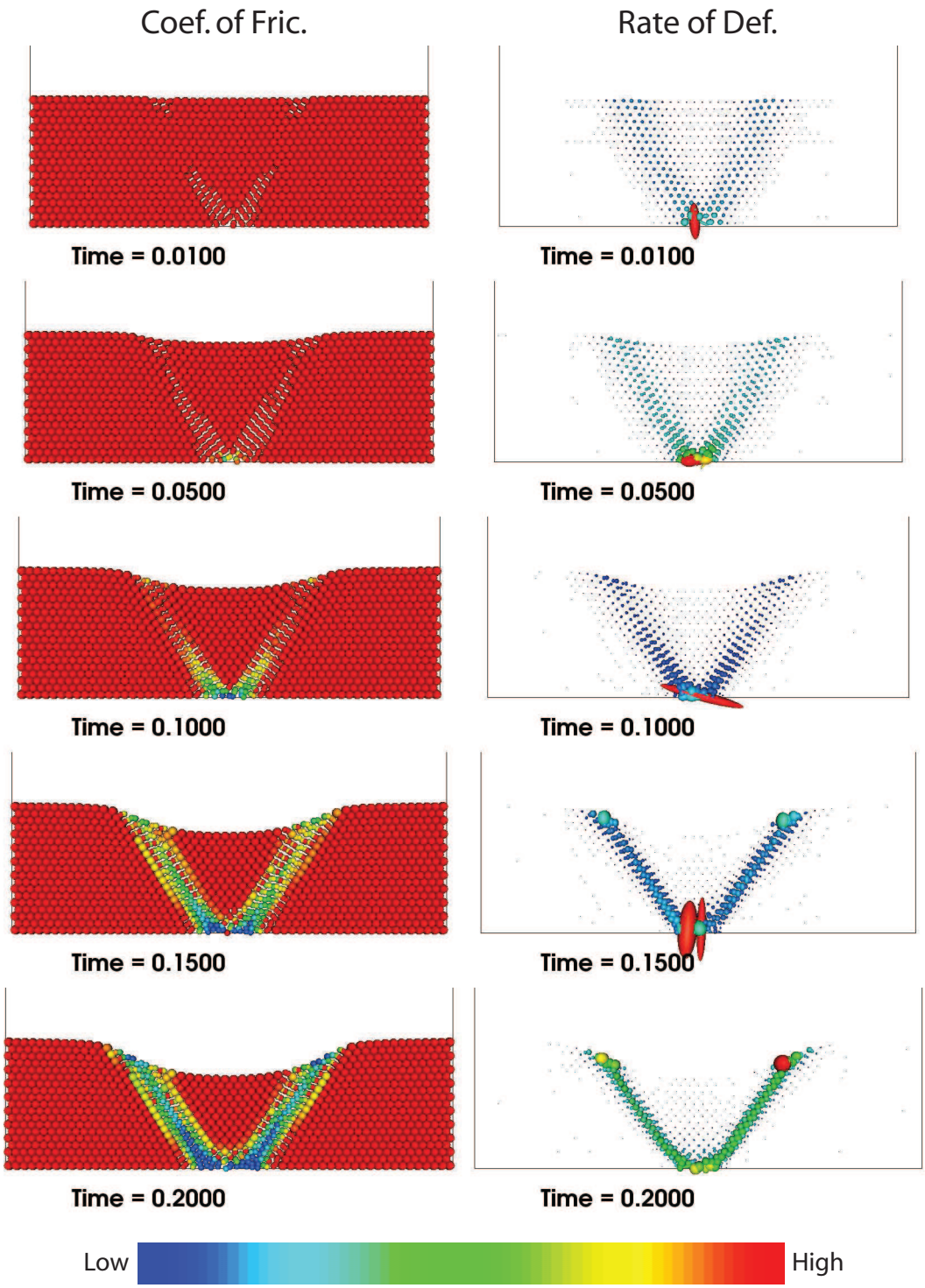

Figure 5.31b: CASE 10: Mohr-Coulomb Rift, (Cubic Spline kernel, $h = 1.2$, Strain-softening ($\phi = 40°$–$5°$), One-level Adaptive Refinement). The coefficient of friction ($\tan\phi$) is plotted in the left column. In the right column, the rate of deformation tensor is plotted, scaled by the eigenvalues and colored by the square root of the second invariant.

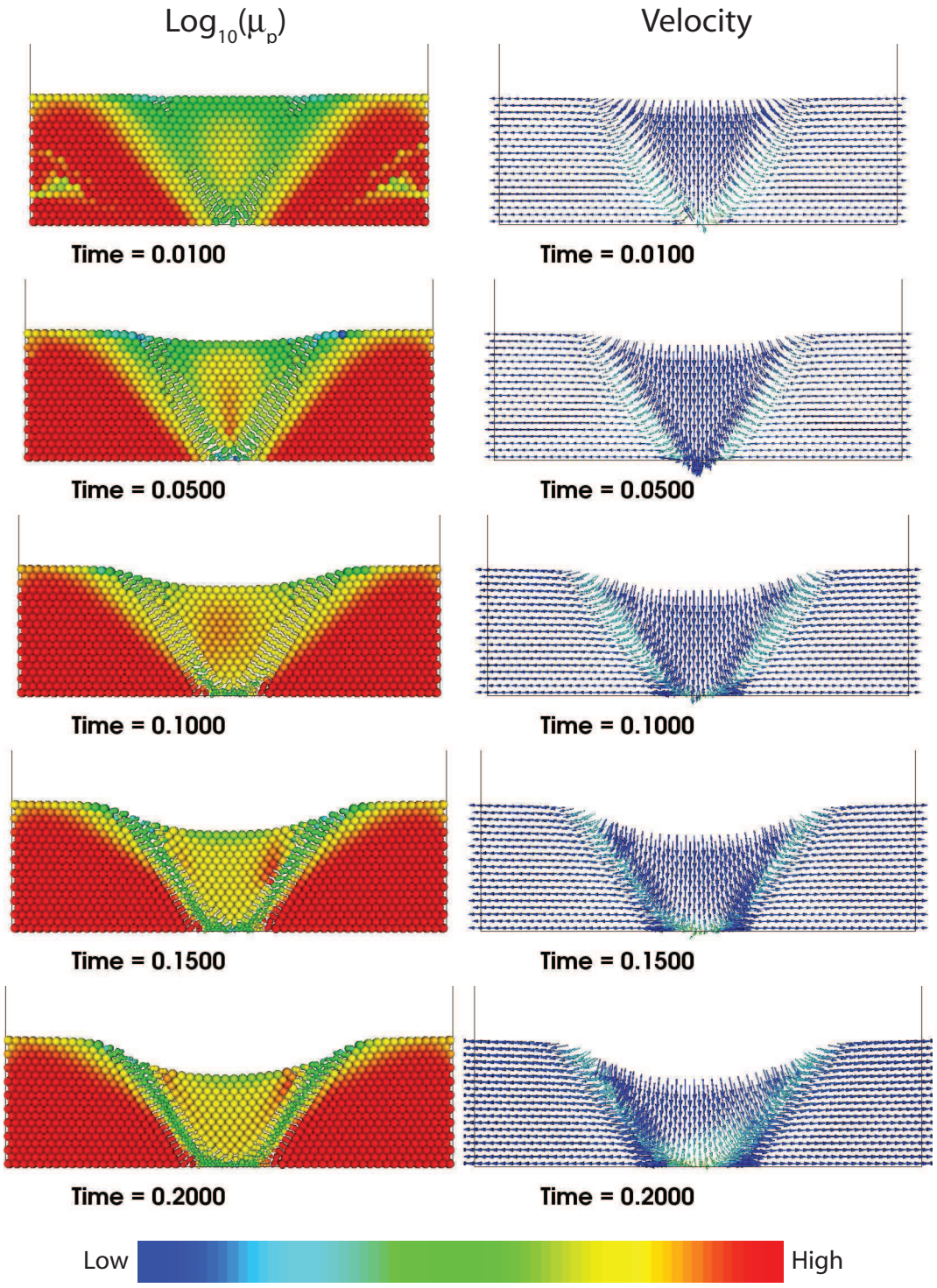

Figure 5.32a: CASE 11: Mohr-Coulomb Rift, (Cubic Spline kernel, $h = 1.2$, Strain-softening ($\phi = 40°$–$5°$), Two-level Adaptive Refinement). $\log_{10} \mu_p$ is plotted in the left column (warm colors correspond to higher values) and velocity vectors are plotted in the right column.

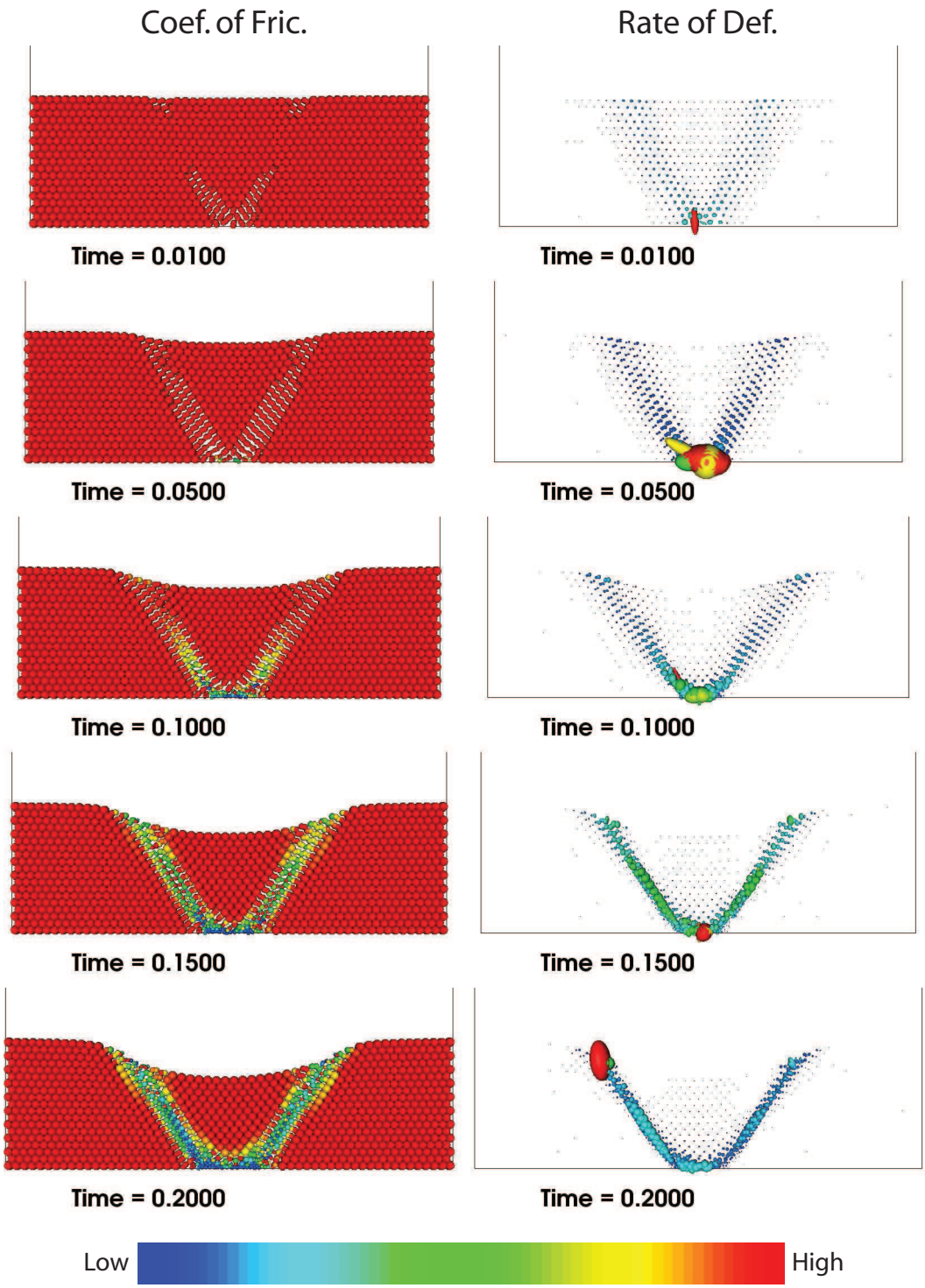

Figure 5.32b: CASE 11: Mohr-Coulomb Rift, (Cubic Spline kernel, $h = 1.2$, Strain-softening ($\phi = 40°$–$5°$), Two-level Adaptive Refinement). The coefficient of friction ($\tan\phi$) is plotted in the left column. In the right column, the rate of deformation tensor is plotted, scaled by the eigenvalues and colored by the square root of the second invariant.

Table 5.1: Table of Mohr-Coulomb rift cases

Case	Str.-Soft.	Kernel	h	Lap.	AR
1	No ($\phi = 30°$)	Quintic	1.2	L1	No
2	No ($\phi = 30°$)	Cubic	1.0	L2	No
3	No ($\phi = 30°$)	Cubic	1.0	L2–Γ	No
4	No ($\phi = 30°$)	Cubic	1.2	L1	No
5	No ($\phi = 30°$)	Cubic	1.0	L1	No
6	No ($\phi = 30°$)	Cubic	0.85	L1	No
7	No ($\phi = 30°$)	Cubic	1.2	L1	AR–1
8	$\phi = 40° \rightarrow 20°$	Cubic	1.2	L1	No
9	$\phi = 40° \rightarrow 5°$	Quintic	1.2	L1	No
10	$\phi = 40° \rightarrow 5°$	Cubic	1.2	L1	AR–1
11	$\phi = 40° \rightarrow 5°$	Cubic	1.2	L1	AR–2

5.5 Discussion

Once the corrected Laplacian term (described in chapter 3) is applied to pressure and the stationary hybrid perturbation to the continuity equation (described in chapter 4) is used, the Mohr-Coulomb rheology is fairly straight-forward to implement. The results of the angle of repose test for the collapse of Mohr-Coulomb material were satisfactory, as were the comparison of the SPH rift case with the FEM solution. The localization of strain however proved to be much more elusive.

Capturing this localization of strain is important in modeling the brittle deformation of crustal material, and is in fact the primary motivation for employing a mesh-free method. The difficulty is due, in part, to the width of the smoothing kernel. This is because particles on the far side of an idealized fault would contribute to the viscous stress by the same amount as if the fault were not present. The focus of improving the localization of strain was reducing the kernel width so as to minimize the influence of particles across faults. Much effort went into investigating the limits of reducing the kernel width which included applying corrections to the viscous term to improve accuracy, reducing the kernel order, reducing the characteristic width (h) and adaptively splitting particles. None of these techniques by themselves led to the significant localization of strain.

A second approach was to modify the constitutive behavior to include a history dependence through a strain-softening function. This also only led to modest improvements in strain localization. Strain-softening coupled with the adaptive refining, however, led to highly localized deformation bands. The goal is to mitigate as much as possible any hinderance the numerical scheme might have on the evolution of the physical problem. Strain-softening, but with the lack of refinement, leads to a resolution-dependent constraint on the width of the shear bands. Adaptively increasing the resolution, alleviates this numerical constraint and allows the localization to sharpen.

There are a few points to note. An inspection of the velocity vectors in the right-side column of Fig. 5.32a or the ellipsoids of the rate of deformation tensor in the right-side column of Fig. 5.32b shows that the shear bands are still several particles thick. This could potentially be reduced by using the corrected Laplacian term, however the instability in the velocity solution needs to be identified and remedied. We suspect this instability is due to the lack of velocity boundary conditions enforced at the stress-free surface.

Secondly, the method of refining particles works well, but a method of merging particles of the appropriate AMR level needs to be implemented so that faults that become dormant can undergo a coarsening of resolution.

Faults did not go dormant in any of the rifting cases, however preliminary tests of doubly-vergent wedge cases with AMR and strain-softening do show the forward migration of faults. This is

somewhat surprising since the basal boundary condition is no-slip, not frictional. To properly apply the refinements developed in this chapter to the double-vergent wedge case, frictional basal sliding would need to be included.

Lastly, the strain-softening function allows for the development of much weaker material than other authors have employed. Buiter et al. [11], for example, used a linear decrease of ϕ from 36° to 31° over the finite strain range of 0.5–1.0. Further work is needed to compare SPH results with results from other published methods.

Chapter 6

SUMMARY AND DISCUSSION

The brittle failure of geomaterials is a problematic process to simulate numerically, especially if the post-failure deformation is large. The aim of this project has been to develop a mesh-free continuum-based numerical method for the large-deformation of heterogeneous, history-dependent material to be applied to tectonic deformation. The motivation in using a mesh-free framework is to draw on the successes of the Distinct Element Method in modeling, through the frictional contacts of numerical 'grains', the sharp failure planes (faults) in Mohr-Coulomb material, but to also include the ability to model deformation based on a continuum description, such as viscous deformation. The hope is that a mesh-free, Lagrangian model will be able to track material history and accommodate highly-localized deformation without the difficulties associated with modeling shear bands with mesh-based methods.

Smoothed Particle Hydrodynamics is among the simplest mesh-free methods to implement and is well suited to model certain classes of geophysical flows such as the high-velocity impact of two fluids as illustrated in chapter 2. The lack of consistency of SPH in regions where the kernel loses some of its support (i.e. near surfaces), however, causes problems accurately representing function values and gradients. Much work was required to modify the standard SPH method to remedy this deficiency and many authors have proposed correction methods [18, 147, 67, 5]. For the quasi-static creeping incompressible flow problems of tectonic deformation, the same issue of a deficient kernel support region manifested itself in calculations of the Laplacian. Moreover, the standard SPH implementation of incompressible flow is not suited for the high viscosities needed for creeping flow.

In chapters 3 and 4, methods were developed to remedy these problems. Chapter 3 outlines a proposed method of correcting the Laplacian discretizations. Although the correction method is presented in the context of thermal diffusion, Laplacian discretization are important in creeping flow problems both in the form of $\nabla^2 \boldsymbol{v}$ and $\nabla^2 p$. The correction method was found to significantly improve Laplacian calculations in the vicinity of surfaces where kernel support becomes deficient.

Since a Mohr-Coulomb rheology is pressure sensitive, the next step towards a tectonic model was to apply these correction methods to calculating smooth pressure solutions for creeping, linear viscous flow. Chapter 4 outlined a method of imposing the incompressibility constraint for creeping viscous

flows based on a generalization of the quasi-compressibility perturbations to the constraint $\nabla \cdot \boldsymbol{v} = 0$. In both this chapter and the previous, care was taken to develop a method of imposing both Dirichlet and Neumann boundary conditions. When the equations are cast implicitly, boundary conditions are enforced by augmenting the set of variables, subject to the constraint that the boundary conditions are satisfied. This method works well both when enforcing boundary conditions through ghost particles at wall-boundaries, and along the particles at fluid surfaces.

With the creeping flow implementation of SPH developed, chapter 5 could focus on incorporating the non-linear viscosity to simulate Mohr-Coulomb behavior and the localization of strain. The SPH implementation of Mohr-Coulomb rheology compared favorably with finite element solutions, however the resulting shear bands were quite diffuse. Much of this chapter was devoted to improving strain localization. Strain-softening was included to encourage shear bands to persist, however the primary difficulty seems to be that the SPH kernel, in order to calculate accurate values, requires too broad of a support region. This breadth then inhibits strain-localization. Tests were run to determine how much this breadth could be reduced, how narrow the kernel could be set, and still return accurate values. It was found that applying the correction terms to the Laplacian discretization, as developed in chapter 3, allowed a smaller kernel width to be used while maintaining accurate values for the Laplacian of a vector field. Unfortunately, when applying this to the creeping flow case, the velocity field was unstable, likely a result of the lack of velocity boundary condition at the stress-free surface. This approach of reducing the allowable kernel width by compensating for the deterioration of the Laplacian by including correction terms shows promise. More work is needed to address the stress-free boundary condition.

The more successful approach investigated in this chapter was to reduce the effective kernel width by adaptively increasing the resolution in regions of high deformation. This increase in resolution was achieved by splitting particles in the appropriate regions and resulted in highly-localized deformation bands.

The methods outlined in this chapter successfully extend SPH to modeling the brittle failure of Mohr-Coulomb material, however further work is needed in several aspects. As mentioned above, imposing the stress-free boundary condition needs to be improved. Further work is also needed to verify that incompressibility is maintained through the adaptive refinement. Thirdly, the iterative solver used is quite slow and could likely be improved by preconditioning.

Additionally, since this method is based on a visco-plastic continuum model, the 'faults' do not behave like the sliding of blocks on a frictional surface. Although the localization behavior shows promise for modeling brittle and ductile crustal deformation, it is not clear that the width of the

smoothing kernel can be overcome efficiently. It is possible that the smoothing nature of SPH, in essence is incompatible with the sharp localization of strain.

Furthermore, Lagrangian hydrocodes are best suited for modeling systems where there is a fixed amount of material. In crustal dynamics, there is a growing body of literature noting the coupling of geomorphic processes with tectonic deformation. Mass flux boundary conditions, both erosional and depositional, would not be straight-forward to implement within this model. This difficulty would also hamper the application of the creeping viscous SPH model to other similar flows such as that of glaciers where quantity of ice is controlled by the flux through the surface by ablation or accumulation.

Nevertheless, the viscous SPH model is a useful numerical framework for modeling a broad class of flows, especially flows which require the tracking of material interfaces, the tracking of material history, or coupled thermo-mechanical problems.

For example, many geophysical flows require the tracking of material interfaces; from flows such as the Rayleigh-Taylor instability of salt diapers to various gravity currents (landslides, turbidity currents, pyroclastic flows). Interfaces can be tracked with mesh-based methods by advecting an interface function, however the Lagrangian scheme tracks these interfaces as an inherent aspect of the method. This is advantageous when there are specific interface conditions that need to be imposed or investigated. For example, surface tension can play a role in multiphase flow however evaluating the forces require some knowledge of the geometry of the interface. In the case of the tsunamigenic landslide, the Lagrangian framework eases the inclusion of an energy loss function at the landslide–water interface or in the spray zone.

The Lagrangian framework also eases the tracking of material history which can have important rheologic implications such as for fluids with memory or for tracking work hardening of strain softening in plastic deformation. This tracking of material history facilitates the calculation of processes such as the evolution of fabrics in the rock through tracking of finite deformation or the tracking of chemical constituents in mantle convection.

With the inclusion of heat flux boundary conditions, this viscous SPH model is well positioned to address some of the complexities of deformation of coupled thermo-mechanical flows. For example, the mechanics of the solidification of a creeping lava flow is effected by the solidified surface rolling beneath the advancing front. This cooled material incorporated into the flow requires a tracking of the material history as it could effect the deformation field. For faster flows, the solidified material could become entrained into the flow and accelerate the cooling, a process difficult to model with grid-based methods.

BIBLIOGRAPHY

[1] R. C. Batra and G. M. Zhang. Analysis of adiabatic shear bands in elasto-thermo-viscoplastic materials by modified smoothed-particle hydrodynamics (MSPH) method. *Journal of Computational Physics*, 201:172–190, 2004.

[2] Ted Belytschko, Yury Krongauz, John Dolbow, and C. Gerlach. On the completeness of meshfree particle methods. *International Journal for Numerical Methods in Engineering*, 43(5):785–819, Nov 1998.

[3] Ted Belytschko, Y.Y. Lu, and L. Gu. Element-free Galerkin methods. *International Journal for Numerical Methods in Engineering*, 37(2):229–256, 1994.

[4] S. Betelu, J. Diez, L. Thomas, R. Gratton, and B. Marino. A boundary element method for viscous gravity currents. *International Journal for Numerical Methods in Fluids*, 25(1):1–19, 1997.

[5] Javier Bonet and Sivakumar Kulasegaram. Correction and stabilization of smooth particle hydrodynamics methods with applications in metal forming simulations. *International Journal for Numerical Methods in Engineering*, 47(6):1189–1214, 2000.

[6] Javier Bonet and Sivakumar Kulasegram. A simplified approach to enhance the performance of smooth particle hydrodynamics methods. *Applied Mathematics and Computation*, 126(2-3):133–155, Mar 2002.

[7] Javier Bonet and T.-S.L. Lok. Variational and momentum preservation aspects of smooth particle hydrodynamic formulations. *Computational Methods in Applied Mechanical Engineering*, 180(1-2):97–115, Nov 1999.

[8] Alexander N. Brooks and Thomas J. R. Hughes. Streamline upwind/Petrov-Galerkin formulations for convection dominated flows with particular emphasis on the incompressible Navier-Stokes equations. *Computer Methods in Applied Mechanics and Engineering*, 32:199–259, 1982. Also published in: *Computer Methods in Applied Mechanics and Engineering*; Special edition on the 20th Anniversary; p.199 - 259; 1990.

[9] L. Brookshaw. A method of calculating radiative heat diffusion in particle simulations. *Astronomical Society of Australia, Proceedings*, 6(2):207–210, 1985.

[10] W. Roger Buck and Dimitrios Sokoutis. Analog model of gravitational collapse and surface extension during continental convergence. *Nature*, 369:737–740, 1994.

[11] Suanne J.H. Buiter, Andrey Yu Babeyko, Susan Ellis, Taras V. Gerya, Boris J.P. Kaus, Antje Kellner, Guido Schreurs, and Yasuhiro Yamada. The numerical sandbox: comparison of model results for a shortening and an extension experiment. In S.J.H. Buiter and G. Schreurs,

editors, *Analogue and Numerical Modelling of Crustal-Scale Processes.*, volume 253, pages 29–64. Geological Society of America, 2006.

[12] David R. Burbidge. *The Complex Evolution of Accretionary Wedges and Thrust Belts: Results from Numerical Experiments Using the Distinct Element Method*. PhD thesis, Australian National University, 2000.

[13] David R. Burbidge and Jean Braun. Numerical models of the evolution of accretionary wedges and fold-and-thrust belts using the distinct-elment method. *Geophysical Journal International*, 148:542–561, 2002.

[14] Phil M. Campbell. Some new algorithms for boundary value problems in smooth particle hydrodynamics. Technical report, Mission Research Corp., Albuquerque, NM., 1989.

[15] A.K. Chaniotis, D. Poulikakos, and P. Koumoutsakos. Remeshed smoothed particle hydrodynamics for the simulation of viscous and heat conduction flows. *Journal of Computational Physics*, 182(1):67–90, 2002.

[16] J. K. Chen, J. E. Beraun, and C. J. Jih. Completeness of corrective smoothed particle method for linear elastodynamics. *Computational Mechanics*, 24(4):273–285, 1999.

[17] J. K. Chen, J. E. Beraun, and C. J. Jih. A corrective smoothed particle method for transient elastoplastic dynamics. *Computational Mechanics*, 27(3):177–187, 2001.

[18] J.K. Chen, J.E. Beraun, and T.C. Carney. A corrective smoothed particle method for boundary value problems in heat conduction. *International Journal for Numerical Methods in Engineering*, 46(2):231–252, 1999.

[19] Alexandre Joel Chorin. A numerical method for solving incompressible viscous flow problems. *Journal of Computational Physics*, 2:12–26, 1967.

[20] Paul W. Cleary and Joseph J. Monaghan. Conduction modelling using smoothed particle hydrodynamics. *Journal of Computational Physics*, 148(1):227–264, 1999.

[21] Andrea Colagrossi and Maurizio Landrini. Numerical simulation of interface flows by smoothed particle hydrodynamics. *Journal of Computational Physics*, 191(2):448–475, 2003.

[22] F. Colin, R. Egli, and F.Y. Lin. Computing a null divergence velocity field using smoothed particle hydrodynamics. *Journal of Computational Physics*, 217(2):680–692, 2006.

[23] Sharen J. Cummins and Murray Rudman. An SPH projection method. *Journal of Computational Physics*, 152(2):584–607, 1999.

[24] P.A. Cundall and O.D. Strack. A discrete numerical model for granular assemblies. *Géotechnique*, 29(1):47–65, 1979.

[25] F.A. Dahlen. Noncohesive critical Coulomb wedges: An exact solution. *Journal of Geophysical Research*, 89:10,125–10,133, 1984.

[26] A. Dedner, F. Kemm, D. Kröner, T. Schnitzer, and M. Wesenberg. Hyperbolic divergence cleaning for the MHD equations. *Journal of Computational Physics*, 175:645–673, 2002.

[27] Leo F. Donovan. A numerical solution of unsteady flow in a two-dimensional square cavity. *American Institute of Aeronautics and Astronautics Journal*, 8(3):524–529, 1970.

[28] John K. Dukowicz. Computational efficiency of the hybrid penalty-pseudocompressibility method for incompressible flow. *Computers and Fluids*, 23(2):479–486, 1994.

[29] Jacques Duran. *Sands, Powders, and Grains: An Introduction to the Physics of Granular Materials*. Springer Verlag, 1999.

[30] Marco Ellero, Mar Serrano, and Pep Español. Incompressible smoothed particle hydrodynamics. *Journal of Computational Physics*, 2006. accepted.

[31] Steven H. Emerman and D.L. Turcotte. A fluid model for the shape of accretionary wedges. *Earth and Planetary Science Letters*, 63:379–384, 1983.

[32] Philip England and Gregory Houseman. Role of lithospheric strength heterogeneities in the tectonics of Tibet and neighboring regions. *Nature*, 315:297–310, May 1985.

[33] Philip England and Dan P. McKenzie. A thin viscous sheet model for continental deformation. *Geophysical Journal of the Royal Astronomical Society*, 70:295–321, 1982.

[34] Emma Finch, Stuart Hardy, and Rob Gawthorpe. Discrete element modelling of contractional fault-propagation folding above rigid basement fault blocks. *Journal of Structural Geology*, 25:515–528, 2003.

[35] Hermann M. Fritz, Willi H. Hager, and Hans-Erwin Minor. Lituya Bay case: Rockslide impact and wave run-up. *Science of Tsunami Hazards*, 19(1):3–22, 2001.

[36] Philippe Fullsack. An arbitrary Lagrangian-Eulerian formulation for creeping flows and its application in tectonic models. *Geophysical Journal International*, 120(1):1–23, 1995.

[37] M. Gallati, G. Braschi, and S. Falappi. SPH simulations of the waves produced by a falling mass into a reservoir. *Il Nuovo Cimento C*, 28(2):129–140, 2005.

[38] R.A. Gingold and J.J. Monaghan. Smoothed particle hydrodynamics: Theory and application to non-spherical stars. *Monthly Notices Of The Royal Astronomical Society*, 181(2):375–389, 1977.

[39] H. Gotch, M. Hayashi, and T. Sakai. Lagrangian multiphase flow model for debris-flow-induced tsunami. In J.M. Smith, editor, *Coastal Engineering 2004: Proceedings of the 29th International Conference*, pages 1121–1133. ICCE, World Scientific, 2004.

[40] J.P Gray, J.J. Monaghan, and R.P. Swift. SPH elastic dynamics. *Computational Methods in Applied Mechanical Engineering*, 190:6641–6662, 2001.

[41] Philip Gresho. Incompressible fluid dynamics: Some fundamental formulation issues. *Annual Review of Fluid Mechanics*, 23:413–453, 1991.

[42] Philip Gresho and Robert L. Sani. On pressure boundary conditions for the incompressible Navier-Stokes equations. *International Journal for Numerical Methods in Fluids*, 7(10):1111–1145, 1987.

[43] Frank C. Günther and Wing Kam Liu. Implementation of boundary conditions for meshless methods. *Computer Methods in Applied Mechanics and Engineering*, 163:205–230, 1998.

[44] Ricardo Gutfraind and Stuart B. Savage. Marginal ice zone rheology: Comparison of results from continuum-plastic models and diescrete-particle simulations. *Journal of Geophysical Research*, 102(C6):12647–12661, June 1997.

[45] Ricardo Gutfraind and Stuart B. Savage. Smoothed particle hydrodynamics for the simulation of broken-ice fields: Mohr-Coulomb-type rheology and frictional boundary conditions. *Journal of Computational Physics*, 134:203–215, 1997.

[46] Ricardo Gutfraind and Stuart B. Savage. Flow of fractured ice through wedge-shaped channels: Smoothed particle hydrodynamics and discrete-element simulations. *Mechanics of Materials*, 29:1–17, 1998.

[47] J.V. Hall and J.W. Watts. Laboratory investigation of the vertical rise of solitary waves on impermeable slopes. Technical Report 33, Beach Erosion Board, US Army Corps of Engineer, 1953.

[48] Francis H. Harlow and J. Eddie Welch. Numerical calculation of time-dependent viscous incompressible flow of fluid with free surface. *Physics of Fluids*, 8(12):2182–2189, 1965.

[49] C. Hérault and Y. Maréchal. Boundary and interface conditions in meshless methods. *IEEE Transactions on Magnetics*, 35:1450–1453, 1999.

[50] B.E. Hobbs, H.-B. Mühlhaus, and A. Ord. Instability, softening and localization of deformation. In R.J. Knipe and E.H. Rutter, editors, *Deformation Mechanisms, Rheology and Tectonics*, number 54 in Special Publication, pages 143–165. Geological Society of America, 1990.

[51] Thomas J.R. Hughes, Wing Kam Liu, and Alec Brooks. Finite element analysis of incompressible viscous flows by the penalty function formulation. *Journal of Computational Physics*, 30:1–60, 1979.

[52] B. Hunt. Water waves generated by distant landslides. *Journal of Hydraulic Research*, 26:307–322, 1988.

[53] Herbert E. Huppert. The propagation of two-dimensional and axisymetric viscous gravity currents over a rigid horizontal surface. *Journal of Fluid Mechanics*, 121:43–58, 1982.

[54] Herbert E. Huppert. The intrusion of fluid mechanics into geology. *Journal of Fluid Mechanics*, 173:557–594, 1986.

[55] F. Jiang, M.S.A. Oliveira, and A.C.M. Sousa. SPH simulation of low Reynolds number planar shear flow and heat convection. *Materialwissenschaft und Werkstofftechnik*, 36(10):613–619, 2005.

[56] Gordon R. Johnson, Robert A. Stryk, and Stephen R. Beissel. SPH for high velocity impact computations. *Computational Methods in Applied Mechanical Engineering*, 139:347–373, 1996.

[57] Martin Jubelgas, Volker Springel, and Klaus Dolag. Thermal conduction in cosmological SPH simulations. *Monthly Notices of the Royal Astronomical Society*, 351(2):423, 2004.

[58] Y. Krongauz and T. Belytschko. Consistent pseudo-derivatives in meshless methods. *Computer Methods in Applied Mechanics and Engineering*, 146(3):371–386, July 1997.

[59] T. William Lambe and Robert V. Whitman. *Soil mechanics*. Wiley, 1969.

[60] H. P. Langtangen, K.-A. Mardal, and R. Winther. Numerical methods for incompressible viscous flow. *Advances in Water Resources*, 25:1125–1146, 2002.

[61] L. Law and A. Brebner. On water waves generated by landslides. In *Third Australasian Conference on Hydraulics and Fluid Mechanics*, pages 155–159, Sydney, 1968. Paper 2561.

[62] Shaofan Li, Wei Hao, and Wing Kam Liu. Mesh-free simulations of shear banding in large deformation. *International Journal of Solids and Structures*, 37(50):7185–7206, 2000.

[63] Shaofan Li and Wing Kam Liu. Meshfree and particle methods and their applications. *Applied Mechanics Review*, 55:1–34, 2002.

[64] Shaofan Li, Wing Kam Liu, Ares J. Rosakis, Ted Belytschko, and Wei Hao. Mesh-free Galerkin simulations of dynamic shear band propagation and failure mode transition. *International Journal of Solids and Structures*, 39:1213–1240, 2002.

[65] Gui-Rong Liu. *Mesh Free Methods: Moving beyond the finite element method*. CRC Press, LLC, Boca Raton, Florida, 2003.

[66] Gui-Rong Liu and M.B. Liu. *Smoothed Particle Hydrodynamics: A meshfree particle method*. World Scientific Publishing Co. Pte. Ltd., Singapore, 2003.

[67] M.B. Liu and Gui-Rong Liu. Restoring particle consistency in smoothed particle hydrodynamics. *Applied Numerical Mathematics*, 56(1):19–36, 2006.

[68] Wing Kam Liu and Sukky Jun. Multiple-scale reproducing kernel particle moethod for large deformation problems. *International Journal for Numerical Methods in Engineering*, 41(7):1339–1362, Apr 1998.

[69] Wing Kam Liu, Sukky Jun, and Fei Zhang. Reproducing kernel particle methods. *International Journal for Numerical Methods in Fluids*, 20(8-9):1081–1106, 1995.

[70] Louis A. Lliboutry. *Very Slow Flow of Solids*. Kluwer Academic Publishing Group, 1987.

[71] L.B. Lucy. A numerical approach to testing the fission hypothesis. *Astronomical Journal*, 82(12):1013–1024, 1977.

[72] Charles L. Mader. Modeling the 1958 Lituya Bay mega-tsunami. *Science of Tsunami Hazards*, 17(1):57–68, 1999.

[73] Charles L. Mader. *Numerical Modeling of Water Waves*. CRC Press, New York, 2 edition, 2004.

[74] Charles L. Mader and Michael L. Gittings. Modeling the 1958 Lituya Bay mega-tsunami, II. *Science of Tsunami Hazards*, 20(5):241–250, 2002.

[75] Lawrence E. Malvern. *Introduction to the Mechanics of a Continuous Medium*. Prentice-Hall, Inc., Englewood Cliffs, New Jersey, 1969.

[76] G. Thomas Mase and George E. Mase. *Continuum Mechanics for Engineers*. CRC Press LLC, Boca Raton, Florida, 1999.

[77] Scott McDougall and Oldrich Hungr. A model for the analysis of rapid landslide motion across three-dimensional terrain. *Canadian Geotechnical Journal*, 41(6):1084–1097, 2004.

[78] P.R. McHugh and J.D. Ramshaw. Damped artificial compressibility iteration scheme for implicit calculations of unsteady incompressible flow. *International Journal For Numerical Methods In Fluids*, 21(2):141–153, 1995.

[79] Dan McKenzie. Finite deformation during fluid flow. *Geophysical Journal of the Royal Astronomical Society*, 58(3):689–715, 1979.

[80] Olivier Merle. *Emplacement Mechanisms of Nappes and Thrust Sheets*, volume 9 of *Petrology and Structural Geology*. Kluwer Academic Publishers, 1998.

[81] Don J. Miller. Giant waves in Lituya Bay, Alaska. Professional Paper 354-C, United States Geological Survey, Washington D.C, 1960.

[82] J. J. Monaghan. Simulating free surface flows with SPH. *Journal of Computational Physics*, 110(2):399–406, 1994.

[83] J. J. Monaghan and A. Kos. Solitary waves on a Cretan beach. *Journal of Waterway, Port, Coastal, and Ocean Engineering*, 125(3):145–155, 1999.

[84] J.J. Monaghan. Smoothed particle hydrodynamics. *Annual Review of Astronomy and Astrophysics*, 30:543–74, 1992.

[85] J.J. Monaghan, A. Kos, and N. Issa. Fluid motion generated by impact. *Journal of Waterway, Port, Coastal, and Ocean Engineering*, 129(6):250–259, 2003.

[86] L. Moresi. Pers. comm.

[87] L. Moresi, F. Dufour, and H.-B. Mühlhaus. A Lagrangian integration point finite element method for large deformation modeling of viscoelastic geomaterials. *Journal of Computational Physics*, 184(2):476–497, 2003.

[88] L. Moresi, H.-B. Muhlhaus, and F. Dufour. Particle-in-cell solutions for creeping viscous flows with internal interfaces. In H.-B. Muhlhaus, A. Dyskin, and E. Pasternak, editors, *Proceedings of the 5th International Workshop on Bifurcation and Localization in Soils and Rocks*, pages 345–354. Balkema., 2001.

[89] Joseph P. Morris, Patric J. Fox, and Yi Zhu. Modeling low Reynolds number incompressible flows using SPH. *Journal of Computational Physics*, 136(1):214–226, 1997.

[90] C.-D. Munz, P. Omnes, R. Schneider, E. Sonnendrücker, and U. Voß. Divergence correction techniques for Maxwell solvers based on a hyperbolic model. *Journal of Computational Physics*, 161:484–511, 2000.

[91] Mark Naylor, Hugh Sinclair, Sean Willett, and Patience Cowie. A discrete element model for orogenesis and accretionary wedge growth. *Journal of Geophysical Research*, 110:B12403, 2005.

[92] A. Needleman. Material rate dependence and mesh sensitivity in localization problems. *Computer Methods In Applied Mechanics and Engineering*, 67:60–85, 1988.

[93] G. Oger, M. Doring, B. Alessandrini, and P. Ferrant. Two-dimensional SPH simulations of wedge water entries. *Journal of Computational Physics*, 213(2):803–822, 2005.

[94] L. Oger and S.B. Savage. Smoothed particle hydrodynamics for cohesive grains. *Computational Methods in Applied Mechanical Engineering*, 180(1-2):169–183, Nov 1999.

[95] L. Oger, S.B. Savage, D. Corriveau, and M. Sayed. Yield and deformation of an assembly of disks subjected to a deviatoric stress loading. *Mechanics of Materials*, 27(4):189–210, 1998.

[96] Steven A. Orszag, Moshe Israeli, and Michel O. Deville. Boundary conditions for incompressible flows. *Journal of Scientific Computing*, 1:75–111, 1986.

[97] Andrea Panizzo. *Physical and numerical modelling of subaerial landslide generated waves*. PhD thesis, Università degli studi di L'Aquila, L'Aquila, 2004.

[98] George Pararas-Carayannis. Analysis of mechanism of tsunami generation in Lituya Bay. *Science of Tsunami Hazards*, 17(3):193–206, 1999.

[99] J. Pozorski and A. Wawrenczuk. SPH computations of incompressible viscous flows. *Journal of Theoretical and Applied Mechanics*, 40:917–937, 2002.

[100] William E. Pracht. A numerical method for calculating transient creep flows. *Journal of Computational Physics*, 7(1):46–60, 1971.

[101] Daniel J. Price. *SPLASH– v1.8.0.*

[102] Daniel J. Price and J.J. Monaghan. Smoothed particle magnetohydrodynamics III. Multidimensional tests and the $\nabla \cdot B = 0$ constraint. *Monthly Notices of the Royal Astronomical Society*, 362:384–406, 2005.

[103] Daniel James Price. *Magnetic Fields in Astrophysics*. PhD thesis, Churchill College, University of Cambridge, Cambridge, August 2004.

[104] Andreas Prohl. *Projection and Quasi-Compressibility Methods for Solving the Incompressible Navier-Stokes Equations*. B.G. Teubner, 1997.

[105] M. Quecedo, M. Pastor, and M. I. Herreros. Numerical modelling of impulse wave generated by fast landslides. *International Journal for Numerical Methods in Engineering*, 59(12):1633–1656, 2004.

[106] Nathan Quinlan, Mihai Basa, and Martin Lastiwka. An analysis of accuracy in one-dimensional smoothed particle hydrodynamics. In *17th AIAA Computational Fluid Dynamics Conference*, page 4622, Toronto, Canada, June 2005. American Institute of Aeronautics and Astronautics.

[107] Nathan J. Quinlan, Mihai Basa, and Martin Lastiwka. Truncation error in mesh-free particle methods. *International Journal for Numerical Methods in Engineering*, 66(13):2064–2085, Jan 2006.

[108] T. Rabczuk and P.M.A. Areias. A new approach for modelling slip lines in geological materials with cohesive models. *International Journal for Numerical and Analytical Methods in Geomechanics*, 30(11):1159–1172, 2006.

[109] J.D. Ramshaw and G.L. Mesina. A hybrid penalty-pseudocompressibility method for transient incompressible fluid flow. *Computers and Fluids*, 20(2):165–175, 1991.

[110] J.D. Ramshaw and V.A. Mousseau. Accelerated artificial compressibility method for steady-state incompessible flow calculations. *Computers and Fluids*, 18:361–367, 1990.

[111] J.D. Ramshaw and V.A. Mousseau. Damped artificial compressibility method for steady-state low-speed flow calculations. *Computers and Fluids*, 20(2):177–186, 1991.

[112] P.W. Randles and L.D. Libersky. Smoothed particle hydrodynamics: Some recent improvements and applications. *Computational Methods in Applied Mechanical Engineering*, 139(1-4):375–408, Dec 1996.

[113] M. X. Rodriguez-Paz and Javier Bonet. A corrected smooth particle hydrodynamics method for the simulation of debris flows. *Numerical Methods for Partial Differential Equations*, 20(1):140–163, 2003.

[114] Yousef Saad. SPARSKIT: A basic tool kit for sparse matrix computations. Technical Report RIACS-90-20, Research Institute for Advanced Computer Science, NASA Ames Research Center, Moffet Field, CA, 1990.

[115] Yuzuru Sakai, Zong Yi Yang, and Young Guan Jung. Incompressible viscous flow analysis by SPH. *Nihon Kikaigakkai Rombunshu B-Hen (Transactions of the Japan Society of Mechanical Engineers)*, 70:47–54, 2004.

[116] Guido Schreurs, Susanne J.H. Buiter, David Boutelier, Giacomo Corti, Elisabetta Costa, Alexander R. Cruden, Jean-Marc Daniel, Silvan Hoth, Hemin A. Koyi, Nina Kukowski, Jo Lohrmann, Antonio Ravaglia, Roy W. Schlische, Martha Oliver Withjack, Yasuhiro Yamada, Cristian Cavozzi, Chiara DelVentisette, Jennifer A. Elder Brady, Arne Hoffmann-Rothe, Jean-Marie Mengus, Domenico Montanari, and Faramarz Nilforoushan. Analogue benchmarks of shortening and extension experiments. In S.J.H. Buiter and G. Schreurs, editors, *Analogue and Numerical Modelling of Crustal-Scale Processes.*, volume 253, pages 1–27. Geological Society of America, 2006.

[117] Will Schroeder, Ken Martin, and Bill Lorensen. *The Visualization Toolkit: An Object Oriented Approach to 3D Graphics.* Kitware, Inc., 2003.

[118] Hans F. Schwaiger, Sean D. Willett, and Christopher Fuller. A mesh-free Lagrangian fluid model for creeping flow of history-dependent material with applications to extensional tectonics. In *Eos. Trans. AGU*, volume 84, pages T31D–0873, 2005. Fall Meet. Suppl.

[119] M. Seyferth and A. Henk. A numerical sandbox: High-resolution distinct element models of halfgraben formation. *International Journal of Earth Sciences*, 95(2):189–203, 2005.

[120] Songdong Shao and Edmond Y. M. Lo. Incompressible SPH method for simulating Newtonian and non-Newtonian flows with a free surface. *Advances in Water Resources*, 26(7):787–800, 2003.

[121] Hung Tao Shen, Jushan Su, and Lianwu Liu. SPH simulation of river ice dynamics. *Journal of Computational Physics*, 165(2):752–770, 2000.

[122] Jie Shen. On pressure stabilization method and projection methods for unsteady Navier-Stokes equations. In R. Vichnevestsky, D. Knight, and G. Richter, editors, *Advances in Computer Methods for Partial Differential Equations-VII*, pages 658–662. IMACS, 1992.

[123] Jie Shen. On a new pseudo-compressibility method for the incompressible Navier-Stokes equations. *Applied Numerical Mathematics*, 21:71–90, 1996.

[124] Jie Shen. Pseudo-compressibility methods for the unsteady incompressible Navier-Stokes equations. In *Proceedings of the 1994 Beijing Symposium on Nonlinear Evolution Equations and Infinite Dynamical Systems*, 1997.

[125] R.L. Slingerland and B. Voight. Evaluating hazard of landslide-induced water waves. *Journal of Waterway, Port, Coastal, and Ocean Engineering*, 108:504–512, 1982.

[126] Luther M. Strayer and John Suppe. Out-of-plane motion of a thrust sheet along-strike propagation of a thrust ramp: a distinct-element approach. *Journal of Structural Geology*, 24(4):637–650, 2002.

[127] Kurt Stüwe. *Geodynamics of the Lithosphere.* Springer Verlag, Berlin, 2002.

[128] E Suleimani and P Vollmoeller. Numerical simulation of impulse waves generated by sliding masses. In *Eos Trans. AGU*, volume 87, 2006. Fall Meet. Suppl., Abstract OS43C-0685.

[129] D. Sulsky and H. Schreyer. Antisymmetric form of the material point method with applications to upsetting and taylor impact problems. *Computer Methods in Applied Mechanics and Engineering*, 139:409–429, 1996.

[130] Hidenori Takeda, Shoken M. Miyama, and Minoru Sekiya. Numerical simulation of viscous flow by smoothed particle hydrodynamics. *Progress of Theoretical Physics*, 92(5):939–960, Nov 1994.

[131] Roger Témam. *Navier-Stokes Equations: Theory and Numerical Analysis*, volume 2 of *Studies In Mathematics and its Aplications*. North-Holland, 1979.

[132] Gábor Tóth. The $\nabla \cdot B = 0$ constraint in shock-capturing magnetohydrodynamics codes. *Journal of Computational Physics*, 161(2):605–652, 2000.

[133] D. L. Turcotte and G. Schubert. *Geodynamics: Applications of Continuum Physics to Geological Problems*. Wiley, New York, 1982.

[134] I. Vardoulakis and J. Sulem. *Bifurcation Analysis in Geomechanics*. Blackie Academic and Professional, 1995.

[135] T. Vietor. Numerical simulation of collisional orogeny using the distinct element technique. In H. Konietzky, editor, *Numerical Modeling in Micromechanics via Particle Methods*, pages 295–301, Rotterdam, 2003. A.A. Balkema.

[136] Gregory J. Wagner and Wing Kam Liu. Application of essential boundary conditions in mesh-free methods: A corrected collocation method. *International Journal for Numerical Methods in Engineering*, 47:1367–1379, 2000.

[137] S.J. Watkins, A.S. Bhattal, N. Francis, J.A. Turner, and A.P. Whitworth. A new prescription for viscosity in smoothed particle hydrodynamics. *Astronomy And Astrophysics Supplement Series*, 119:177–187, 1996.

[138] E. Weinan and Jian-Guo Liu. Projection method I: Convergence and numerical boundary layers. *SIAM Journal on Numerical Analysis*, 32(4):1017–1057, 1995.

[139] P. Wessel and W. H. F. Smith. 1995 new version of the generic mapping tools released. In *EOS Trans. AGU*, volume 76, page 329, 1995.

[140] Sean D. Willett. Dynamic and kinematic growth and change of a Coulomb wedge. In *Thrust Tectonics*, pages 19–31. Chapman and Hall, London, 1992.

[141] Sean D. Willett. Rheological dependence of extension in wedge models of convergent orogens. *Tectonophysics*, 305(4):419–435, 1999.

[142] Sean D. Willett, Chris Beaumont, and Philippe Fullsack. Mechanical model for the tectonics of doubly vergent compressional orogens. *Geology*, 21(4):371–374, 1993.

[143] Cheng-Kong C. Wu and Michael E. Plesha. Essential boundary condition enforcement in meshless methods: Boundary flux collocation method. *International Journal for Numerical Methods in Engineering*, 53(3):499–514, 2000.

[144] Yasuhiro Yamada, Kei Baba, and Toshifumi Matsuoka. Analogue and numerical modelling of accretionary prisms with a décollement in sediment. In S.J.H. Buiter and G. Schreurs, editors, *Analogue and Numerical Modelling of Crustal-Scale Processes.*, volume 253, pages 169–183. Geological Society of America, 2006.

[145] N.N. Yanenko, B.G. Kuznetsov, and Sh. Smagulov. *Numerical Methods In Fluid Dynamics*, chapter On the approximation of the Navier-Stokes equations for an incompressible fluid by evolution-type equations, pages 291–314. Mir Publishers, 1984.

[146] Erich Zauderer. *Partial Differential Equations of Applied Mathematics*. John Wiley & Sons, 1983.

[147] G.M. Zhang and R.C. Batra. Modified smoothed particle hydrodynamics method and its application to transient problems. *Computational Mechanics*, 34(2):137–146, Jul 2004.

VITA

Hans Schwaiger was born in 1972 and grew up in Anchorage, Alaska. He spent his undergraduate years in Ithaca, NY at Cornell University. By the time he settled on physics as a major (AB, Jan. 1996), he discovered the geology department where he began spending most of his time, ultimately getting a degree from that department as well (M.Eng. in geophysics, Aug. 1996). Hesitant about jumping into a PhD program without first exploring the world, he spent the next five years working as either a research assistant, field assistant in Antarctica, or a consulting geophysicist (Alaska and Washington). Finally, he stepped back into academia at the University of Washington where he earned a Masters in Applied Mathematics (June, 2006) and a PhD in Geophysics (June, 2007).